

Simulating the signature of starspots in stellar oscillations

Dissertation

zur Erlangung des mathematisch-naturwissenschaftlichen Doktorgrades

“Doctor rerum naturalium”

der Georg-August-Universität Göttingen

im Promotionsprogramm PROPHYS

der Georg-August University School of Science (GAUSS)

vorgelegt von

Emanuele Papini

aus Firenze, Italien

Göttingen, 2015

Betreuungsausschuss

Prof. Dr. Laurent Gizon

Institut für Astrophysik, Georg-August-Universität, Göttingen, Deutschland
Max-Planck-Institut für Sonnensystemforschung, Göttingen, Deutschland

Prof. Dr. Ansgar Reiners

Institut für Astrophysik, Georg-August-Universität, Göttingen, Deutschland

Dr. Aaron C. Birch

Max-Planck-Institut für Sonnensystemforschung, Göttingen, Deutschland

Mitglieder der Prüfungskommission

Referent: Prof. Dr. Laurent Gizon

Institut für Astrophysik, Georg-August-Universität, Göttingen, Deutschland
Max-Planck-Institut für Sonnensystemforschung, Göttingen, Deutschland

Korreferent: Prof. Dr. Ansgar Reiners

Institut für Astrophysik, Georg-August-Universität, Göttingen, Deutschland

Weitere Mitglieder der Prüfungskommission:

Prof. Dr. Jörg Büchner

Max-Planck-Institut für Sonnensystemforschung, Göttingen, Deutschland

Prof. Dr. Thorsten Hohage

Institut für Numerische und Angewandte Mathematik,
Georg-August-Universität, Göttingen, Deutschland

PD Dr. Olga Shishkina

Max-Planck-Institut für Dynamik und Selbstorganisation, Göttingen, Deutschland

Prof. Dr. Andreas Tilgner

Institut für Geophysik, Universität Göttingen, Deutschland

Tag der mündlichen Prüfung: 28. Juli 2015

Contents

Summary	5
Zusammenfassung	7
1 Introduction	9
1.1 Acoustic oscillations and magnetic activity	11
1.2 Modeling approaches	12
1.2.1 Time-domain simulations of linear oscillations	13
1.3 Results contained in this work	14
2 Propagating linear waves in convectively unstable stellar models: A perturbative approach	17
2.1 Background stabilization in time-domain simulations	17
2.2 Proposed solution: A perturbative approach	19
2.2.1 Constructing convectively stable background models	19
2.2.2 First-order correction to the wave field	20
2.3 Testing the method in 1D for the Sun	22
2.3.1 Acoustic modes	23
2.3.2 Rotational sensitivity kernels	25
3 Simulating acoustic waves in spotted stars	31
3.1 Introduction	32
3.1.1 Motivation: Low degree stellar oscillations	32
3.1.2 Our approach: Time-domain numerical simulations of waves and starspot	32
3.2 Numerical method	33
3.2.1 Time-domain pseudo-spectral simulations in spherical geometry	33
3.2.2 Extending the simulation to the center of the star	34
3.2.3 Validation: Comparison with ADIPLS normal modes	35
3.3 Frequency shifts: Nonlinear dependence on perturbation amplitude	36
3.3.1 Spot model: Perturbation in sound speed	36
3.3.2 Linear theory	38
3.3.3 Numerical simulations	40
3.4 Perturbations to the eigenfunctions	45
3.5 Synthetic power spectra for a polar spot	46
3.5.1 Synthetic light curves	46

3.5.2	Example power spectrum for $\ell = 2$	50
4	On the asteroseismic signature of a large active region	51
4.1	Introduction	52
4.2	Signature of an active region in the acoustic power: linear theory	52
4.2.1	Linear problem in the corotating frame	52
4.2.2	Power spectrum: asymmetric profiles and blended peaks in $n\ell$ -multiplets	59
4.3	Nonlinear frequency shifts and amplitudes in synthetic power spectra from numerical simulations	73
4.3.1	Synthetic power spectrum with rotation	75
5	Conclusions	81
5.1	Conclusions of chapter 2	81
5.2	Conclusions of chapter 3	83
5.3	Conclusions of chapter 4	83
5.4	Outlook	84
	Bibliography	85
	Publications	93
	Acknowledgements	95
	Curriculum vitae	97

Summary

It has been known for a few decades that acoustic oscillations are affected by stellar activity. In the case of the Sun global acoustic modes show a variation with the 11-year cycle and a similar phenomenon has been observed in other stars with asteroseismology. In this work I investigate the effects of large starspots on the global low-degree modes of stellar oscillations. I use the GLASS code to simulate the propagation of small amplitude acoustic waves in 3D stellar interiors.

Firstly, I consider the problem of convective stabilization, common to every linear oscillation code in the time domain. A general method to build a convectively stable background starting from a given stellar model is presented. Important properties of the original model, such as hydrostatic equilibrium, are preserved by the method. A perturbative approach to approximately recover the acoustic wavefield in the original unstable stellar model is proposed. Tests show that the corrected frequencies are within $1 \mu\text{Hz}$ of the exact values for low-degree modes near 3 mHz.

Secondly, using the GLASS code, I study the effects of a localized sound speed perturbation placed at the north pole on radial, dipole, and quadrupole modes of oscillation. The study shows that the axisymmetric modes are the most strongly affected and their frequencies cannot be modeled by linear theory for large starspots. Mode eigenfunctions depart from their shape of pure spherical harmonics and get mixed with spherical harmonics of different angular degrees. This may affect the correct identification of the modes in the power spectrum.

Thirdly, we consider the observational signatures of a large starspot on modes of angular degree ℓ . For an active region rotating with the star (and not situated at a pole), the perturbation is not steady in any inertial frame. The combined effects of rotation and the starspot cause each mode to appear as $(2\ell + 1)^2$ peaks in the observed power spectrum. The envelope of the power spectrum of a multiplet is thus complex and depends on the latitude of the active region and the inclination angle of the star. Examples are computed using both perturbation theory and the GLASS code. This work ought to be useful in interpreting oscillation power spectra of spotted pulsators.

Zusammenfassung

Wie seit schon einigen Jahrzehnten bekannt ist, werden akustische Oszillationen durch stellare Aktivität beeinflusst. Die globalen akustischen Moden in der Sonne weisen eine Variation mit dem 11-jährigen Sonnenzyklus auf. Ein ähnliches Phänomen konnte auch in anderen Sternen mit Hilfe von Asteroseismologie nachgewiesen werden. In dieser Arbeit erforsche ich den Einfluss von großen Sternflecken auf globale Oszillationen mit niedrigem Grad ℓ . Als wichtigstes Werkzeug benutze ich hierfür den GLASS Kode, der die Ausbreitung von linearen akustischen Wellen im Sterninneren in 3D simuliert.

Zunächst habe ich das Problem der konvektiven Stabilisierung betrachtet, welches bei jedem linearen Oszillationskode im Zeitbereich auftritt. Ich präsentiere eine allgemeine Methode um konvektiv stabile Hintergrundmodelle für ein vorgegebenes Sternmodell zu erzeugen. Dabei werden wichtige Eigenschaften des ursprünglichen Modells beibehalten, beispielsweise das hydrostatische Gleichgewicht. Ich schlage einen störungstheoretischen Ansatz vor, um das akustische Wellenfeld in dem ursprünglichen instabilen Sternmodell näherungsweise zu erlangen. Tests zeigen, dass für Moden mit niedrigem Grad ℓ und einer Frequenz um 3 mHz die korrigierten Frequenzen mit einer Genauigkeit von $1 \mu\text{ Hz}$ mit den exakten Werten übereinstimmen.

Zweitens habe ich mit Hilfe des GLASS Kodes den Einfluss einer am Nordpol des Sterns lokalisierten Störung der Schallgeschwindigkeit auf radiale, dipolare und quadrupolare Oszillationsmoden untersucht. Diese Studie zeigt auf, dass die axialsymmetrischen Moden dadurch am stärksten beeinflusst werden und im Falle von großen Sternflecken können ihre Frequenzen nicht mit der linearen Theorie berechnet werden. Die Form der Eigenfunktionen der Moden weicht von reinen Kugelflächenfunktionen ab und werden mit Kugelflächenfunktionen mit unterschiedlichem Grad ℓ vermischt. Dies könnte die korrekte Identifikation der Moden in der spektralen Leistungsdichte beeinflussen.

Drittens habe ich den beobachtbaren Einfluss eines großen Sternflecks auf Moden mit Grad ℓ betrachtet. Im Falle einer aktiven Region, die mit dem Stern rotiert (und sich nicht am Pol befindet), ist die Störung nicht stabil, wenn sie in einem Inertialsystem betrachtet wird. Der kombinierte Einfluss von Rotation und Sternfleck veranlasst jede Mode, in der beobachteten spektralen Leistungsdichte als $(2\ell + 1)^2$ Peaks aufzutreten. Die Einhüllende der spektralen Leistungsdichte eines Multipletts ist also komplex und hängt von dem Breitengrad ab, wo sich die aktive Region befindet, und vom Inklinationwinkel des Sterns.

Ich berechne die spektrale Leistungsdichte für einige Beispiele sowohl mit Störungstheorie als auch mit Hilfe von GLASS. Diese Arbeit soll dazu beitragen, die spektrale Leistungsdichte von oszillierenden Sternen, die Sternflecken aufweisen, zu interpretieren.

1 Introduction

Since observations made in the middle of the twentieth century (Leighton et al. 1962) it has been known that the Sun possesses a rich spectrum of acoustic oscillations, measured at the surface through observations of brightness and velocity fluctuations. The observed spectrum is the surface manifestation of acoustic waves excited by turbulent convection in the layers near the surface, propagating in the solar interior and finally reemerging at the surface, where they are detected. While traveling inside the Sun, acoustic waves sense the internal physical properties and configurations of flows and magnetic fields, therefore they carry information about the internal solar structure and dynamics.

Helioseismology (Christensen-Dalsgaard 2002) is a collection of tools developed to unravel that information. It allowed accurate measurements of internal differential rotation (see, *e.g.*, Thompson et al. 1996; Schou et al. 1998), sound speed and density stratification (Gough et al. 1996) and was fundamental in solving the solar neutrino problem, by assessing the quality of the theoretical models of the internal structure of the Sun (Christensen-Dalsgaard et al. 1996). Helioseismic observations not only allow us to image the interior of the Sun directly: they also pose several constraints and serve as a test bench in the development of theoretical models for the solar dynamo, convection, stellar rotation, to name a few.

Asteroseismology (for a general introduction see, *e.g.*, Aerts et al. 2010) extends the study of acoustic oscillations to other stars. Due to the impossibility of spatially resolving the stellar surface, only a few tens of modes (radial, dipole and quadrupole modes; in some cases also octupole modes have been detected, see Metcalfe et al. 2012) can be observed with asteroseismology, while for the Sun millions of modes have been measured so far. Figure 1.1 shows the power spectrum of a Sun-like star observed by *Kepler* (KIC 005184732), that represents a typical power spectrum observable with asteroseismology. After few pioneering detections of Sun-like pulsators¹ (for an overview of helio- and asteroseismology with an historical focus see, *e.g.*, Christensen-Dalsgaard 2004; Bedding 2014), first the *Convection, Rotation & planetary Transits* (CoRoT, Auvergne et al. 2009), and then the *Kepler* (Borucki et al. 2010) satellites led to a breakthrough in the field. For the first time, asteroseismic data with long-term continuous observations and of excellent quality provided by CoRoT and *Kepler* allowed detection of acoustic oscillations in $\sim 10\,000$ Sun-like stars. The exploitation of these data helps to constrain the internal physical properties of stars of different mass, age, and chemical composition throughout the H-R diagram, and (among other applications) it allows for testing theories and models for stellar structure, dynamics, and evolution.

¹With this term we indicate those stars for which the mechanism for excitation and damping of the acoustic wavefield is the same as for the Sun, namely the near-surface convection.

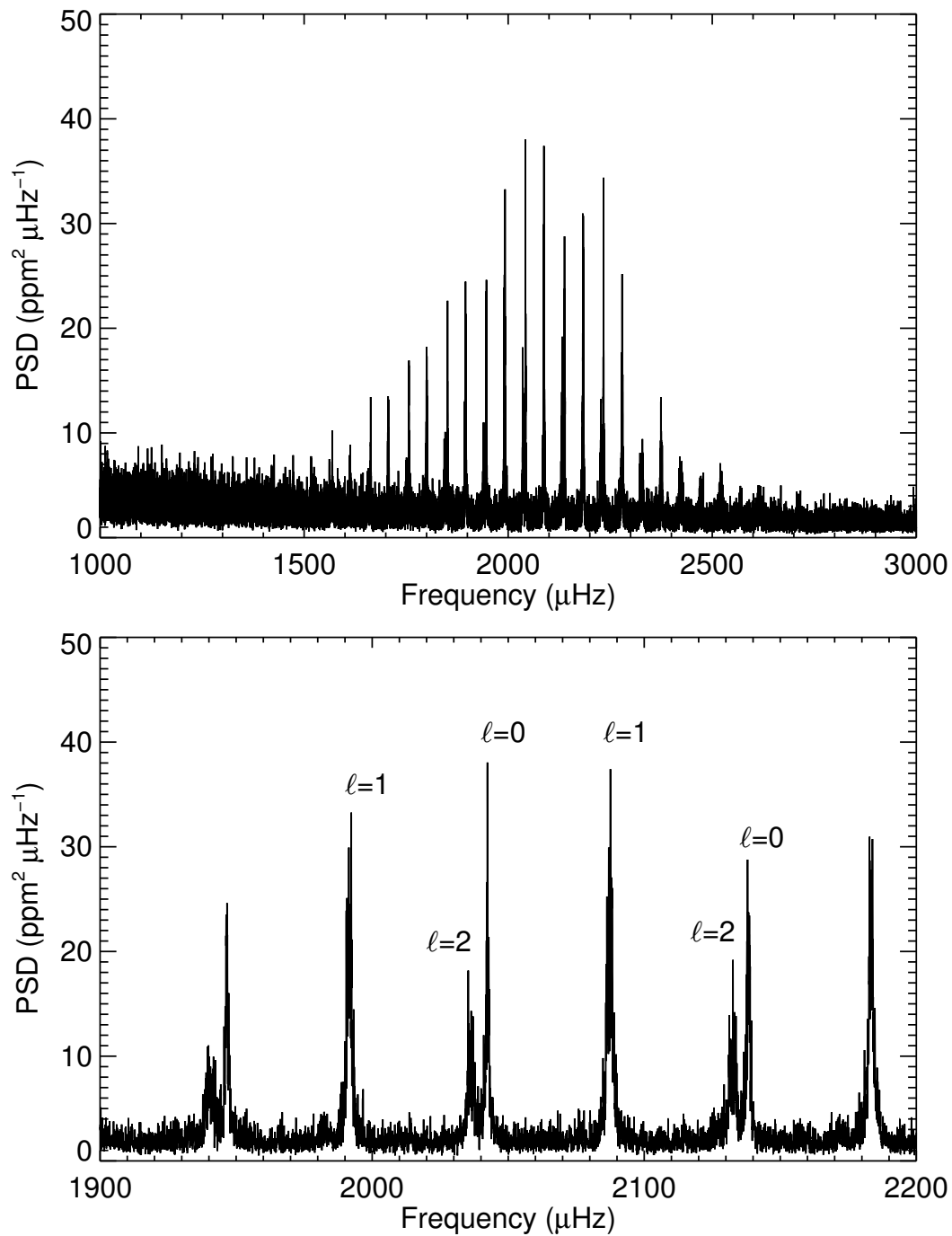


Figure 1.1: Power spectral density (PSD) of a Sun-like star (KIC 005184732), as observed by *Kepler*, showing the spectrum of the acoustic oscillations (upper panel). The lower panel gives an expanded view in the central part of the spectrum. Here some modes are labeled by their degree ℓ , and the characteristic repeating pattern is visible. The spectrum was smoothed by applying a Gaussian filter. The data were obtained from 90 days of observation (data courtesy of Martin Bo Nielsen).

A very successful application of asteroseismology includes the detection and characterization of exoplanets. Measuring exoplanet properties, such as radius, mass, position in the stellar system, and the location of the habitable zone, is made possible by knowing the parameters of the host star. With *Kepler* the number of detected exoplanets increased exponentially, and the future missions, *Transiting Exoplanet Survey Satellite* (TESS) from NASA (Ricker et al. 2014), and *PLANetary Transits and Oscillations of stars* (PLATO) from ESA (Rauer et al. 2014), promise to further expand the observations up to $\sim 1\,000\,000$ stars across the sky.

1.1 Acoustic oscillations and magnetic activity

The dynamics of magnetic fields in stars is a complex study which involves phenomena acting at different length scales and time scales, ranging from typical time scales of a few hours (in the case of convection), up to months (for active regions) and years (in the case of the solar dynamo) for magnetic structures. As a result the properties of seismic waves change with time because of the evolving magnetic structures. In particular, for the Sun, it has been observed that magnetic activity influences global acoustic modes (Libbrecht and Woodard 1990). These modes show a variation in their frequencies with the 11-year solar cycle, with a frequency shift of $0.4\ \mu\text{Hz}$ for a mode frequency of about $3\ \text{mHz}$ and a decrease in their amplitudes by $\sim 20\%$. Figure 1.2 shows the 11-year frequency variability in the acoustic modes of the Sun from the last three cycles (from Figure 1 of Broomhall et al. 2014). There is no doubt that these changes are related to the solar cycle, but their origin is unclear. The responsible physical mechanism probably takes place near the surface, owing to the fact that the frequency shifts are almost independent of the angular degree ℓ of the oscillations.

Chaplin et al. (2007b), based on a dataset of thirty years of observations, suggested that this variation is most likely associated with the weak and widely latitude-distributed component of the magnetic flux in the quiet Sun, rather than with strong and localized structures (like sunspots and active regions).

Magnetic activity is not a phenomenon confined to our Sun, as it has been known for a few decades now. Observation campaigns of chromospheric emission from the CaII H and K lines, started by Wilson (1968) and carried out for more than 20 years (Balinas et al. 1995), revealed stars with magnetic activity cycles of different periods and amplitudes. Moreover, Böhm-Vitense (2007) reported the existence of a relation between stellar rotation periods and activity cycle period, reflecting the action of a stellar dynamo operating in different regimes. Finally, seismic measurements from CoRoT revealed the existence of magnetic activity in a Sun-like star (HD 49933, García et al. 2010), thus allowing asteroseismology, for the first time, to directly measure magnetic activity. This proved that asteroseismology can probe stellar magnetic activity.

Asteroseismology provides a unique tool for probing the magnetic structure and dynamics of other stars, and to give fundamental insight into stellar dynamos.

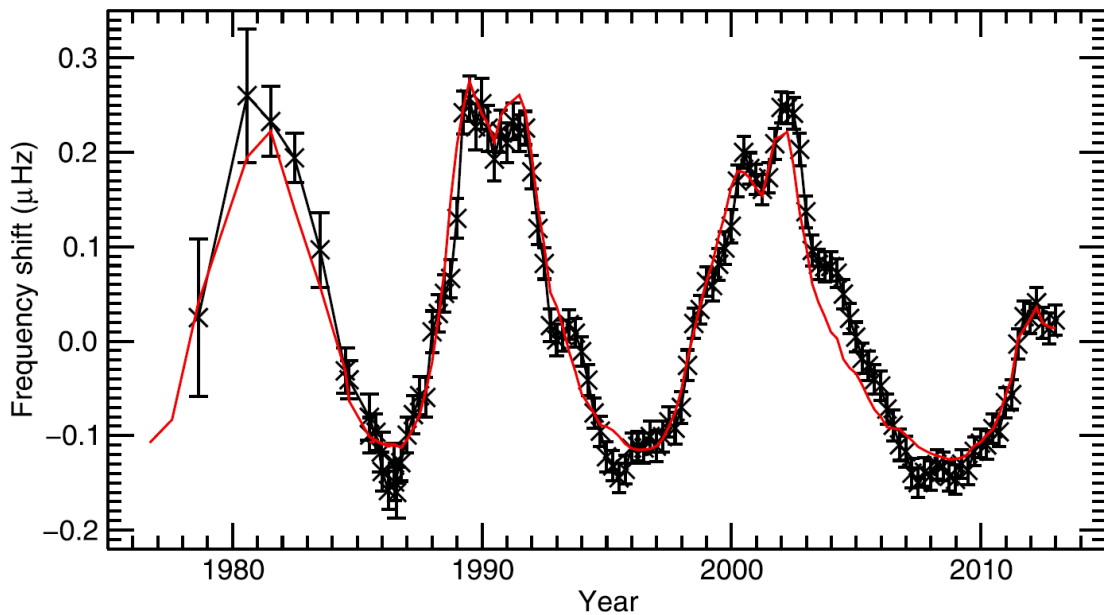


Figure 1.2: Average frequency shifts from solar cycle 21 to 23 for the $\ell = 0, 1$, and 2 modes with frequencies between 2.5 mHz and 3.5 mHz, calculated by using time series of 365 days and overlapped by 91.25 days, as obtained from the BiSON network (Chaplin et al. 2002). Overplotted in red is a scaled and shifted version of the 10.7 cm radio flux, which is used as a proxy for solar activity (taken from Figure 1 of Broomhall et al. 2014).

1.2 Modeling approaches

One of the main difficulties in understanding the variability of the acoustic oscillations results from the fact that modeling the complex and heterogeneous structures of magnetic activity near the surface of a star is not at all an easy task. It is usual to tackle the problem by means of perturbative approaches, for example by considering magnetic activity as a small steady perturbation to an otherwise spherically symmetric stellar model, and then calculating the linear changes to the acoustic wavefield using the first Born approximation². Several applications using linear perturbation theory are found in the literature that either deal with a localized perturbation (Santos et al. 2012) or a latitudinal distribution of activity (see, *e.g.*, Chaplin et al. 2008).

These approaches, however, suffer from several issues. Accurate modeling of a magnetic structure is overwhelming, and even creating a single self-consistent magnetohydrostatic model of a sunspot is not trivial (Moradi et al. 2010), therefore the direct effect of magnetic fields is often neglected and the perturbations only treat the hydrostatic changes in the stellar stratification. Even more importantly, the changes caused by magnetic activity at the surface are in general not small, especially in those regions where the ratio of the gas to the magnetic pressure (that is the so-called plasma β) is near or below the unity,

²There are two separate level of linearization here. One is the approximation of linear acoustic waves, which permits us to linearize the equation describing the propagation of waves, namely the wave equation. The other is the Born approximation, where one considers the changes in a background model as small and uses a perturbative approach to calculate the linear perturbed solutions using the ones from the unperturbed background model.

therefore the linear approach may be not correct. Last but not least, magnetic structures evolve with time: in the Sun we see new sunspots and active regions that emerge, diffuse, and then dissipate in time scales of months and almost continuously in periods of high activity. Moreover these structures rotate with the star, therefore their treatment as steady perturbations is highly questionable. A more appropriate way to address this problem is *forward* modeling, by using numerical simulations to directly solve the wave equation in complex media.

1.2.1 Time-domain simulations of linear oscillations

Numerical simulations of wave propagation are a crucial tool for modeling and interpreting helioseismic observations. They allow the study of complex phenomena in the solar interior and atmosphere, such as flows and magnetic heterogeneities that cover many temporal and spatial scales. The same simulations should find applications in the study of stellar oscillations as well.

With time-domain codes it is possible to simulate the propagation of acoustic waves inside 3D stellar models. In principle there are no restrictions in defining the properties of the model. For instance, we may compute the temporal evolution of the acoustic wavefield in the presence of many surface perturbations of different size and magnitude, mimicking starspots and active regions, with a surface distribution that reproduces the observed spatial coverage of activity as, *e.g.*, the butterfly diagram depicts in the case of the Sun or, in a wider context, spatial distributions observed in other stars with Doppler imaging or Zeeman Doppler imaging (Strassmeier 2009). Numerical simulations also allow us to characterize the influence of single localized perturbations beyond the perturbative approach.

Acoustic waves in the Sun and Sun-like stars have very low amplitudes compared with those of the background (Christensen-Dalsgaard 2002) and thus can be treated as weak perturbations with respect to a background reference model. The linearized oscillation equations can be solved as an eigenvalue problem (*e.g.* Monteiro 2009; Christensen-Dalsgaard 2008a) or through time-domain simulations. Here we are concerned with the time-domain simulations. Several linear codes exist in the framework of helioseismology (*e.g.* Khomenko and Collados 2006; Hanasoge and Duvall 2007; Parchevsky and Kosovichev 2007). Time-domain codes are particularly suited to problems in local helioseismology (see, *e.g.* Gizon et al. 2010; Gizon 2013). Among other applications they are used to characterize the propagation of waves through sunspots (Cameron et al. 2007, 2008) and active regions (Hanasoge 2008). Numerical simulations are also useful in assessing and validating observation techniques, such as far-side imaging (Hartlep et al. 2008), helioseismic holography and time-distance helioseismology (Braun et al. 2012).

Beyond the various uses in helioseismology, forward modeling finds useful applications also in asteroseismology. In observing other stars we do not have access to the rich amount of daily information available for the Sun, and magnetic activity only gives a weak signal in the observed low-degree modes. Therefore it is crucial to precisely characterize the seismic signature of magnetic structures in the observed light curves, and in this context numerical simulations are a powerful mean of investigation.

1.3 Results contained in this work

The maximum frequency variation in the acoustic modes corresponds to the maximum period of magnetic activity (as shown in Figure 1.2 for the Sun). In this period the surface of the star is continuously populated by starspots and active regions that give the major contributions to surface magnetism, therefore the changes in global low-degree modes likely arise from the net interaction of the acoustic oscillations with these structures. As the realistic modeling of the whole surface activity has a considerable degree of complexity, a first simple approach focusing on the characterization of the acoustic signature from a single strong localized structure is preferable. This problem is already interesting *per se*, for it opens the possibility to observing such structures in other stars with asteroseismology.

Most of the results contained in this work concern the use of forward modeling to characterize the effect of localized structures on global modes in stellar models. A significant part consisted of developing the GLobal Acoustic Spherical Simulator (GLASS), a code that simulates the propagation of linear acoustic waves in a spherical 3D domain encompassing the full star. GLASS takes the legacy of the code developed by Hanasoge et al. (2006) and extends it to include a treatment for the center of the star. The use of the linear approximation in describing the propagation of acoustic waves inside Sun-like stars is justified by observations (Libbrecht 1988). The linear treatment conveniently simplifies the equations describing the evolution of the wavefield, moreover it allows us to design numerical codes with affordable computational costs. The alternative to performing a more realistic simulation solving the full nonlinear set of equations on the entire star is computationally impossible at the time of writing, due to the range of the many different scales of the physical mechanisms in place and to the stellar stratification induced in the physical quantities (*e.g.*, in the density, which spans over more than ten orders of magnitude between the center and the surface of the star). Linear codes, however, come with some complications: they need a stable background model to produce numerical solutions that do not grow exponentially with time. The reality yet is different: all stars contain dynamical instabilities of hydrodynamic or magnetic origin. Convection is the main source of instability.

In chapter 2 I consider the problem of convective stabilization in numerical simulations. Various techniques exist to build convectively stable models in the frame of helioseismology, but they are usually tuned to a specific problem. Moreover most of these techniques only deal with the near surface convection (see, *e.g.*, Hanasoge et al. 2006) and the resulting stellar models still contain convective instabilities on time scales of ~ 10 days. This is not acceptable in the view of comparing simulation results with the long-term observations of months performed with satellites. Starting from a convectively unstable stellar model, I first devise a general method to build a stable model while retaining the hypothesis made for the original model (*e.g.*, the condition of hydrostatic equilibrium of the star). I then focus on the changes that stabilization produces in the acoustic wavefield, and I ask whether it is possible to correct for these changes. Based on a perturbative approach I propose a method to approximately recover the wavefield solutions for the original unstable model: this is done at the cost of performing an additional simulation that, depending on the method employed in stabilizing the background, exploits the numerical solution calculated for the stable model to build a source term driv-

ing the additional simulation. The method is tested using the standard 1D solar Model S (Christensen-Dalsgaard et al. 1996).

Chapter 3 is devoted to exploring the nonmagnetic effects induced by a starspot on the global acoustic modes beyond the linear regime. In this sense, this work extends previous investigations conducted in the linear regime (Santos et al. 2012; Chaplin et al. 2007a) to stars with higher levels of activity. For the study I consider a single starspot with a polar geometry, a configuration similar to that observed in a young solar analogue by means of Doppler imaging (Marsden et al. 2005). The starspot is modeled as a 3D change in the sound speed stratification of the star with respect to a convectively stable and spherically symmetric solar model, defined in chapter 2. Here I also describe the numerical method used in GLASS. I introduce the governing equations of wave motion and explain the technique devised to implement a treatment of the center of the star. This includes dealing with the numerical issues associated with the geometrical singularities in a spherical coordinates system. The code is validated against a spherically symmetric model through independent calculations of its theoretical modes of oscillations. The interaction of the acoustic wavefield with the polar spot is explored both in the linear regime and in the nonlinear regime with GLASS. Finally, as an application to asteroseismology, the signature that the starspot would produce in an asteroseismic observation is characterized, by using the wavefield to construct a synthetic light curve.

Chapter 4 extends the study conducted in the previous chapter to include the effect of rotation, and concerns the characterization of the asteroseismic signature of a large active region. For the active region a simple two-parameter model is used, which accounts for amplitude of the perturbation and surface coverage, and defines a localized surface perturbation. As a consequence of rotation the perturbation is not steady, but rotates with the star, therefore one must take into account the effect of both rotation and the active region at the same time.

In the linear regime of the perturbation the problem is solved by following the same approach that Goode and Thompson (1992) used to search for the signal in the acoustic oscillation frequencies of a magnetic field deeply buried in the convection zone of the Sun. The nonlinear regime is explored by means of numerical simulations using the GLASS code.

2 Propagating linear waves in convectively unstable stellar models: A perturbative approach

The content of this chapter appeared as “*Propagating linear waves in convectively unstable stellar models: a perturbative approach*” by E. Papini, L. Gizon, and A. C. Birch in *Solar Physics* 289, pp. 1919-1929, 2014, DOI:10.1007/s11207-013-0457-7. The final publication is available at <http://link.springer.com/article/10.1007/s11207-013-0457-7>. I designed research together with L. Gizon and A. Birch. I carried out the analysis and the numerical calculations and I wrote most of the text. This work is supported by SFB 963 “Astrophysical Turbulence and Flow Instabilities” (Project A18). I used mode frequencies provided by the BiSON network, funded by the UK Science and Technology Facilities Council (STFC).

Chapter summary

Linear time-domain simulations of acoustic oscillations are unstable in the stellar convection zone. To overcome this problem it is customary to compute the oscillations of a stabilized background stellar model. The stabilization, however, affects the result. Here we propose to use a perturbative approach (running the simulation twice) to approximately recover the acoustic wave field, while preserving seismic reciprocity. To test the method we considered a 1D standard solar model. We found that the mode frequencies of the (unstable) standard solar model are well approximated by the perturbative approach within $1 \mu\text{Hz}$ for low-degree modes with frequencies near 3 mHz. We also show that the perturbative approach is appropriate for correcting rotational-frequency kernels. Finally, we comment that the method can be generalized to wave propagation in 3D magnetized stellar interiors because the magnetic fields have stabilizing effects on convection.

2.1 Background stabilization in time-domain simulations

A stable background model is required to prevent numerical solutions that grow exponentially with time. Stellar models, however, always contain dynamical instabilities, which can be of hydrodynamic and/or magnetic nature. These instabilities must be removed. The main source of instability in stars is convection. Some magnetic configurations can

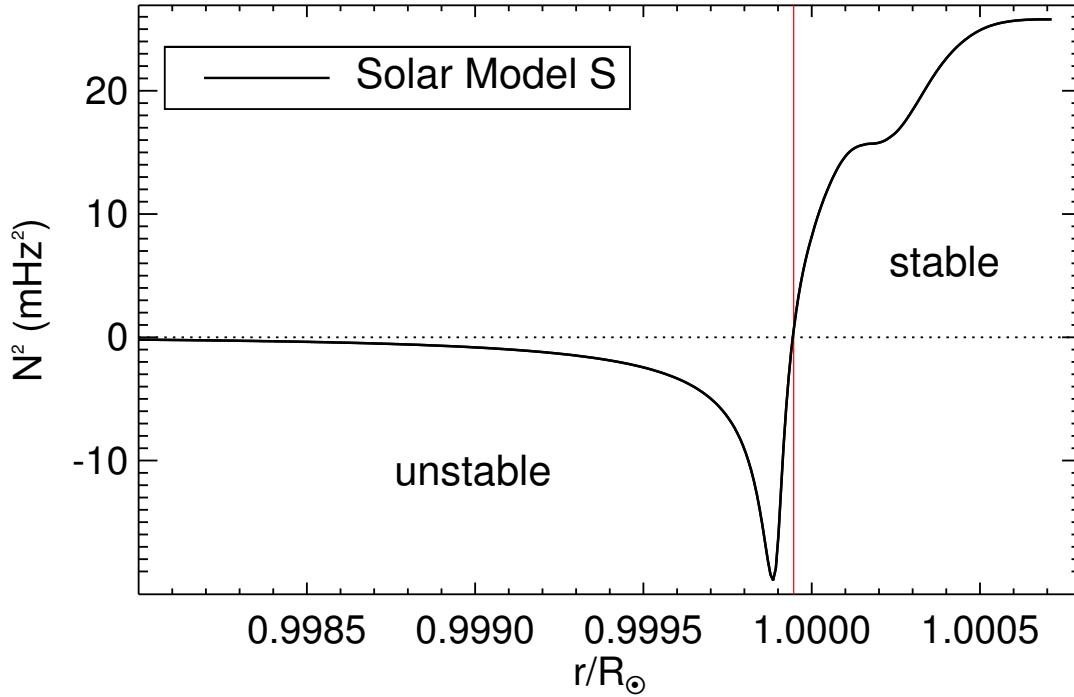


Figure 2.1: Square of the buoyancy frequency for Model S (solid black line) in the upper part of the convection zone and the atmosphere: the negative peak corresponds to the superadiabatic layer, located just below the photosphere. The vertical red line divides stable and unstable zones.

also be unstable (*e.g.*, Tayler 1973), although the magnetic field often has a stabilizing effect on convection (Gough and Tayler 1966; Moreno-Insertis and Spruit 1989).

For the hydrodynamic case, the Schwarzschild criterion (Schwarzschild 1906) for local convective stability is

$$\frac{1}{\Gamma} - \frac{d \ln \rho}{d \ln P} < 0, \quad (2.1)$$

where ρ , P , and Γ are density, pressure, and first adiabatic exponent. This criterion for convective stability can be reformulated to explicitly include gravity $\mathbf{g}(\mathbf{r})$ by introducing the Brunt–Väisälä or buoyancy frequency N :

$$N^2 \equiv -\mathbf{g} \cdot \mathbf{A} > 0, \quad (2.2)$$

where

$$\mathbf{A}(\mathbf{r}) \equiv \nabla \ln \rho - \frac{1}{\Gamma} \nabla \ln P \quad (2.3)$$

is the Schwarzschild discriminant at position \mathbf{r} . In the solar case, the square of the buoyancy frequency is marginally negative in the convection zone, except for a strong negative peak in the highly superadiabatic layer just below the surface. Figure 2.1 shows the squared buoyancy frequency in the upper part of the solar convection zone for Model S (Christensen-Dalsgaard et al. 1996).

To perform time-domain simulations we need to modify the model in order to obtain a non-negative N^2 everywhere. Various examples can be found in the literature. Hanasoge et al. (2006) replaced the near-surface layer above $0.98R_\odot$ with an empirical model that satisfies convective stability while preserving hydrostatic equilibrium, allowing stable simulations to be extended over a temporal window of several days. Hartlep et al. (2008) neglected the terms containing \mathbf{A} in the momentum equation because they did not affect the frequencies in their range of investigation. Shelyag et al. (2006) assumed a constant adiabatic exponent $\Gamma = 5/3$ of a perfect gas and then adjusted pressure and density to reach convective stability and hydrostatic equilibrium. Parchevsky and Kosovichev (2007) chose a non-negative profile of N^2 and then calculated the corresponding density profile that satisfied hydrostatic equilibrium. Schunker et al. (2011) constructed Convectively Stable Models (CSM) by taking Model S as reference and modifying the sound speed before stabilizing it, such that the mode frequencies of the new stable model are close to those of Model S.

Stabilization, unfortunately, modifies the solutions for the wave field, and the question arises of how to correct the results that we obtain from the simulations, in order to recover the solutions for the original model of the star. We propose here a perturbative approach that numerically corrects for the changes in the wave field caused by stabilizing the background model, and approximate the correct solutions of the original unstable model. This is a step toward direct comparison of synthetic data with data from observations (*e.g.* observations from the *Helioseismic and Magnetic Imager*; Scherrer et al. 2012).

2.2 Proposed solution: A perturbative approach

2.2.1 Constructing convectively stable background models

The linearized equation of motion describing the propagation of acoustic waves inside a star has the general form

$$\mathcal{L}\xi(\mathbf{r}, t) = \mathbf{S}(\mathbf{r}, t), \quad \mathcal{L} = \rho\partial_t^2 + \mathcal{H} \quad (2.4)$$

where \mathbf{r} is the position vector, t is time, \mathcal{H} is a linear spatial operator associated with the background stellar model, $\xi(\mathbf{r}, t)$ is the vector wave displacement, and $\mathbf{S}(\mathbf{r}, t)$ is a source function that represents forcing by granulation. In the adiabatic case, \mathcal{H} takes the form

$$\mathcal{H}\xi = \nabla p' + \rho \left(\xi \cdot \mathbf{A} - \frac{p'}{\Gamma P} \right) \mathbf{g} - \rho \mathbf{g}' - \mathbf{F}', \quad (2.5)$$

where primes refer to wave perturbations and the term \mathbf{F}' accounts for the interaction of waves with flows and magnetic fields. Solutions of Equation (2.4) are uniquely determined once the initial and boundary conditions are set. Note that when $\mathbf{F}' = 0$ the operator \mathcal{H} is Hermitian and symmetric (Lynden-Bell and Ostriker 1967).

Let us choose a reference unstable model, *e.g.* solar Model S, which is labeled “ref” throughout this article. We construct a convectively stable model defined by the new quantities ρ_0 , P_0 , and Γ_0 . These quantities are obtained from the original reference model by imposing $N_0^2 \geq 0$. The simplest choice is to set $N_0^2 = 0$ where N_{ref}^2 is negative, but

other choices are possible. We define the differences between the stable and the reference models by

$$\Delta\rho = \rho_{\text{ref}} - \rho_0, \quad \Delta P = P_{\text{ref}} - P_0, \quad \Delta\Gamma = \Gamma_{\text{ref}} - \Gamma_0. \quad (2.6)$$

The difference in the squared buoyancy frequency is then $\Delta N^2 = N_{\text{ref}}^2 - N_0^2$.

Stabilization can be achieved in different ways. In the spherically symmetric case and with the hydrostatic equilibrium condition, stellar models are entirely described by two independent physical quantities (if no flows and no magnetic fields are present): for example, the density $\rho_0(r)$ and the first adiabatic exponent $\Gamma_0(r)$. When ρ_0 and Γ_0 are specified, the pressure is given by

$$\frac{dP_0}{dr} = -\rho_0(r)g_0(r), \quad (2.7)$$

where $g_0(r) > 0$ is the acceleration of gravity, which is fixed by $\rho_0(r)$.

Stabilization by changing Γ_{ref} is a simple procedure. On the other hand, changing the density requires solving a nonlinear boundary-value problem, involving Equations (2.2) and (2.7) with the new stable N_0^2 (*e.g.* Parchevsky and Kosovichev 2007). In the latter case a smart choice of the boundary conditions must be made to preserve the main properties of the star (such as total mass and radius). Changing both Γ_{ref} and ρ_{ref} is allowed and desirable, but it is not a straightforward procedure and we do not explore this possibility further in this work.

The linearized equation of motion for the stable model takes the form:

$$\mathcal{L}_0 \xi_0(\mathbf{r}, t) = \mathbf{S}(\mathbf{r}, t), \quad \mathcal{L}_0 = \rho_0 \partial_t^2 + \mathcal{H}_0, \quad (2.8)$$

where \mathcal{H}_0 is the operator associated with the new stable model and ξ_0 is the corresponding wave-field solution.

We stress that convective stabilization must be applied consistently with the hypothesis made for the model; we also note that density, pressure, and first adiabatic exponent must be changed in Equation (2.5) and all other equations, not only in **A**.

2.2.2 First-order correction to the wave field

Assuming that a first simulation to solve Equation (2.8) is performed and the solution ξ_0 for the stable model is computed, we write the approximate solution ξ for Equation (2.4) as

$$\xi(\mathbf{r}, t) = \xi_0(\mathbf{r}, t) + \Delta\xi(\mathbf{r}, t), \quad (2.9)$$

where $\Delta\xi$ represents the first-order correction to ξ_0 toward the unstable model. This correction is given by

$$\mathcal{L}_0 \Delta\xi(\mathbf{r}, t) = -\Delta\mathcal{H}\xi_0(\mathbf{r}, t), \quad (2.10)$$

where the operator $\Delta\mathcal{H}$ is the first correction to the wave operator, obtained by collecting the first-order terms in $\mathcal{L}_{\text{ref}} - \mathcal{L}_0$. In practice, the correction $\Delta\xi$ is obtained by running a second simulation using the same background model \mathcal{L}_0 but with a source term $-\Delta\mathcal{H}\xi_0(\mathbf{r}, t)$. Figure 2.2 sketches the steps of the method. The main advantage of this method is that it is well defined, uses computational tools, and does not require fine-tuning of the stabilization to match the observations (*e.g.* as in Schunker et al. 2011).

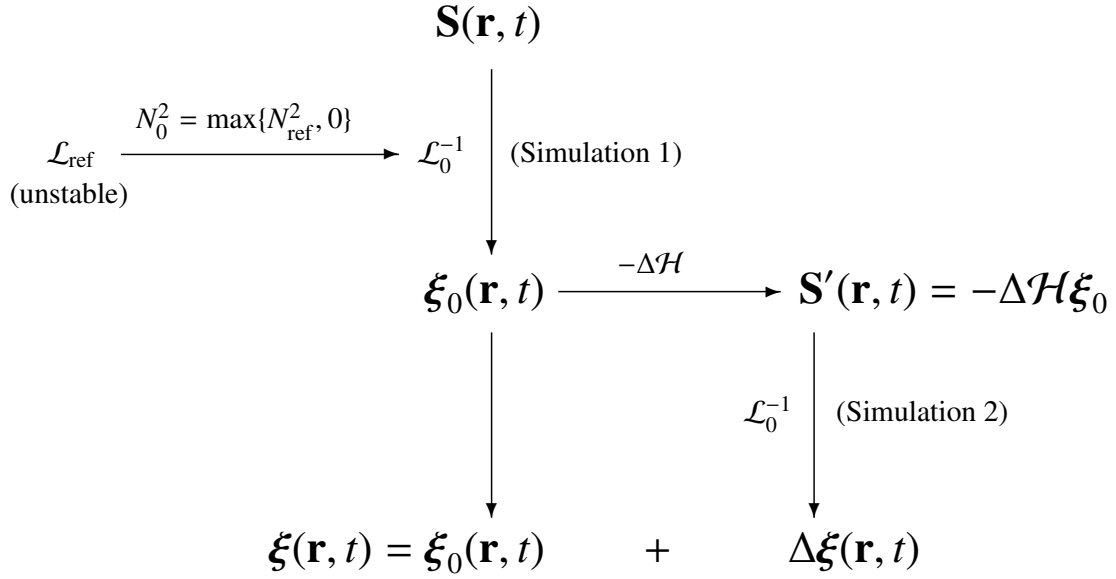


Figure 2.2: The steps of the proposed method. Here \mathcal{L}_0^{-1} mathematically represents the operation performed by the simulations. A stable model is built from \mathcal{L}_{ref} . The solution for the stable model is computed (Simulation 1), and is used to compute the driving source \mathbf{S}' (with $-\Delta\mathcal{H}$). A second simulation is run (Simulation 2) to find the correction $\Delta\xi$ toward the unstable model. Refer to Equations (2.8) and (2.10) for the symbols.

Applying the correction doubles the computational cost. Whether this cost is worth it or not depends on the application. For example, in the future we intend to use the simulations to study the effect of active regions on low-degree modes. Such a small effect (less than a μHz) is at the level of the first-order correction in the background model.

To assess the validity of the method, one needs to estimate whether the perturbations invoked in Equations 2.9 and 2.10 are weak. To do so, we need to write an approximation for the operator $\Delta\mathcal{H}$ as a function of the change in N^2 . By inspection of the wave operator (Equation (2.5)), we see that an essential term is

$$\Delta\mathcal{H}\xi \approx \rho_0(\xi \cdot \Delta\mathbf{A})\mathbf{g} = \rho_0\xi_r\Delta N^2\hat{r}, \quad (2.11)$$

such that the first-order correction to the mode frequencies may be approximated by (*e.g.*, Aerts et al. 2010)

$$\frac{\Delta\omega}{\omega_0} \approx \frac{\int_{\odot} \Delta N^2 \xi_r^2 \rho_0 dV}{2\omega_0^2 \int_{\odot} \|\xi\|^2 \rho_0 dV}, \quad (2.12)$$

and the relative correction in the mode frequencies is a weighted average of $\Delta N^2/2\omega^2$. For the first-order perturbation theory to work, we should have $\Delta N^2/2\omega^2 \lesssim 1$. Figure 2.3 shows $\Delta N^2/2\omega^2$ for $\omega/2\pi = 3$ mHz in the case of solar Model S, which is based on a mixing-length treatment of convection. This quantity is well below unity throughout the convection zone, except in a localized region near the surface (the highly superadiabatic layer) where it reaches 1.1 for $\omega/2\pi = 3$ mHz. As frequency decreases, $\Delta N^2/2\omega^2$ increases; however low-frequency modes are also less sensitive to surface perturbations. Therefore, we expect the first-order perturbation theory to work reasonably well for the full spectrum of solar oscillations. This is shown for particular cases in the following sections.

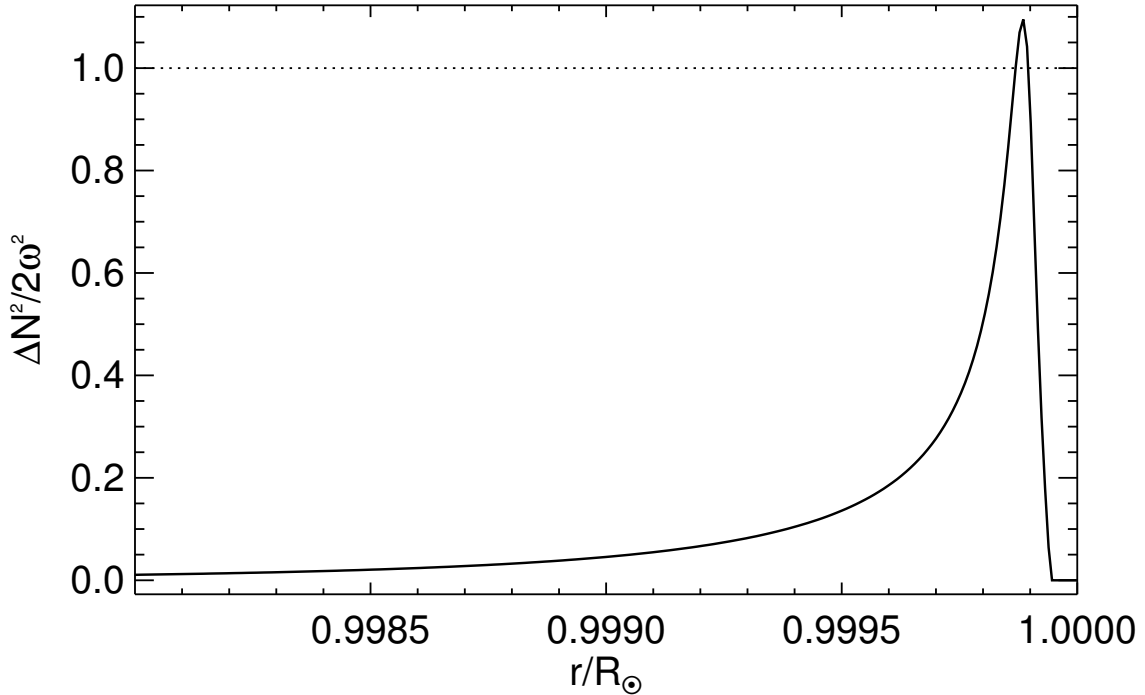


Figure 2.3: $\Delta N^2/2\omega^2$ in the upper part of the convection zone (solar Model S) for a frequency of $\omega/2\pi = 3$ mHz.

We note that seismic reciprocity (Dahlen and Tromp 1998) is preserved to first order, since both \mathcal{H}_0 and $\Delta\mathcal{H}$ are Hermitian and symmetric operators in the absence of flows and magnetic fields (Lynden-Bell and Ostriker 1967). The concept of seismic reciprocity can be extended to include flows and magnetic fields (see Hanasoge et al. 2011, and references therein).

Seismic reciprocity is a key property of the adjoint method used to solve the inverse problem in seismology (*e.g.* Tromp et al. 2005; Hanasoge et al. 2011).

Modified background models employed by Hanasoge et al. (2006), Shelyag et al. (2006) and Parchevsky and Kosovichev (2007) all satisfy reciprocity. By contrast, seismic reciprocity is not automatically enforced in the model of Hartlep et al. (2008), which neglects the term \mathbf{A} in the momentum equation and in the CSM solar models of Schunker et al. (2011), which are not hydrostatic.

2.3 Testing the method in 1D for the Sun

We tested the method in the 1D hydrodynamic case for the Sun, starting from standard solar Model S (Christensen-Dalsgaard et al. 1996). For the test we used the ADIPLS code (Christensen-Dalsgaard 2008a), which solves the adiabatic stellar oscillation equations for a spherically symmetric stellar model in hydrostatic equilibrium as an eigenvalue problem (not in the time domain). This allows one to compute the exact solution for unstable models, and hence directly measure the accuracy of the correction discussed in Section 2.2.

Writing the solution in the form

$$\xi(\mathbf{r}, t) = \xi_{n\ell m}(\mathbf{r})e^{-i\omega_{nl}t}$$

and setting $\mathbf{S} = \mathbf{0}$, we have

$$\mathcal{H}\xi_{n\ell m}(\mathbf{r}) = \rho\omega_{nl}^2\xi_{n\ell m}(\mathbf{r}), \quad (2.13)$$

where ω_{nl} is the acoustic mode frequency and $\xi_{n\ell m}(\mathbf{r})$ the corresponding eigenvector displacement (in the following we omit the $n\ell m$ subscripts for clarity). Each solution is uniquely identified by three integers: the radial order n , the angular degree ℓ , and the azimuthal order m , where $|m| \leq \ell$ (in the spherically symmetric case that we consider here the solutions are degenerate in m).

For our purpose the operator \mathcal{H} can be written as

$$\begin{aligned} \mathcal{H}\xi = & -\nabla(\Gamma P \nabla \cdot \xi) - \nabla(\xi \cdot \nabla P) \\ & + \frac{\nabla P}{\rho} \nabla \cdot (\rho \xi) + \rho G \nabla \left(\int_{\odot} \frac{\nabla_{\mathbf{r}'} \cdot (\rho \xi)}{\|\mathbf{r} - \mathbf{r}'\|} dV' \right), \end{aligned} \quad (2.14)$$

where G is the universal gravitational constant; magnetic fields and flows are not present (see Equation (2.5)) and every wave perturbation to pressure and gravity is expressed in terms of ξ .

2.3.1 Acoustic modes

For the test we chose to construct a stable model by only changing Γ in Model S to obtain $N_0^2 = \max\{N_{\text{ref}}^2, 0\}$. This was made by setting the first adiabatic exponent Γ_0 to

$$\Gamma_0(r) = \begin{cases} \Gamma_{\text{ref}}(r) & \text{where } N_{\text{ref}}^2 \geq 0 \\ d \ln P_{\text{ref}} / d \ln \rho_{\text{ref}} & \text{where } N_{\text{ref}}^2 < 0, \end{cases} \quad (2.15)$$

where ρ_{ref} , P_{ref} , and Γ_{ref} refer to Model S. The density and pressure remained unchanged, *i.e.* $\rho_{\text{ref}} = \rho_0$ and $P_{\text{ref}} = P_0$. Figure 2.4 show a plot of $\Gamma_0(r)$ in the upper part of the convection zone, at the superadiabatic layer. The corresponding change in the sound-speed stratification is plotted in Figure 2.5.

Solutions for the stable model were computed with ADIPLS, and we calculated the corrections to the eigenfrequencies by using

$$\Delta \mathcal{H}\xi_0 = -\nabla(\Delta \Gamma P_0 \nabla \cdot \xi_0). \quad (2.16)$$

We note that $\Delta \mathcal{H}$ is Hermitian and symmetric. Given the eigensolutions (ξ_0, ω_0^2) for the stable model, we then calculated the first-order correction to the change in the eigenfrequencies.

Test results are shown in Figures 2.6 and 2.7. Figure 2.6 shows the solar échelle diagram for the $\ell = 0$ modes. The correction moves the mode frequencies from the stable model toward Model S. Observed frequencies from the *Birmingham Solar-Oscillations Network* (BiSON) (Chaplin et al. 2002) are plotted for comparison.

Figure 2.7 shows the plot of mode-frequency differences (for the $\ell = 0, 200$, and 500 modes) between the stable model and Model S and the residual differences between

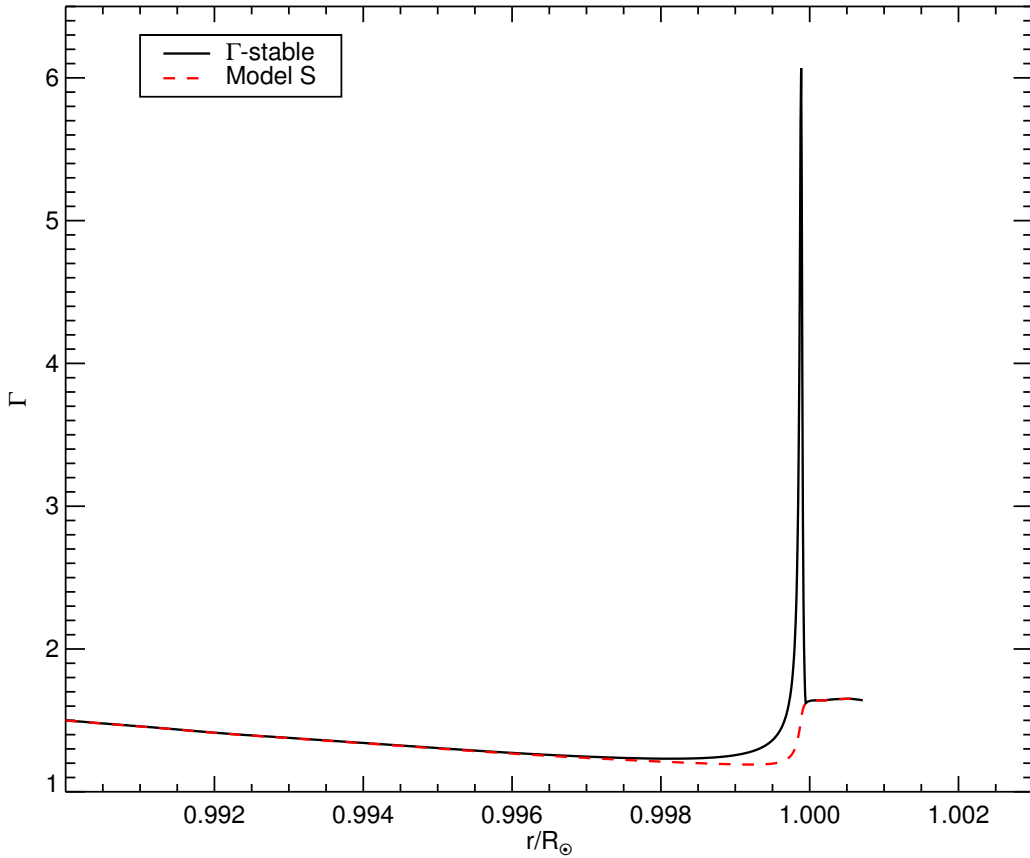


Figure 2.4: First adiabatic exponent Γ_{ref} near the surface for Model S (red dashed line) and Γ_0 resulting from Equation (2.15) (black solid line).

the corrected frequencies and frequencies of Model S. The correction brings the mode frequencies much closer to the values of the original model: the difference between the corrected frequencies and those of the reference model is two orders of magnitude smaller than the difference between the stable and the reference model at 1 mHz. The correction is not as efficient as the frequency increases, but still at the level of one order of magnitude at high frequencies. That is because as frequency increases acoustic modes are more sensitive to the near surface, where the strongest changes to the model are present. The mode-frequency differences between the stable model and – Model S increase with ℓ since high-degree modes are more sensitive to the surface layers (see $\ell = 200$ and 500 in Figure 2.7). The first-order correction reduces these frequency differences by a factor of ten. In Figure 2.8 we display the radial displacement eigenfunctions for the mode $\ell = 500$ and $n = 4$. We see that the first-order correction brings the phase and amplitude of the corrected eigenfunction closer to those of Model S.

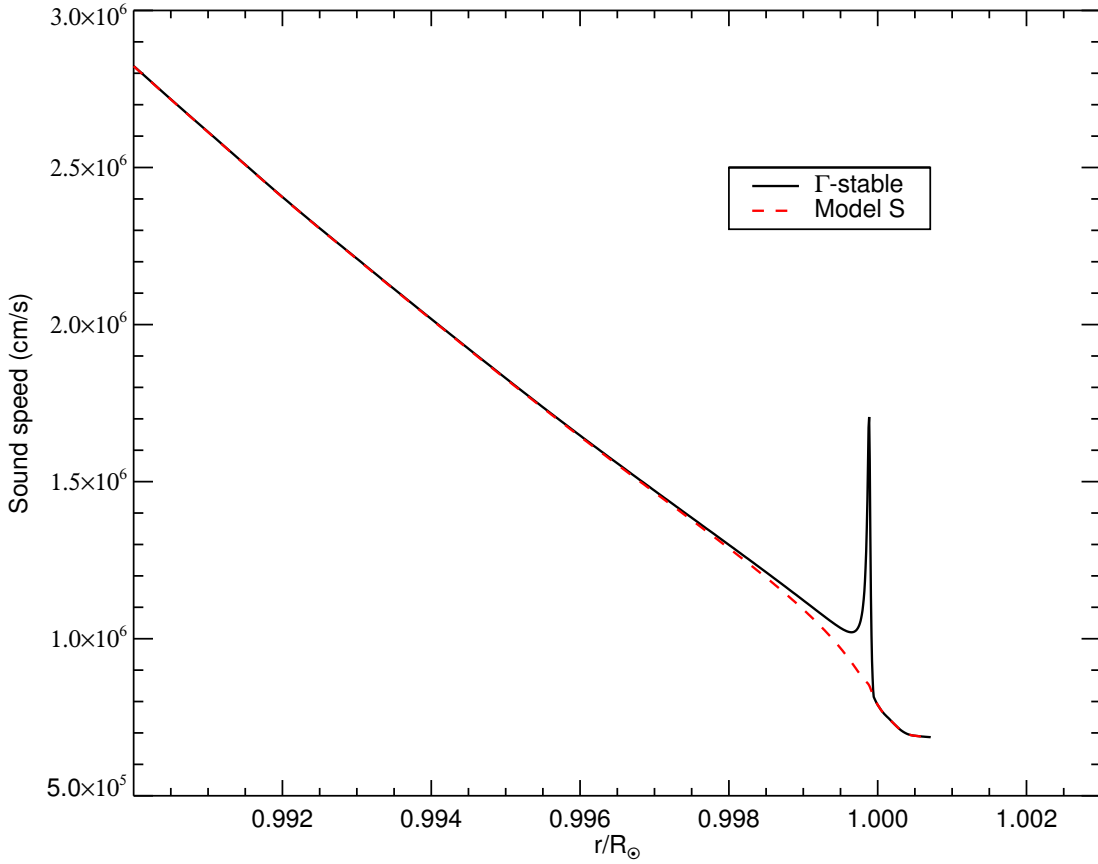


Figure 2.5: Radial profile of the adiabatic sound speed near the surface for Model S (red dashed line) and for the stable model resulting from Equation (2.15) (black solid line).

2.3.2 Rotational sensitivity kernels

We furthermore assessed the ability of the method to correct the eigenfunctions by testing with rotational kernels. In the presence of rotation, frequencies are no longer degenerate in the azimuthal order m . In the case of rotation constant on spheres, the rotational splitting frequency is

$$S_{n\ell} \equiv \frac{\omega_{n\ell m} - \omega_{n\ell 0}}{m} = \int_0^R K(\xi_{n\ell}, r) \Omega(r) dr \quad (2.17)$$

where $\Omega(r)$ is the angular velocity at radius $r \leq R$ and K is the rotational kernel (Hansen et al. 1977). The kernel for mode (n, ℓ) depends on $\xi_{n\ell}$ and the density profile. With ADIPLS we can directly calculate rotational splitting in the case of a rotation profile that only depends on r .

The first-order correction in the rotational splitting frequency as a result of stabilization is

$$\Delta S_{n\ell} = \int_0^R \Delta K_{n\ell}(r) \Omega(r) dr, \quad (2.18)$$

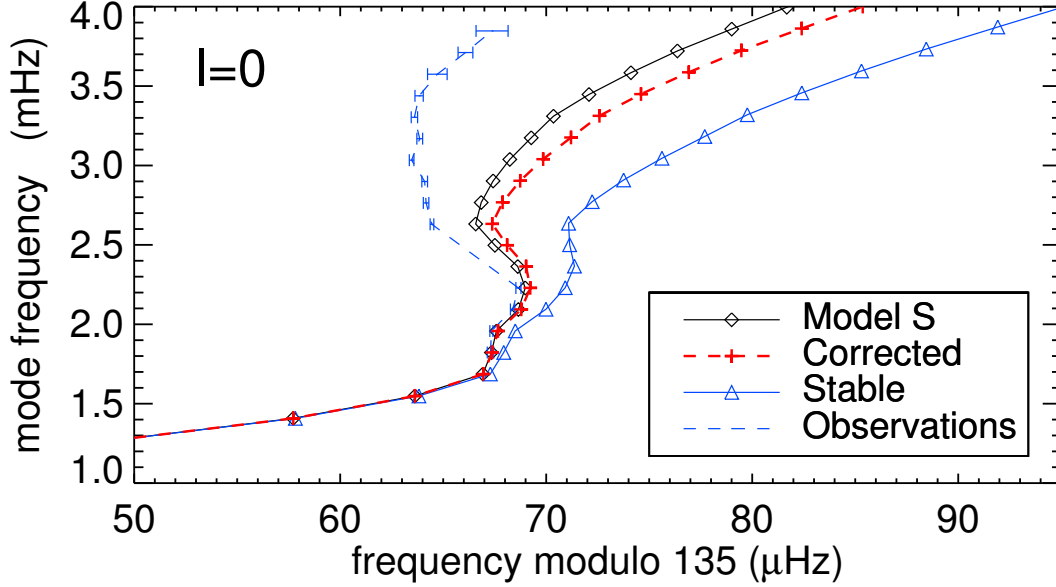


Figure 2.6: Echelle diagram showing mode frequencies modulo $135 \mu\text{Hz}$ for modes with $\ell = 0$ and $7 \leq n \leq 27$. The first-order correction (red dashed line and crosses) moves the mode frequencies back toward Model S (black solid line and diamonds) from the modified Γ -stable model (blue solid line and triangles). BiSON data (blue dashed line and error bars) from 108 days of observations starting from 7 February 1997 are plotted for comparison.

where the perturbation to the kernel can be computed numerically using

$$\Delta K_{n\ell}(r) = \lim_{\epsilon \rightarrow 0} \frac{1}{\epsilon} \left[K(\xi_{n\ell}^\epsilon, r) - K(\xi_{n\ell}^0, r) \right], \quad (2.19)$$

where $\xi_{n\ell}^\epsilon$ is the eigenvector that solves Equation (2.13) for $\mathcal{H} = \mathcal{H}_0 + \epsilon(\mathcal{H}_{\text{ref}} - \mathcal{H}_0)$ and ϵ is an infinitesimally small parameter. We calculated $\Delta K_{n\ell}$ numerically using $\epsilon = 10^{-5}$, in a linear regime where the result is independent of ϵ , within the numerical precision of ADIPLS.

Figure 2.9 shows the rotational kernel for the $\ell = 1, n = 25$ mode and the corrected kernel. We see that the phase and amplitude of the corrected kernel are closer to that of the Model S kernel.

To evaluate the accuracy of the correction, we computed the rotational splitting given by Equation (2.17) in the case of a solid rotation profile of $\Omega/2\pi = 0.5 \mu\text{Hz}$, for the $\ell = 1$ modes. The maximum difference $S_{n\ell}^{\text{ref}} - (S_{n\ell}^0 + \Delta S_{n\ell})$ between the corrected model and Model S is around 10^{-3} nHz, while the difference $S_{n\ell}^{\text{ref}} - S_{n\ell}^0$ between Model S and the stable model is one order of magnitude higher.

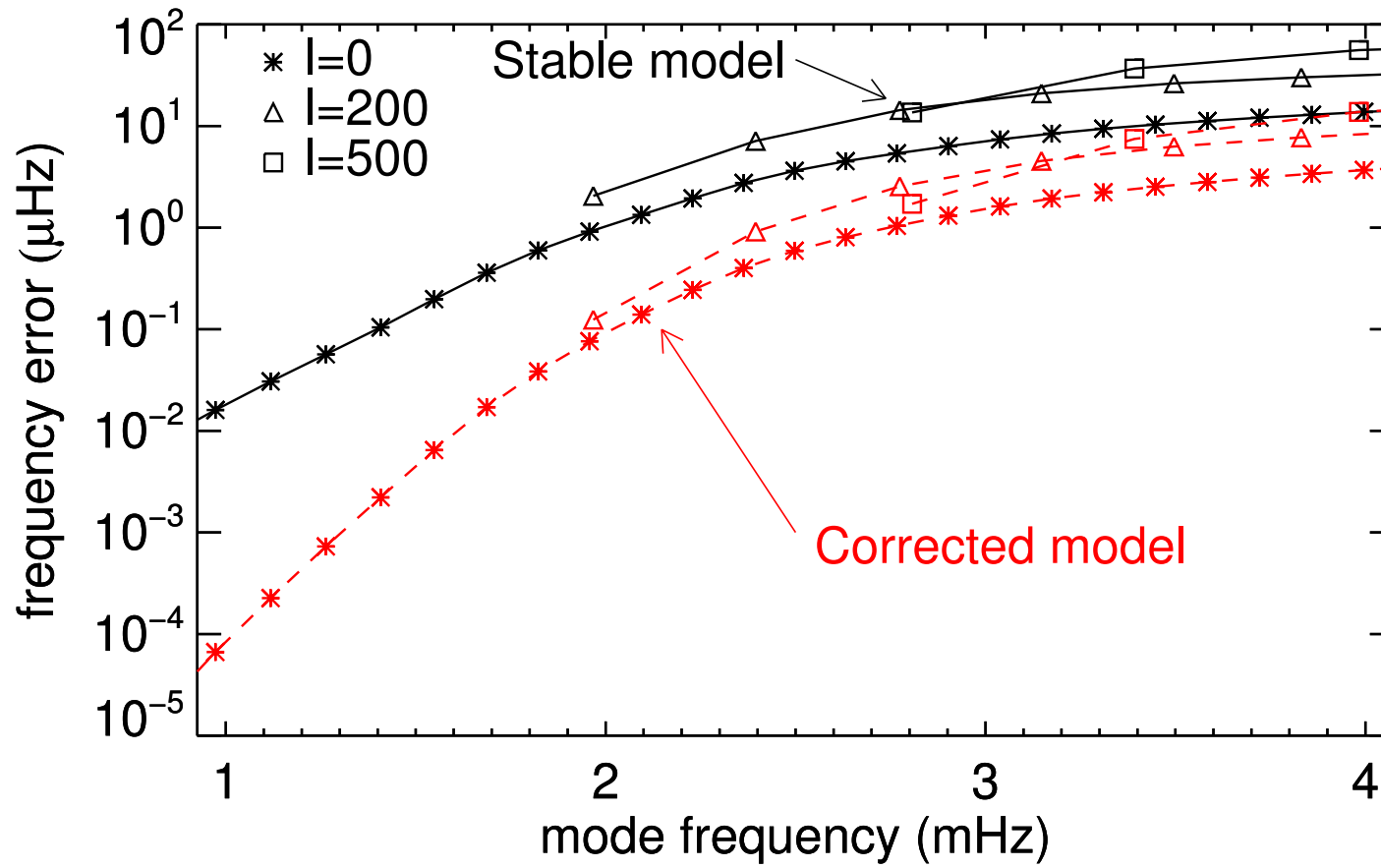


Figure 2.7: Mode-frequency error for acoustic modes with $\ell = 0, 200, \text{ and } 500$. Solid black line: difference $(\omega_0 - \omega_{\text{ref}})/2\pi$ between the Γ -stable model and Model S (reference model). Dashed red line: difference $(\omega_0 + \Delta\omega - \omega_{\text{ref}})/2\pi$ between the corrected frequencies and Model S.

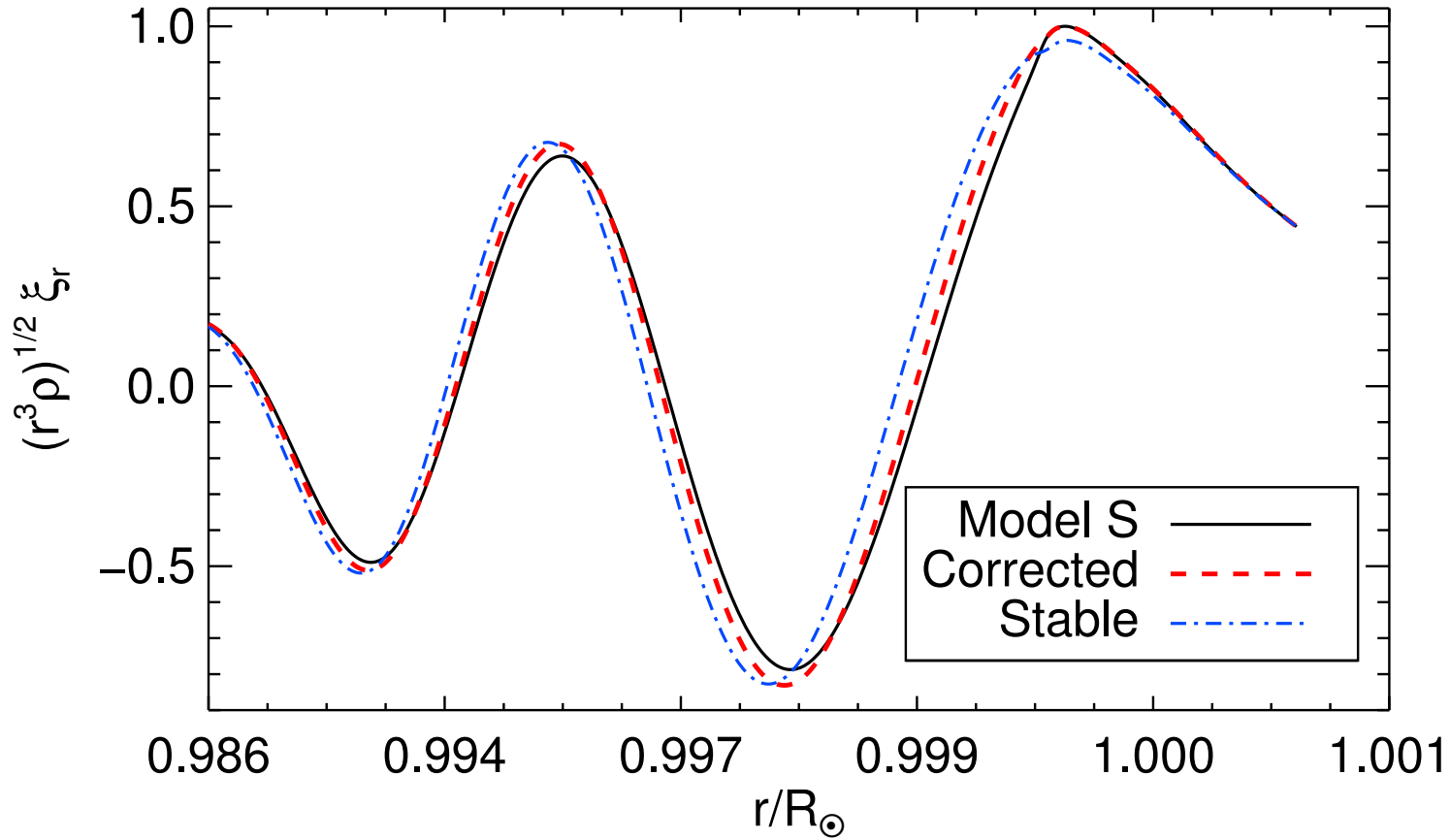


Figure 2.8: Radial displacement eigenfunction $(r^3 \rho)^{1/2} \xi_r$ for the $\ell = 500$ and $n = 4$ mode as a function of radius (constant grid spacing in acoustic depth). The solid black line is for Model S, the dash-dotted blue line for the stable model, and the dashed red line for the first-order correction. All three eigenfunctions are normalized with respect to the maximum value of the eigenfunction of Model S.

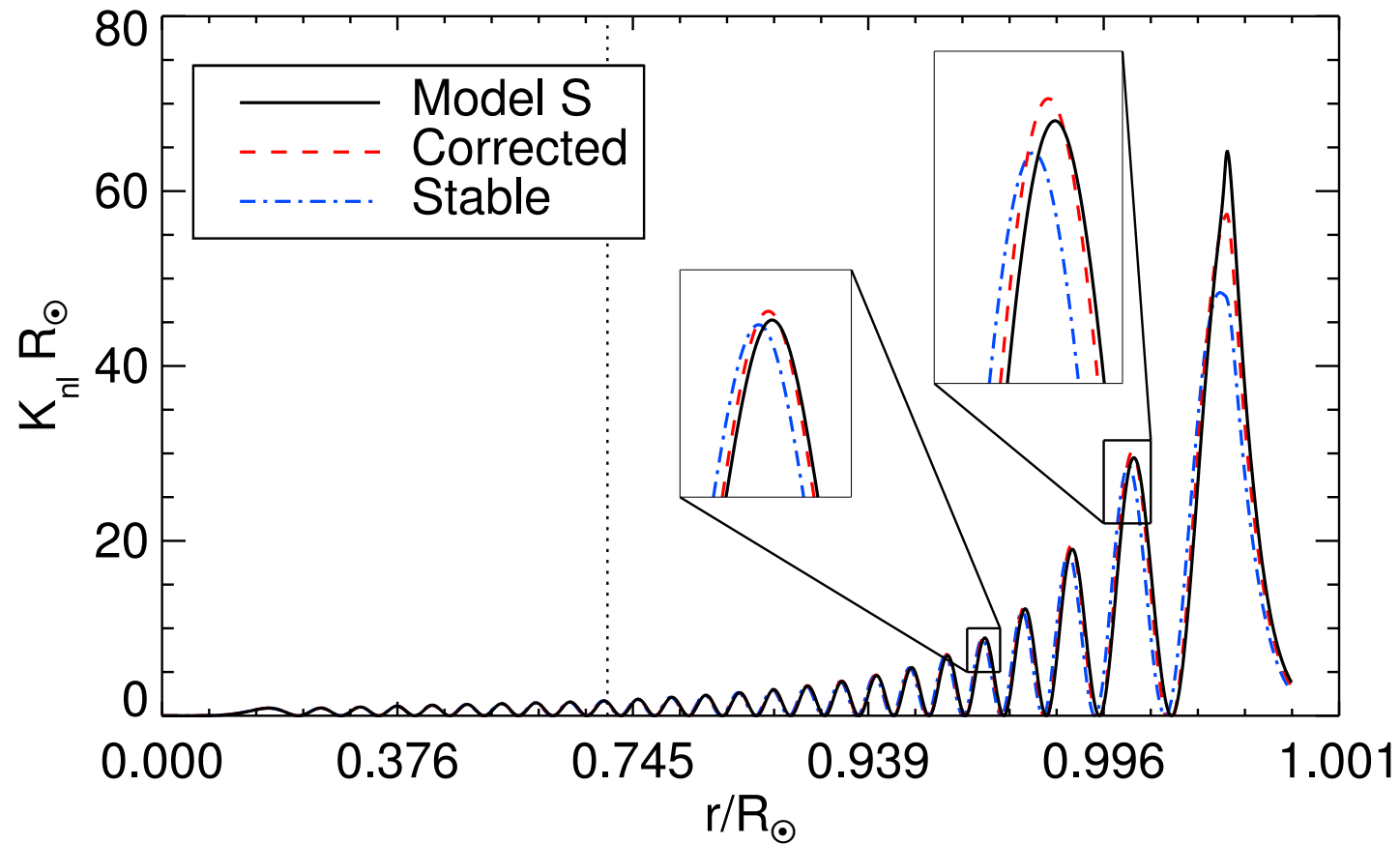


Figure 2.9: Rotational kernels for the $\ell = 1$ and $n = 25$ mode as a function of radius (constant grid spacing in acoustic depth). The vertical dotted line indicates the location of the base of the convection zone. The solid black line is the kernel for Model S, the dash-dotted blue line for the stable model, and the dashed red line for the first-order correction.

3 Simulating acoustic waves in spotted stars

The content of this chapter appeared as “*Simulating acoustic waves in spotted stars*” by E. Papini, A. C. Birch, L. Gizon, and S. M. Hanasoge in *Astronomy & Astrophysics*, 577, A145, 2015, DOI: 10.1051/0004-6361/201525842. Reproduced with permission from Astronomy & Astrophysics, © ESO. I designed research together with L. Gizon and A. Birch. I carried out the analysis and the numerical calculations and I wrote most of the text. This work is supported by SFB 963 “Astrophysical Turbulence and Flow Instabilities” (Project A18).

Chapter summary

Acoustic modes of oscillation are affected by stellar activity, however it is unclear how starspots contribute to these changes. Here we investigate the nonmagnetic effects of starspots on global modes with angular degree $\ell \leq 2$ in highly active stars, and characterize the spot seismic signature on synthetic light curves. We perform 3D time-domain simulations of linear acoustic waves to study their interaction with a model starspot. We model the spot as a 3D change in the sound speed stratification with respect to a convectively stable stellar background, built from solar Model S. We perform a parametric study by considering different depths and perturbation amplitudes. Exact numerical simulations allow the investigation of the wavefield-spot interaction beyond first order perturbation theory. The interaction of the axisymmetric modes with the starspot is strongly nonlinear. As mode frequency increases, the frequency shifts for radial modes exceed the value predicted by linear theory, while the shifts for the $\ell = 2, m = 0$ modes are smaller than predicted by linear theory, with avoided-crossing-like patterns forming between the $m = 0$ and $m = 1$ mode frequencies. The nonlinear behavior increases with increasing spot amplitude and/or decreasing depth. Linear theory still reproduces the correct shifts for nonaxisymmetric modes. In the nonlinear regime the mode eigenfunctions are not pure spherical harmonics, but rather a mixture of different spherical harmonics. This mode mixing, together with the frequency changes, may lead to misidentification of the modes in the observed acoustic power spectra.

3.1 Introduction

3.1.1 Motivation: Low degree stellar oscillations

Starspots are the main observed features of magnetic activity in stars and play a fundamental role in understanding stellar dynamos. They have been detected in many stars through the modulation of light curves (Mosser and Appourchaux 2009) and Doppler imaging (Strassmeier 2009), the latter suggesting polar and high- to mid-latitude concentrations of magnetic fields. García et al. (2010) unambiguously detected an activity cycle in a Sun-like star with asteroseismology for the first time, using data collected by the *Convection, Rotation & planetary Transits* (CoRoT) mission (Auvergne et al. 2009). Other excellent data are available from the *Kepler* (Borucki et al. 2010) satellite and even more will come from the upcoming missions *Transiting Exoplanet Survey Satellite* (TESS) to be launched in 2017 (Ricker et al. 2014), and *PLAnetary Transits and Oscillations of stars* (PLATO), to be launched in 2024 (Rauer et al. 2014).

The surface distribution of stellar magnetic activity, in principle, can be measured with asteroseismology. Gizon (2002) investigated the challenge of spatially resolving surface magnetic activity in other stars. He concluded that it would be possible to discriminate between a polar cap distribution and equatorial band distributions of activity, but only for stars with an inclination angle higher than 40° , activity stronger than the Sun, and rotation strong enough that the individual m -components in the acoustic spectra could be resolved. In a later study, using an empirical model calibrated to the Sun, Chaplin et al. (2007a) tested the ability to measure, with asteroseismology, the extension of a latitudinal activity band distribution in Sun-like stars, finding that the best prospects for detection are for stars with magnetic activity concentrated at low latitudes.

More recently Santos et al. (2012) studied the indirect (nonmagnetic) effects on radial acoustic oscillations induced by the changes in the stellar stratification due to starspots. In the case of the Sun they found that the frequency changes are too small (by two orders of magnitude) to explain the observed shifts. They concluded that the indirect effects of starspots on the stellar stratification cannot be responsible for the observed changes in the acoustic oscillations, at least for a star with a solar-like level of activity.

3.1.2 Our approach: Time-domain numerical simulations of waves and starspot

In this work we extend the investigation to starspots in stars with a higher level of activity: those stars likely have starspots with larger surface coverage, thus implying considerable changes in the internal stratification (*e.g.*, in the sound speed). We also explore the possibility of identifying starspots through asteroseismic observations of highly spotted stars. We address two main questions: what are the changes in the mode frequencies and amplitudes in such stars? And, what is the starspots seismic signature in synthetic light curves?

We simplify the problem by focusing on the interaction between the acoustic wavefield and a single starspot with a polar geometry (such a configuration is compatible with Doppler observations of a young solar analogue with strong activity, Marsden et al. 2005). For the starspot we model only the indirect changes induced in the sound speed in the stellar interior. These changes in principle are not small, therefore, unlike in Santos et al.

(2012), a perturbative approach may not be appropriate, and we need to use direct numerical simulations accounting for the full 3D structure of the star. Direct 3D numerical simulations also provide synthetic observations, and therefore are a powerful tool to characterize how the observable quantities change depending on the 3D stellar background.

The remainder of this work is organized as follows: in the next section we introduce the *GLobal Acoustic Spherical Simulator* (GLASS) code, which extends the code developed by Hanasoge et al. (2006) to include treatment of the center of the star. GLASS simulates linear acoustic waves propagating through the full 3D stellar interior, in the time-domain. In Sects. 3.3 and 3.4 we describe the spot model employed, analyze the effect of the spot on acoustic modes, and discuss the changes to the eigenmodes in the nonlinear regime. Section 3.5 highlights the signature of the starspot in the power spectra of the modeled light curves.

3.2 Numerical method

3.2.1 Time-domain pseudo-spectral simulations in spherical geometry

The GLASS code solves the 3D linearized hydrodynamic equations in a spherical domain containing the full star, from the center up to the stellar surface. The use of the linear approximation is justified since acoustic wave perturbations in the Sun and solar-like stars have much smaller amplitudes compared to the stellar background quantities (*e.g.*, velocity perturbations at the surface are < 20 cm/s, four orders of magnitude smaller than the local sound speed, see Libbrecht 1988). For the stellar model we considered a spherically symmetric static equilibrium described by Model S (Christensen-Dalsgaard et al. 1996) stabilized against convection (Papini et al. 2014) and including the photosphere up to $R = 1.0007 R_{\odot}$, R_{\odot} being the solar radius: that is our quiet Sun (QS) background model. We then added the starspot model to the background. We stress here that the spot model must not reintroduce convective instabilities and must fulfill the condition of hydrostatic equilibrium. We also neglected the perturbation to the gravitational potential (the so-called Cowling approximation, Cowling 1941), which reduces the order of the equations by 2. The use of the Cowling approximation is not, in general, appropriate when considering a full stellar model including the center. However, since here we are only concerned with the changes in the modes of oscillation caused by perturbations to the stellar model in the near-surface layers, we expect the Cowling approximation to be reasonable. Finally we assumed that the waves propagate adiabatically inside the star. With these assumptions, the main equations are

$$\partial_t \boldsymbol{\xi} = \mathbf{v}, \quad (3.1)$$

$$\partial_t \mathbf{v} = -\frac{\nabla p}{\rho_0} - \frac{\rho}{\rho_0} g_0 \mathbf{e}_r - \gamma(r) \mathbf{v}, \quad (3.2)$$

where $\boldsymbol{\xi}(\mathbf{r}, t)$ is the vector displacement of the wavefield, $\mathbf{v}(\mathbf{r}, t)$ is the Eulerian velocity perturbation, $g_0(r)\mathbf{e}_r$ and $\rho_0(r)$ are the unsigned (radially directed) gravitational acceleration and density of the stellar background, and \mathbf{r} and \mathbf{e}_r are the position vector and the unit vector in the radial direction. Here $\gamma(r)$ is a sponge-like damping term that prevents

spurious waves reflection at the upper boundary (Hanasoge et al. 2006). The symbols $\rho(\mathbf{r}, t)$ and $p(\mathbf{r}, t)$ are the Eulerian perturbations to density and pressure, both functions of ξ by means of the linearized continuity and adiabatic equations

$$\rho = -\nabla \cdot (\rho_0 \xi), \quad (3.3)$$

$$p = -\xi \cdot \nabla p_0 - \rho_0 (c_0^2 + \Delta c^2) \nabla \cdot \xi, \quad (3.4)$$

where Δc^2 is the change in the squared sound speed induced by the starspot, p_0 and $c_0^2 = \Gamma_0 p_0 / \rho_0$ are respectively the pressure and the square of the adiabatic sound speed of the stellar background, and Γ_0 is the first adiabatic exponent. The wavefield is excited by setting an initial condition for the displacement ξ , then the code performs the temporal integration for ξ and \mathbf{v} , while the other relevant quantities are computed at each timestep.

GLASS employs a pseudo-spectral scheme, which uses spherical harmonic (SH) decomposition on spherical surfaces to compute the horizontal derivatives, and a sixth-order tridiagonal compact scheme (Lele 1992) for radial derivatives. In SH space the spectral components are identified by the angular degree ℓ and the azimuthal order m . Temporal integration is performed by means of a five-stage second-order low dissipation and dispersion Runge-Kutta (LDDRK) scheme (Hu et al. 1996). For a more detailed description of the code see Hanasoge et al. (2006). The grid size is chosen according to the desired resolution: the maximum value ℓ_{\max} of ℓ in the SH transform sets the minimum number of latitudinal and longitudinal grid points ($n_{\text{lon}} = 2n_{\text{lat}} \geq 3\ell_{\max}$), while in the radial direction we adopted a grid with a step size constant in acoustic depth, small enough to resolve the background model and the shortest wavelength among the modes of interest. Upper boundary conditions are set by imposing a vanishing Lagrangian perturbation of the pressure

$$\delta p = p + \xi \cdot \nabla p_0 = 0 \quad \text{at } r = R,$$

which, using Equation (3.4), translates into the condition

$$\nabla \cdot \xi = 0 \quad \text{at } r = R. \quad (3.5)$$

At the center of the star we prescribe regularity conditions, as we will now explain.

3.2.2 Extending the simulation to the center of the star

Particular care must be taken when considering the center of the star. This point is a geometrical singularity in spherical coordinates, therefore, when calculating the radial derivatives for ξ_r and p , boundary conditions at the center are imposed by considering the asymptotic behavior of radial displacement and pressure in SH space. The spectral components $\xi_{r,\ell m}$ and $p_{\ell m}$ behave like $r^{\ell-1}$ and r^ℓ respectively when $r \rightarrow 0$ (see, e.g., Unno et al. (1989)). We enforce these conditions at the center by requiring that the radial derivatives of $\xi_{r,\ell m}/r^{\ell-2}$ and $p_{\ell m}/r^{\ell-1}$ vanish at the center. We then obtain the original derivatives $\partial_r \xi_{r,\ell m}$ and $\partial_r p_{\ell m}$ by means of algebraic formulas. This procedure also ensures that the numerical accuracy of the compact scheme is preserved near the center.

The horizontal spatial resolution increases with depth, owing to the clustering of the grid points, while the radial resolution remains roughly constant. As a consequence,

a numerical instability appears in those spectral components for which the horizontal wavenumber

$$k_{h,\ell} = \frac{\sqrt{\ell(\ell+1)}}{r}$$

exceeds the Nyquist wavenumber $k_{r,\max} = \pi/\Delta r$ in the radial direction, Δr being the radial grid step. We remove this instability by employing a spectral filter that, at each radial grid point r_j , sets to zero all the spectral components satisfying $k_{h,\ell}(r_j) > k_{r,\max}$. For a grid with constant Δr this translates to the condition

$$j < j_\ell = \frac{\sqrt{\ell(\ell+1)}}{\pi} \quad (+ \text{ offset}), \quad (3.6)$$

where j identifies the j -th grid point from the center. A safety offset parameter is also implemented (we found that 2 is the smallest value that removes the instability). Finally, a fourth-order tridiagonal compact low-pass filter (Lele 1992) is applied in the radial direction, to avoid spectral blocking (Hanasoge and Duvall 2007) and smooth the discontinuity in r caused by the spectral filter. The physical solutions are not affected by the filtering; radial modes (the only modes that propagate through the center of the star) are not filtered, and all the other modes are already evanescent at the points $r_j < r_{j_\ell}$ (the lower turning point for an $\ell = 1$ mode at 5 mHz is $0.03 R_\odot$, *i.e.*, the tenth gridpoint in the grid we employ, while $j_{\ell=1} = 2$). However the combined action of the filter with the time evolution scheme introduces damping in the wavefield, with an exponential dependence on frequency. This results in a lifetime of ~ 50 days for waves with frequency at 2 mHz and down to ~ 3 days at 5 mHz for the simulation setup we used, which employs a radial grid with $n_{\text{rad}} = 800$ grid points and a time step of 1 s.

3.2.3 Validation: Comparison with ADIPLS normal modes

We validated GLASS through independent calculations of the theoretical modes of oscillations for our QS model. These modes are uniquely identified by three quantum numbers: the radial order n , the angular degree ℓ , and the azimuthal order m . With the ADIPLS software package (Christensen-Dalsgaard 2008a), we computed the eigenfrequencies $\omega_{0,n\ell}$ (which are degenerate in m in the QS model) and eigenfunctions $\xi_{0,n\ell m}$ of all the acoustic modes in the range $3 < n < 37$ and up to $\ell = 2$. We then used the eigenfunctions given by ADIPLS to excite the initial wavefield displacement in GLASS. Test simulations were run in a temporal window of 10 days (solar time), using different initial conditions (by exciting either one or a few eigenmodes at the same time) and grid sizes. We also performed one simulation with all the modes excited and in a temporal window of 70 days, to use as reference for our study. Figure 3.1 shows the logarithmic plot of the power spectrum of the reference QS simulation. The effect of numerical damping is evident.

In all the tests performed, the extracted eigenfrequencies and eigenfunctions were compared with ADIPLS solutions and showed good agreement: the difference between ADIPLS and GLASS for the eigenfrequencies was below $0.16 \mu\text{Hz}$ (*i.e.*, the frequency resolution of the simulations) and the maximum difference for the eigenfunctions was $\sim 0.1\%$, after the damping was accounted for (see Figure 3.2).

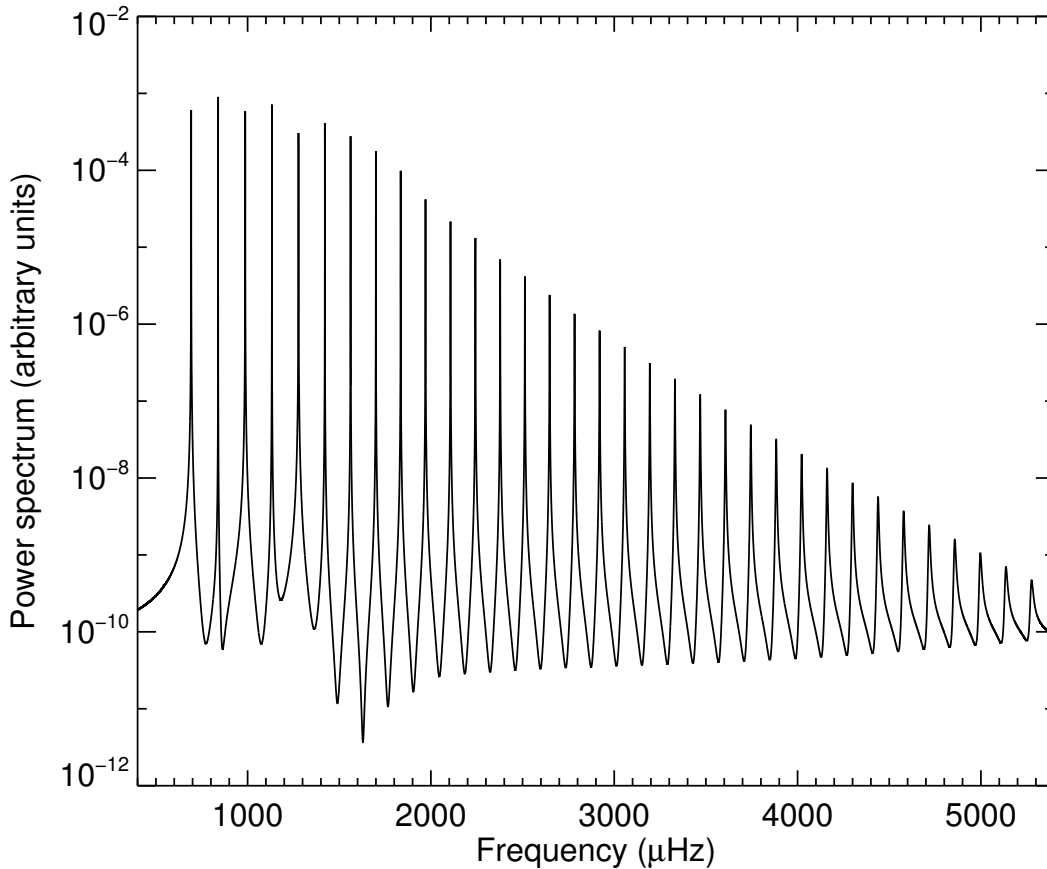


Figure 3.1: Power spectrum of the reference QS simulation (logarithmic scale) as calculated by using the procedure described in Section 3.5, from a light curve with a length of 70 days and a cadence of 60 seconds.

3.3 Frequency shifts: Nonlinear dependence on perturbation amplitude

3.3.1 Spot model: Perturbation in sound speed

We modeled the changes to the stratification caused by a starspot as a positive change Δc^2 in the squared sound speed, while the density and pressure were unchanged. This guaranteed the compatibility with the stabilization method used for the background model (for which a decrease in the sound speed would reintroduce convective instabilities). We defined the change in the sound speed as

$$\Delta c^2(r, \theta) = \epsilon c_0^2(r) f(r; r_c) g(\theta), \quad (3.7)$$

with positive amplitude ϵ , a radial profile

$$f(r; r_c) = \frac{1}{2} \left[\cos \left(\frac{|r - r_c|}{\sigma} \right) + 1 \right] \exp \left[-\frac{(r - r_c)^2}{2\sigma^2} \right] \quad (3.8)$$

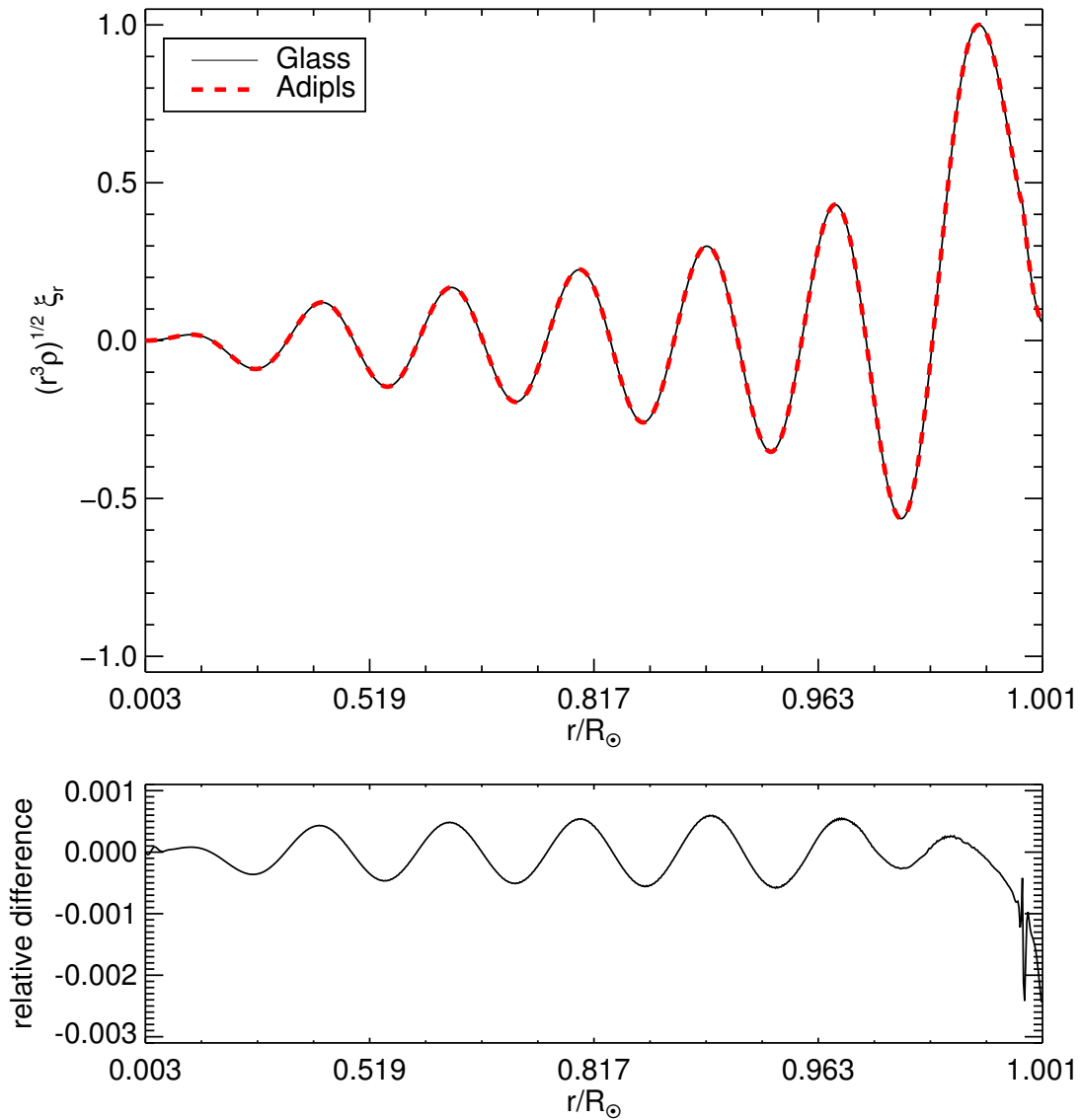


Figure 3.2: Radial displacement eigenfunction $(r^3\rho)^{1/2}\xi_r(r, \theta)$ of QS model from GLASS (black solid line) and from ADIPLS (dashed thick red line), for the $\ell = 2, n = 12$ mode. Each eigenfunction is normalized to its maximum. The bottom panel plot the difference between the two functions. The x-axis is rescaled with respect to the acoustic depth.

for $|r - r_c| < \pi\sigma$ and zero otherwise, and with a latitudinal profile

$$g(\theta) = \frac{1}{2} [\cos(\kappa\theta) + 1] \quad (3.9)$$

for $\kappa\theta < \pi$ and zero otherwise, where θ is the colatitude. The functions f and g have continuous derivatives everywhere and define a spot located at the north pole, with a Gaussian profile in radius multiplied by a raised cosine and a raised cosine profile in latitude. For the study the vertical and horizontal size of the spot were fixed by setting $\sigma = 0.01 R_\odot$ and $\kappa = 2.4$, and we varied the depth $R_\odot - r_c$ and the amplitude ϵ . Figure 3.3 shows the a plot of f and g for $r_c = 0.98 R_\odot$. We note that the choice of the coordinate system here is completely arbitrary, since we are studying the perturbation to a spherically symmetric (*e.g.*, nonrotating) background, therefore the results of this work can be translated to a spot located at any point at the surface, via a rotation of the coordinate system.

3.3.2 Linear theory

We first discuss the effect of small perturbations, in order to determine for which parameter range the frequency shifts falls in the linear regime. We consider the normal mode solutions $\xi_0(\mathbf{r}, t) = \xi_{0,n\ell m}(\mathbf{r})e^{-i\omega_{0,n\ell}t}$ of our reference QS model, solving the wave equation

$$\rho_0\omega_{0,n\ell}^2\xi_0 = -\nabla(c_0^2\rho_0\nabla\cdot\xi_0) - \nabla(\xi_0\cdot\nabla p_0) + g_0\mathbf{e}_r\nabla\cdot(\rho_0\xi_0) = \mathcal{H}\xi_0 \quad (3.10)$$

that can be derived from Equations (3.1-3.4). Since the reference background is spherically symmetric, the solutions are degenerate in m . We consider now the perturbation $\Delta\mathcal{H}$ to the wave operator \mathcal{H} due to a generic change in the sound speed (while retaining pressure and density constant), given by

$$\Delta\mathcal{H}\xi_0 = -\nabla(\Delta c^2\rho_0\nabla\cdot\xi_0); \quad (3.11)$$

the expression for the linear frequency shift (see, *e.g.*, Aerts et al. 2010) is

$$\frac{\Delta\omega_{n\ell m}}{\omega_{0,n\ell}} = \frac{\int_{\odot} \Delta c^2(\nabla\cdot\xi_0^*)(\nabla\cdot\xi_0)\rho_0 dV}{2\omega_{0,n\ell}^2 \int_{\odot} \|\xi_0\|^2\rho_0 dV}, \quad (3.12)$$

where integration is performed over the entire volume of the star. Both the surface integral and the perturbation to the mode inertia do not contribute to the change in $\Delta\omega_{n\ell m}$ in this case: the surface integral is zero because of the surface boundary conditions imposed for the pressure, and there is no contribution from the perturbation to the mode inertia, since the density of the background is unchanged. Finally, by exploiting the separable form of the polar spot profile (3.7), we may write the frequency shift in terms of a product of separate integrals for the horizontal and radial coordinates. It is worth noting that, unlike the case of splitting induced by rotation, the frequency shift depends only on $|m|$ and therefore modes with the same $|m|$ are still degenerate. This holds true also in the nonlinear case.

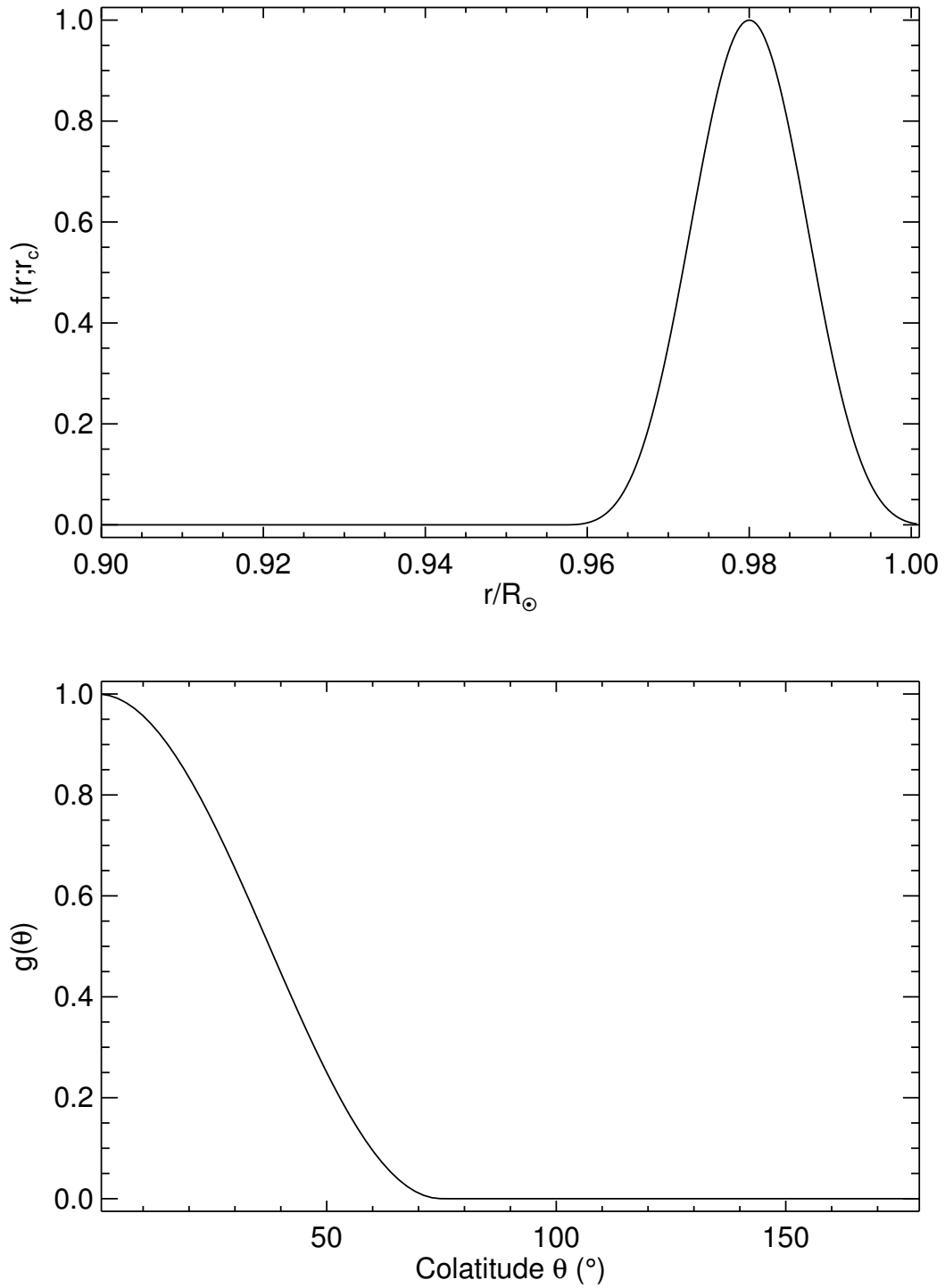


Figure 3.3: Top: spot radial profile $f(r; r_c)$ defined by Equation (3.8) for $r_c = 0.98 R_\odot$ and $\sigma = 0.01$. Bottom: spot latitudinal profile $g(\theta)$ defined by Equation (3.9), with $\kappa = 2.4$.

3.3.3 Numerical simulations

3.3.3.1 Initial conditions: δ -function source

We performed our study in the parameter range $0.01 \leq \epsilon \leq 1$ and $0.97 R_\odot \leq r_c \leq 1 R_\odot$. The simulations run for 70 days (solar time) to reach the desired accuracy of $\sim 0.16 \mu\text{Hz}$ in the frequency domain. Wavefield displacement and velocity records were taken with a cadence of 60 seconds (solar time), mimicking the usual cadence of helio- and asteroseismic observations and in order to have a Nyquist frequency of $\sim 8.3 \text{ mHz}$ (above the maximum acoustic cutoff frequency of $\sim 5.3 \text{ mHz}$). Starting from the ADIPLS eigenfunctions, we set the initial conditions for the wavefield displacement as

$$\boldsymbol{\xi}(\mathbf{r}, t = 0) = \sum_{n=3}^{37} \sum_{\ell=0}^2 \sum_{m=-\ell}^{\ell} \boldsymbol{\xi}_{0,n\ell m}(\mathbf{r}), \quad (3.13)$$

which excites all the modes from $3 < n < 37$ and up to $\ell = 2$. The initial velocity \mathbf{v} is set to zero. We note here that all the modes were excited with the same phase.

3.3.3.2 Nonlinear frequency shifts

The simulated frequencies have been extracted by taking the SH transform coefficient $p_{\ell m}(r_0, t)$ of the wavefield pressure $p(r_0, \theta, \phi, t)$ at each timestep and at $r_0 = R_\odot + 200 \text{ km}$ above the surface. This was followed by a Fourier transform in time to obtain the field $\tilde{p}_{\ell m}(r_0, \omega)$ and then the power spectrum $P_{\ell m}(\omega) = |\tilde{p}_{\ell m}(r_0, \omega)|^2$. Finally we divided each (ℓ, m) spectrum in chunks with size of $80 \mu\text{Hz}$ and centered on the peak closest to the original ADIPLS mode frequency. A least-squares Lorentzian fit was applied to extract frequency, amplitude, and half width at half maximum (HWHM) of each mode.

Figures 3.4, 3.5 and 3.8 show selected results obtained for the frequency shifts $\Delta\nu = \Delta\omega/2\pi$ induced by the spot with respect to QS in the case of a polar spot located at $r_c = 0.98 R_\odot$ (in the following we will always show plots related to simulations performed for this value of r_c). Figure 3.4 shows the relative frequency shifts $\Delta\nu/\nu$ as a function of mode frequency $\nu = \omega/2\pi$ for all the modes we excited, extracted from a simulation with a spot of amplitude $\epsilon = 0.4$. The linear frequency shifts calculated from Equation (3.12) reproduce the behavior of nonaxisymmetric modes ($m \neq 0$). However for axisymmetric modes the frequency shifts deviate from the theoretical linear shifts, but with a different behavior depending on ℓ , the most interesting being the case $\ell = 2$ (bottom panel). Here the relative frequency shifts for $m = 0$ modes are smaller than predicted, and even decrease with increasing mode frequency, while $\Delta\nu/\nu$ remains roughly constant for the $|m| = 1$ and 2 modes. As a consequence, at a frequency of $\sim 3000 \mu\text{Hz}$ the $\Delta\nu/\nu$ for $m = 0$ modes cross the relative frequency shifts of the $m = 1$ modes. Above this crossing frequency the $m = 1$ modes have the largest frequency shifts. Results from the other simulations performed (see Figures 3.5-3.7) shown that this crossing frequency decreases either when the amplitude ϵ increases (as seen also in Fig. 3.8) or when r_c is moved toward the surface, the latter indicating a stronger nonlinear response of the system to smaller surface changes than to bigger changes buried deeper in the convection zone.

Figure 3.8 shows the simulated frequency shifts $\Delta\nu$ against spot amplitudes ϵ and for all the modes with $\ell = 2, n = 12$. These modes in the reference QS model are degenerate

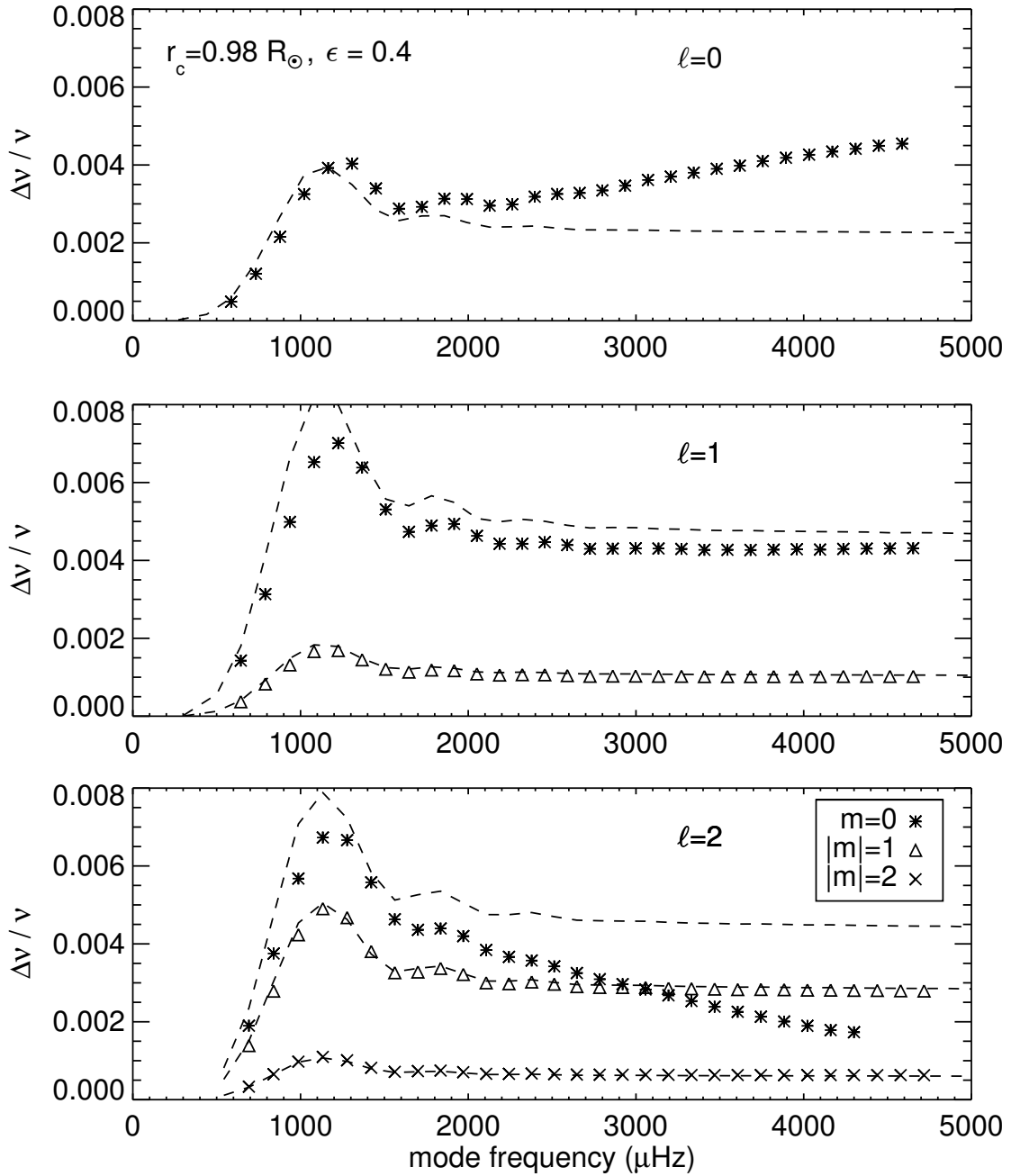


Figure 3.4: Relative frequency shifts $\Delta\nu/\nu$ vs. mode frequency ν for modes with $\ell = 0$ (upper panel), $\ell = 1$ (middle panel) and $\ell = 2$ (bottom panel), for a polar spot model relative to QS model with $r_c = 0.98 R_\odot$ and $\epsilon = 0.4$. Dashed lines represent linear frequency shifts given by Equation (3.12). Fitted frequencies from numerical simulations (asterisks for $m = 0$, triangles for $|m| = 1$, and crosses for $|m| = 2$) show the nonlinear behavior of the shifts for $m = 0$ modes (asterisks). We note that $m = 0$ and $|m| = 1$ mode frequencies for $\ell = 2$ cross at $\nu \simeq 3060 \mu\text{Hz}$.

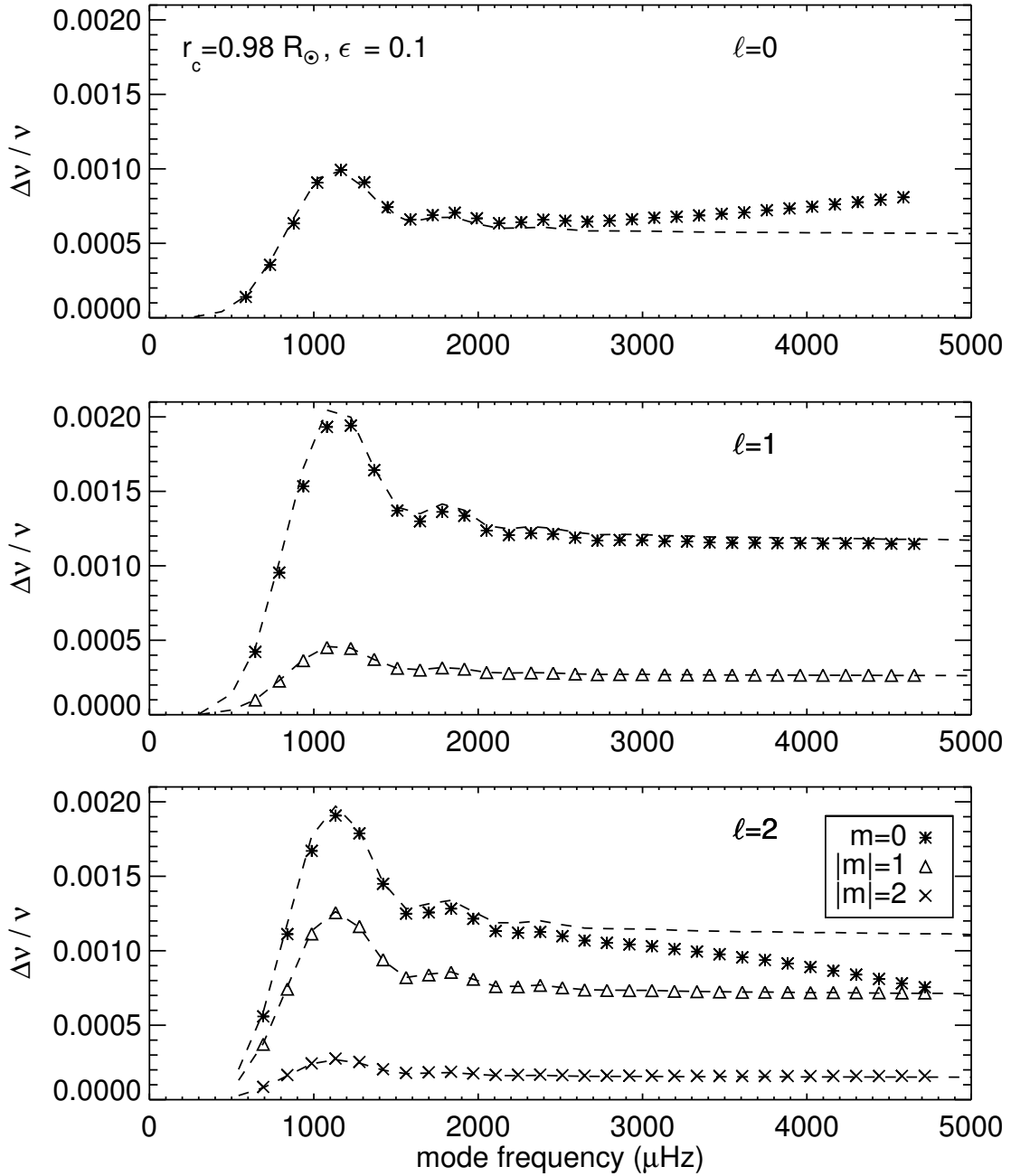


Figure 3.5: Same as Figure 3.4, but for $\epsilon = 0.1$ and $r_c = 0.98 R_\odot$. We note that in this case $m = 0$ and $|m| = 1$ mode frequencies for $\ell = 2$ cross at $\nu \approx 4900 \mu\text{Hz}$.

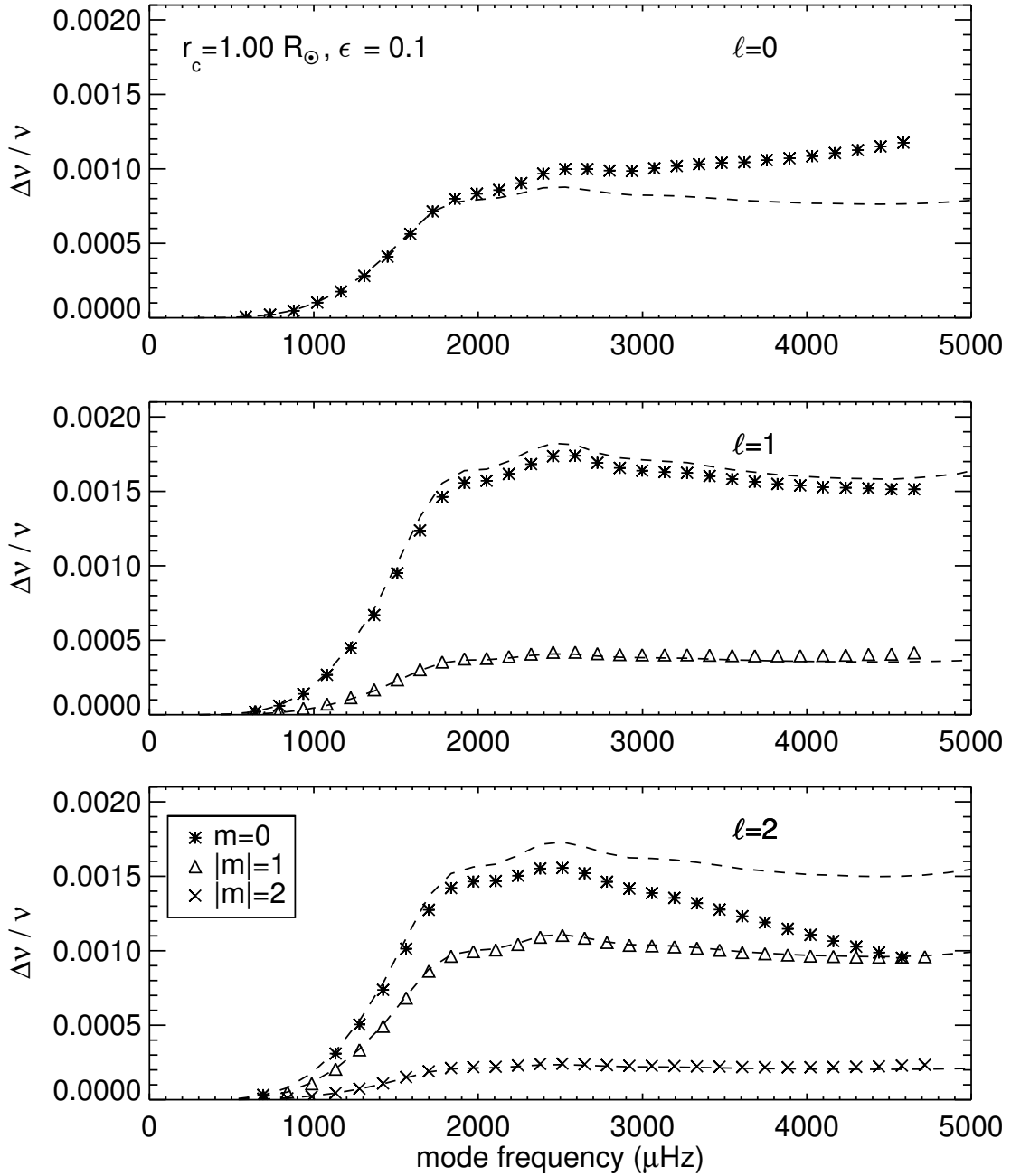


Figure 3.6: Same as Figure 3.4, but for $\epsilon = 0.1$ and $r_c = 1.00 R_\odot$. We note that in this case $m = 0$ and $|m| = 1$ mode frequencies for $\ell = 2$ cross at $\nu \simeq 4600 \mu\text{Hz}$.

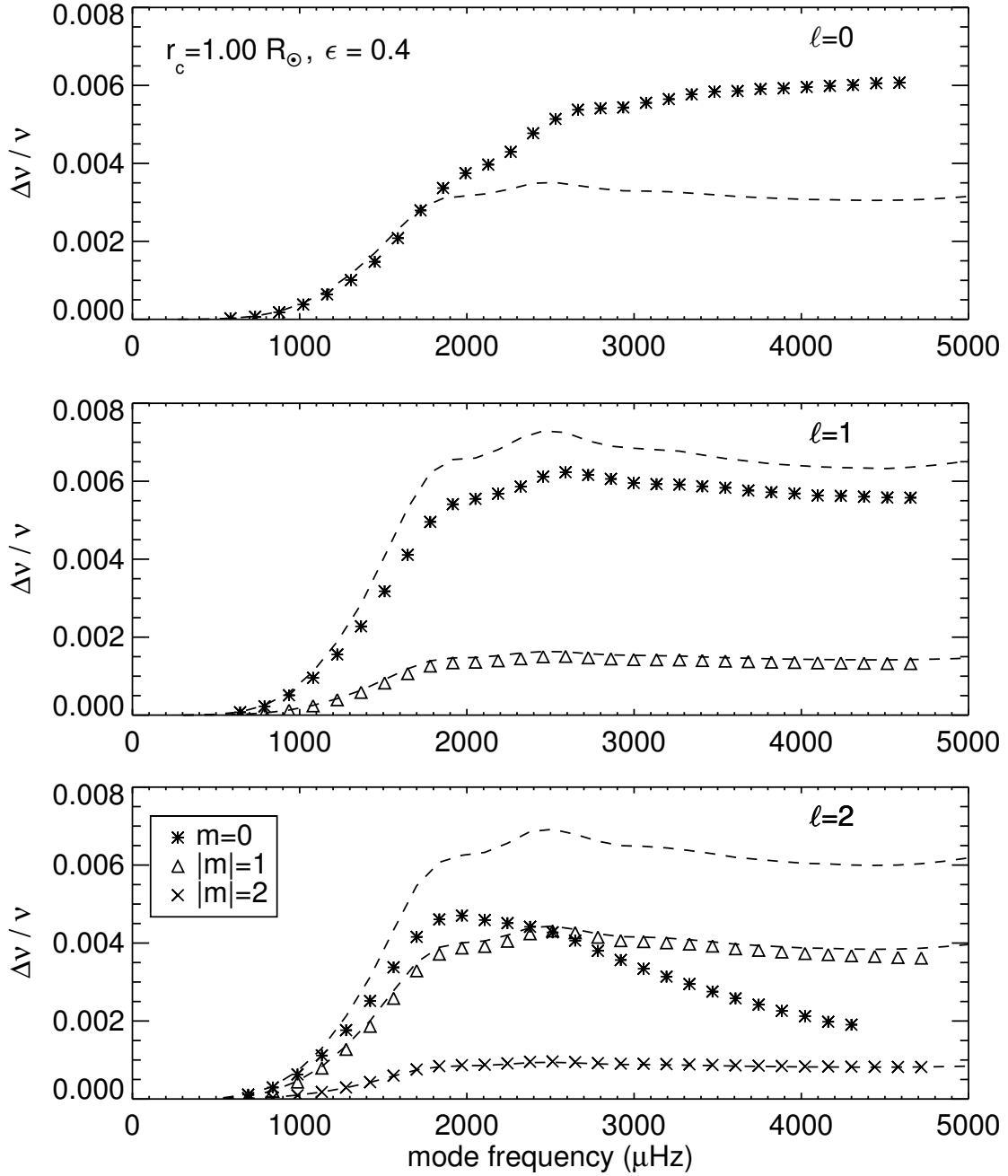


Figure 3.7: Same as Figure 3.4, but for $\epsilon = 0.4$ and $r_c = 1 R_\odot$. We note that in this case $m = 0$ and $|m| = 1$ mode frequencies for $\ell = 2$ cross at $\nu \simeq 2500 \mu\text{Hz}$.

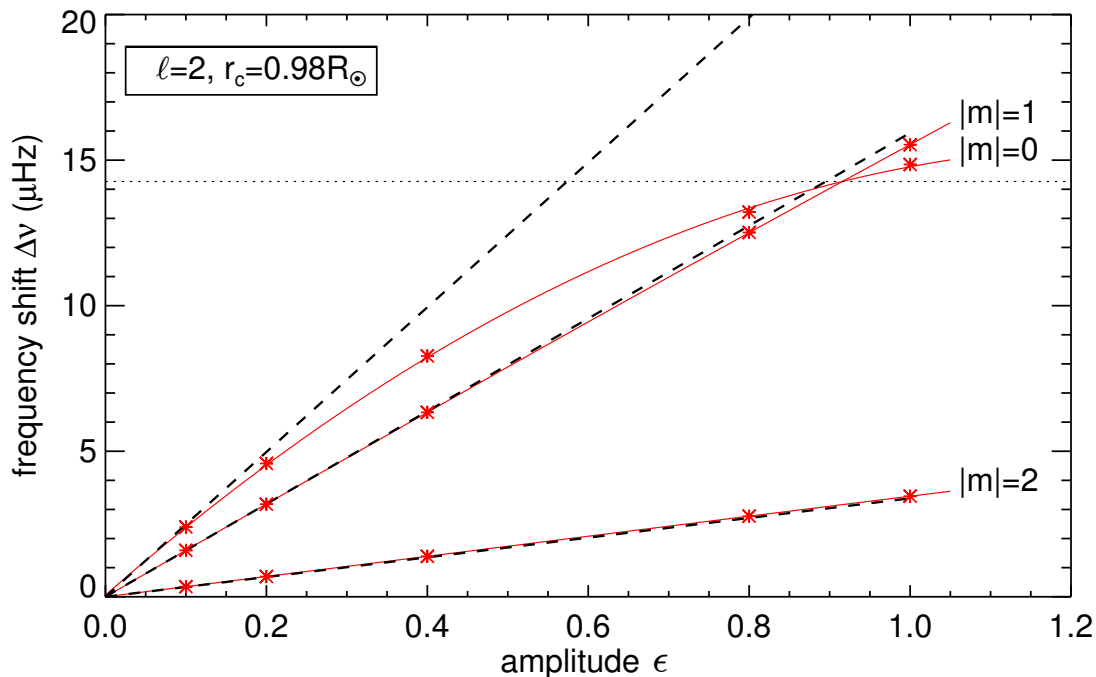


Figure 3.8: Mode frequency shifts $\Delta\nu$ vs. spot amplitude ϵ for modes with $\ell = 2$, $n = 12$ and $|m| = 0, 1, 2$ in the case of a polar spot model with $r_c = 0.98$. The QS eigenfrequency for these modes is $\nu_0 = 1970.50 \pm 0.16 \mu\text{Hz}$. Dashed lines represent linear frequency shifts given by Equation (3.12), red asterisks are frequencies shifts from numerical simulations. Solid red lines represent parabolic fits to the shifts. The horizontal dotted line shows the crossing of the frequencies between the $m = 0$ and $|m| = 1$ modes at $\epsilon \simeq 0.92$.

with respect to the azimuthal order m , with a frequency $\nu_0 = 1970.50 \pm 0.16 \mu\text{Hz}$. Again linear theory successfully reproduces the frequency shift for nonaxisymmetric modes, shifts for $|m| = 1$ however start to deviate from linear behavior at $\epsilon \simeq 0.8$. The frequency shifts for $m = 0$ modes on the contrary are nonlinear already at ϵ values of ~ 0.2 , with $\Delta\nu$ values smaller than predicted by linear theory. A parabolic fit is able to model the shift, thus indicating that in this case a second order perturbative correction could recover the actual frequencies. The figure shows also the crossing frequency (horizontal dotted line) matching the mode frequency at $\epsilon \simeq 0.92$, with a value of about $1985 \mu\text{Hz}$ (corresponding to a frequency shift $\Delta\nu \simeq 14.5 \mu\text{Hz}$), decreased by $\sim 1000 \mu\text{Hz}$ with respect to the case with $\epsilon = 0.4$, as already noted above.

3.4 Perturbations to the eigenfunctions

The polar spot introduces a nonspherically-symmetric perturbation to the background model. As a consequence the eigenfunctions depart from their original horizontal dependence and get mixed with other spherical harmonics. The extent of the mixing depends on the amplitude of the perturbation. Because of the axisymmetric profile of the spot there is no mixing between spherical harmonics with different m . We investigate the effect of the mixing in the eigenfunctions by writing the radial displacement eigenfunction of a given

mode for the model with the spot as

$$\xi_r^{n\tilde{\ell}m}(\mathbf{r}, t) = e^{-i\omega_{n\tilde{\ell}m}t} \sum_{\ell=0}^{\ell_{\max}} a_{\ell}^{n\tilde{\ell}m}(r) Y_{\ell}^m(\theta, \phi) = \xi_r^{n\tilde{\ell}m}(r, \theta) e^{im\phi} e^{-i\omega_{n\tilde{\ell}m}t} \quad (3.14)$$

with the spherical harmonics Y_{ℓ}^m given by

$$Y_{\ell}^m(\theta, \phi) = \sqrt{\frac{(2\ell+1)(\ell-m)!}{4\pi(\ell+m)!}} P_{\ell}^m(\cos\theta) e^{im\phi},$$

where ℓ_{\max} gives the spectral resolution of the SH transform and where we labeled with $\tilde{\ell}$ the new mixed eigenmode originally represented by a pure $Y_{\tilde{\ell}}^m$ in the QS model. Here $\xi_r^{n\tilde{\ell}m}(r, \theta)$ is the meridional profile of $\xi_r^{n\tilde{\ell}m}$, expressed through a truncated series of Legendre polynomials (*i.e.*, the latitudinal components of the Y_{ℓ}^m)

$$\xi_r^{n\tilde{\ell}m}(r, \theta) = \sum_{\ell=0}^{\ell_{\max}} a_{\ell}^{n\tilde{\ell}m}(r) \sqrt{\frac{(2\ell+1)(\ell-m)!}{4\pi(\ell+m)!}} P_{\ell}^m(\cos\theta). \quad (3.15)$$

The amplitude coefficients $a_{\ell}^{n\tilde{\ell}m}(r)$ with $\ell \neq \tilde{\ell}$ give the degree of mixing with $Y_{\tilde{\ell}}^m$ of the $n\tilde{\ell}m$ mode at the radial position r .

Figure 3.9 shows radial cuts taken at different colatitudes θ (*i.e.*, at different angular distances from the center of the spot) of the scaled radial displacement eigenfunction $(r^3\rho)^{1/2}\xi_r^{n\tilde{\ell}m}(r, \theta)$, for a $\tilde{\ell} = 2, m = 0, n = 12$ (top panel) and for a radial mode with $n = 16$ (bottom panel), for a spot with $\epsilon = 0.4$ and $r_c = 0.98 R_{\odot}$. Each cut has been renormalized to its maximum. In the case of the quadrupolar mode the phase shift of ξ_r inside the spot with respect to the QS solution increases from the center, and reaches its maximum at the edge of the spot (*i.e.*, for $\theta = 60^\circ$). The shift then decreases, and $\hat{\xi}_r$ smoothly matches the QS eigenfunction at $\theta = 90^\circ$.

The phase shift has a different behavior in the case of the radial mode with $n = 16$, it is maximum at the center of the spot and then approaches zero at the antipodes ($\theta = 180^\circ$). This is in agreement with what was found by Santos et al. (2012), except that in our case the radial profile of the eigenfunction does not match the QS eigenfunction at the spot edge.

3.5 Synthetic power spectra for a polar spot

3.5.1 Synthetic light curves

Mode mixing affects observed light curves, as was already pointed out by Dziembowski and Goode (1996) and Cunha and Gough (2000) in the case of RoAp stars, since it changes the expected mode visibilities. The production of a realistic synthetic light curve is a nontrivial task, which requires modeling all the contributions to the emergent intensity at the photosphere in the observed wavelength range. Here we only model the contribution of the photospheric pressure perturbations to the intensity fluctuations I induced by the acoustic wavefield. This in principle requires an explicit relation between the mode

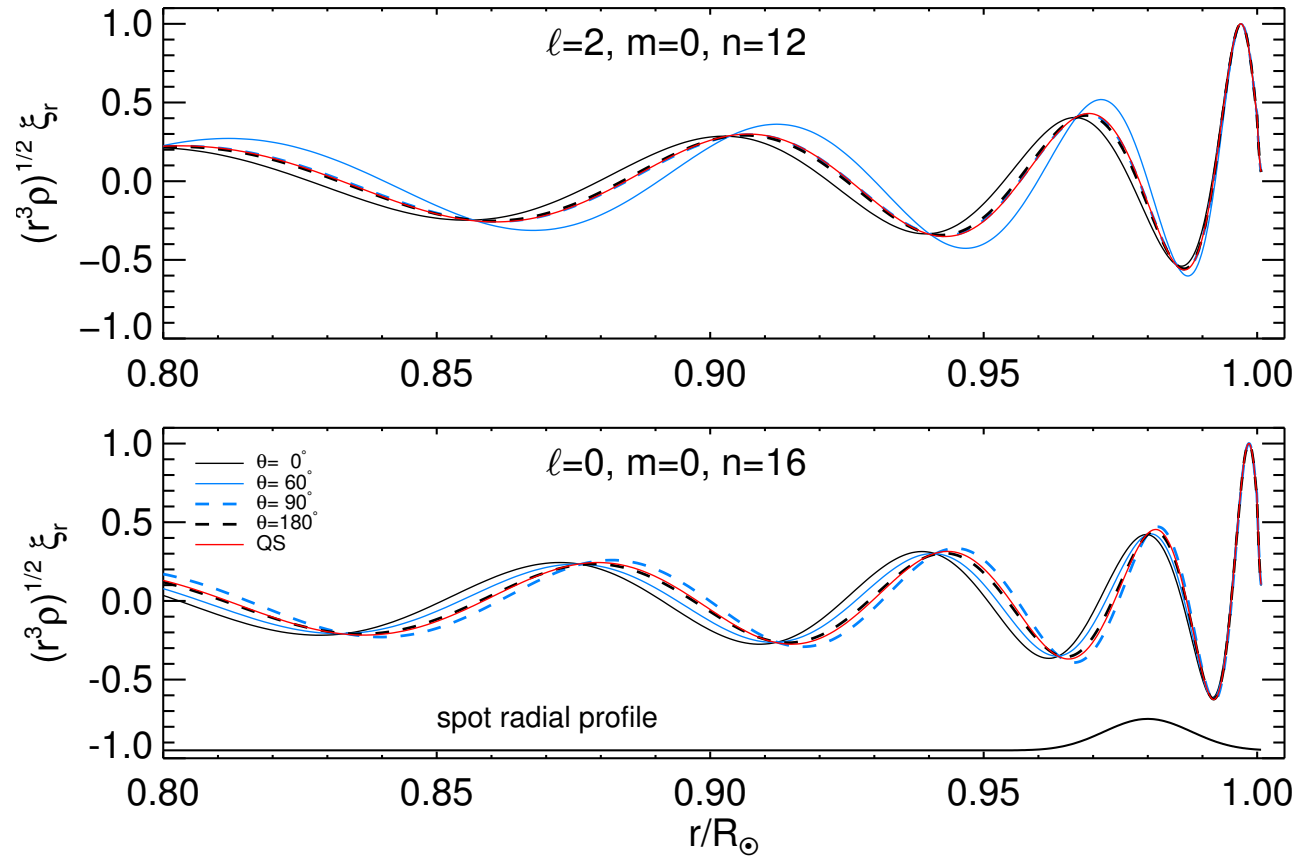


Figure 3.9: Normalized cuts at different colatitudes θ of the radial displacement eigenfunction $(r^3 \rho)^{1/2} \xi_r(r, \theta)$ at the center of the spot ($\theta = 0$, solid black line), at the edge ($\theta = 60^\circ$, solid blue line), and outside the spot (dashed lines), of the $\tilde{\ell} = 2, m = 0, n = 12$ mode (top) and $\tilde{\ell} = 0, m = 0, n = 16$ mode (bottom), for a polar spot with $r_c = 0.98 R_\odot$ and $\epsilon = 0.4$. The solid red line is the corresponding ξ_r from ADIPLS. The solid black line in the bottom panel beneath the eigenfunctions shows the radial profile f of the spot. The blue and black dashed lines in the top panel completely overlap.

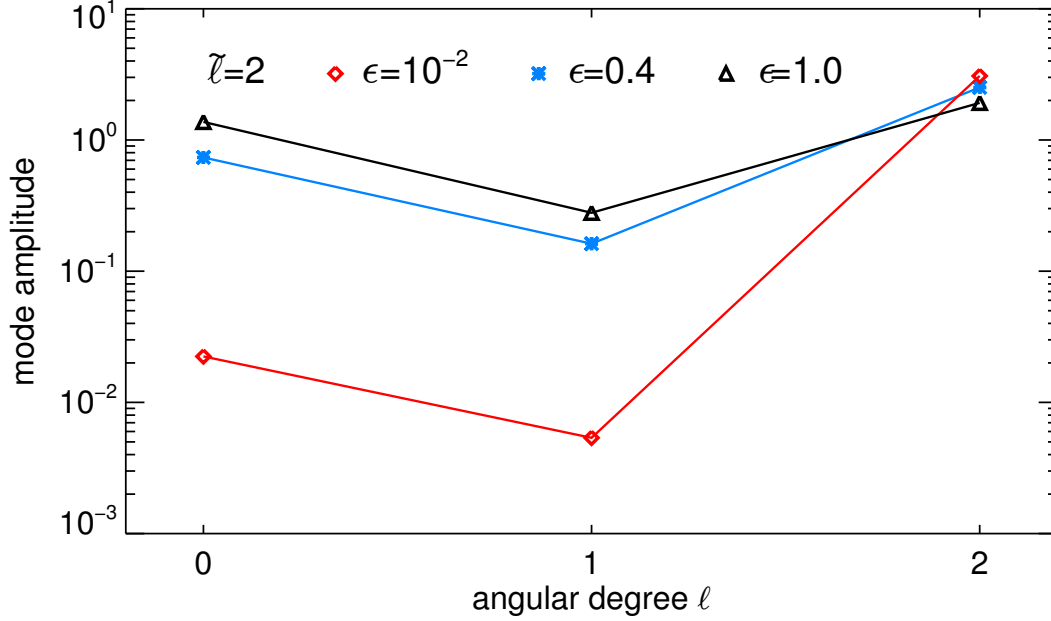


Figure 3.10: Amplitude coefficients $|\tilde{p}_{\ell m}(r_0, \omega_{n\tilde{\ell}m})|$ of equation (3.17) showing the mixing of the $\tilde{\ell} = 2, n = 12, m = 0$ mode for three simulations with spot amplitude $\epsilon = 0.01$ (red squares), 0.4 (blue asterisks), and 1.0 (black triangles).

displacement and $I(\theta', \phi', t)$ at the stellar surface, which is rather complicated in general (see Toutain and Gouttebroze 1993).

For the sake of simplicity we assume that $I(\theta, \phi, t)$ is proportional to the Eulerian pressure perturbation $p(r_0, \theta, \phi, t)$ measured at $r_0 = R_\odot + 200$ km. We then express I in the frequency domain as

$$\tilde{I}(\theta, \phi, \omega) \propto \tilde{p}(r_0, \theta, \phi, \omega) = \sum_{\ell=0}^{\ell_{\max}} \sum_{m=-\ell}^{\ell} \tilde{p}_{\ell m}(r_0, \omega) Y_\ell^m(\theta, \phi), \quad (3.16)$$

where $p_{\ell m}$ are the SH coefficients of the pressure, obtained as described in Section 3.3.3 and containing all the contributions to the wavefield in the spectral component (ℓ, m) , including the mixing from other $\ell \neq \tilde{\ell}$ modes. We can explicitly quantify the mixing of a single mode by writing (see also Equation (3.14))

$$\tilde{p}(r_0, \theta, \phi, \omega_{n\tilde{\ell}m}) = \sum_{\ell=0}^{\ell_{\max}} \tilde{p}_{\ell m}(r_0, \omega_{n\tilde{\ell}m}) Y_\ell^m(\theta, \phi), \quad (3.17)$$

where $\omega_{n\tilde{\ell}m}$ is the mode frequency in the presence of the spot. The values of $\tilde{p}_{\ell m}(r_0, \omega_{n\tilde{\ell}m})$ with $\ell \neq \tilde{\ell}$ give the degree of the mixing.

Figure 3.10 shows the coefficients $|\tilde{p}_{\ell m}(r_0, \omega_{n\tilde{\ell}m})|$ of expansion (3.17) for the $n = 12, \tilde{\ell} = 2, m = 0$ mode for three different values of ϵ . Mixing in the $\epsilon = 0.01$ case is almost absent. For $\epsilon = 0.4$ the mixing contribution from the dipole component is negligible (one order of magnitude smaller), while that from the radial component is 30% of the leading mode. The mixing increases significantly for $\epsilon = 1$, reaching 15% for $\ell = 1$ and 72% for $\ell = 0$, thus resulting in extreme distortion of the eigenfunctions for that mode.

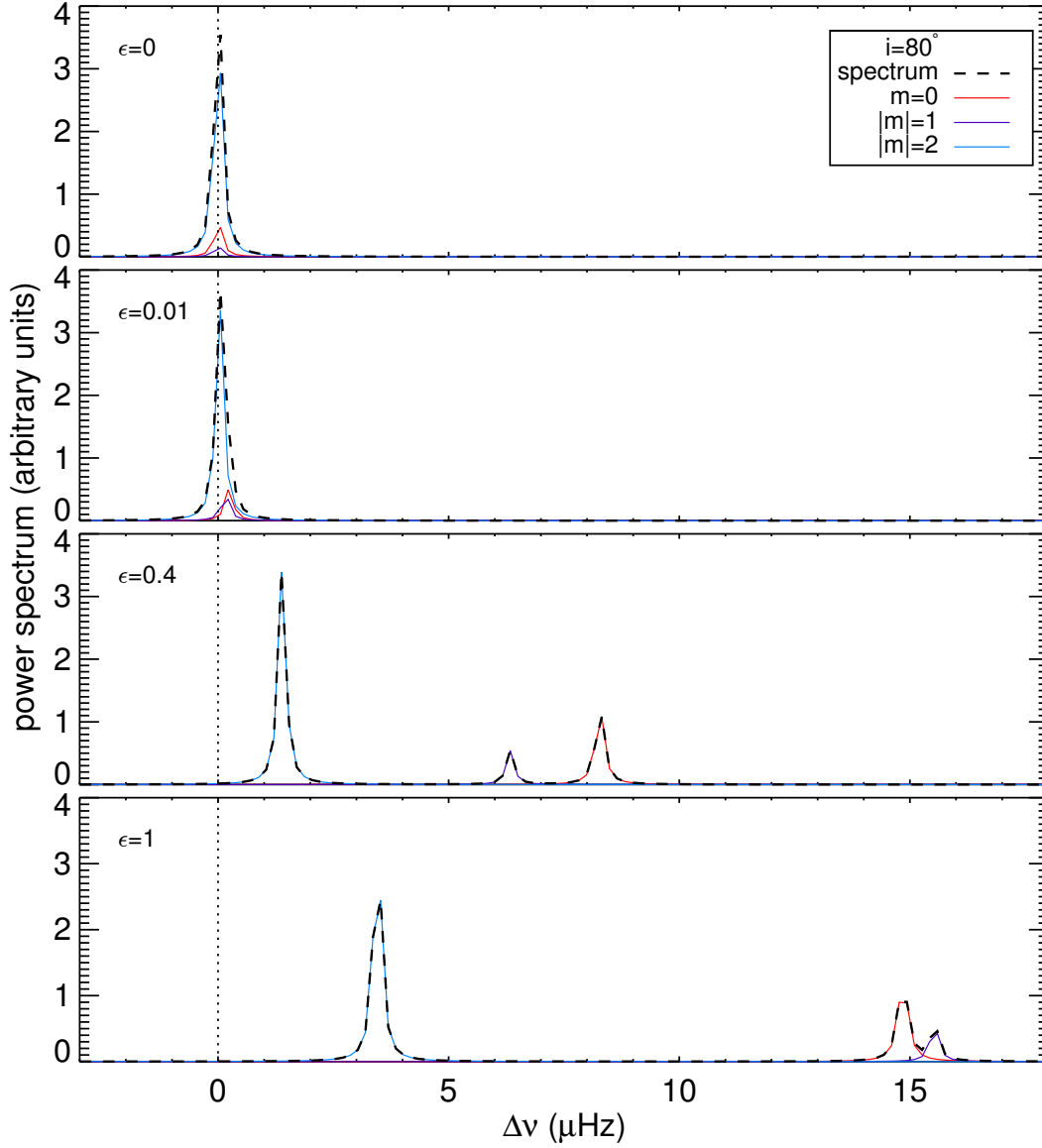


Figure 3.11: Acoustic power vs. $\Delta\nu$ for $\tilde{\ell} = 2$, $n = 12$ and $m = 0$ (red), ± 1 (violet), and ± 2 (blue) at an inclination angle $i = 80^\circ$, for QS ($\epsilon = 0$, upper panel) and for a spot located at a depth of $0.98 R_\odot$ and with $\epsilon = 0.01$ (second upper panel), 0.4 (third upper panel), and 1.0 (bottom panel). The black dashed lines represent the spectra resulting from the sum of all the m components. Because of the initial conditions in Equation (3.13), the observed acoustic power in the $|m| > 0$ modes is twice the power that would be observed in the case of stochastic excitation.

3.5.2 Example power spectrum for $\ell = 2$

As an example we consider now four synthetic power spectra $P(\omega)$ of a star with an inclination angle i of the polar axis with respect to the line of sight of 80° , for QS and three different amplitudes with ϵ values of 0.01, 0.4, and 1, respectively. To create the spectra we followed the procedure outlined by Gizon and Solanki (2003): starting from the intensity fluctuations approximated by Equation (3.16), we calculated the disk integrated intensity $\tilde{I}(\omega)$ in the frequency domain, accounting for projection and limb-darkening effects (Pierce 2000). The resulting power spectra $P(\omega) = |\tilde{I}(\omega)|^2$ vs. $\Delta\nu$ are shown in Fig. 3.11 for the $\tilde{\ell} = 2, n = 12$ multiplet. We note that because of the initial conditions we set (*i.e.*, the choice made in Equation (3.13) of using the same phase in exciting all of the modes), the $|m| > 0$ peaks in these spectra are twice as high as the peaks in a spectrum of acoustic oscillations resulting from stochastic excitation (that is the case for Sun-like stars). The $\epsilon = 0.01$ case falls in the linear regime: the visibility of the modes is the same as that of pure spherical harmonics (observed amplitude ratios correspond to Fig. 2 of Gizon and Solanki (2003), once the residual degeneracy in the $m \neq 0$ modes and the choice of the phase in the initial conditions (3.13) are taken into account) with very little mixing, as already shown in Fig. 3.10.

The same holds true in the case of $\epsilon = 0.4$ and 1 for nonaxisymmetric modes (the differences in shape and height between the peaks in the plots occur because the bin size is comparable to the HWHM of the peaks for these modes). The $m = 0$ mode, on the contrary, departs from the linear regime both in frequency shift (which for $\epsilon = 1$ becomes even smaller than that one for $|m| = 1$) and observed amplitude, as a consequence of the mixing with other spherical harmonics.

4 On the asteroseismic signature of a large active region

This work was done in collaboration with L. Gizon, who presented preliminary work about the linear theory (Gizon 1995, 1998). The core of Section 4.2 is based on Gizon (1995). I expanded this work to include the effect of centrifugal distortion. I ran the numerical simulations of Section 4.3. This work is supported by SFB 963 “Astrophysical Turbulence and Flow Instabilities” (Project A18).

Chapter summary

Stellar acoustic oscillations are influenced by magnetic activity, however it is unclear how localized magnetic features, such as active regions, contribute to these changes. Also rotation plays a role, further complicating the structure of the observed acoustic power spectra. Here we aim to characterize the seismic signature in the acoustic wavefield of a large active region in a highly active star and in presence of rotation. We used linear perturbation theory to analyze the combined effect on global acoustic oscillations of a 3D perturbation to the spherically symmetric solar Model S and in presence of differential rotation. For the active region we used a simplified model, which accounts for strength ε and surface coverage of the perturbation. We also explored the nonlinear regime by means of numerical simulations with the GLASS code. The combined effect of the 3D perturbation and of rotation on a $\ell = 2, n = 18$ multiplet generates 25 peaks, with 20 peaks clustered near the pure rotational frequencies. As result the observed power spectrum of the multiplet departs from its pure rotational shape and develops an asymmetric profile. Only up to 6 Lorentzian profiles are visible because of the blending peaks. The inclination angle of observation and the latitudinal position of the active region strongly affect the asymmetric shape of the observed spectrum, thus making possible to infer the latitudinal position of the active region. Even if already present at perturbation amplitudes of $\varepsilon = 0.005$, the nonlinear changes in frequency and amplitude of the peaks in the power spectrum are almost covered by blending. The nonlinear behavior becomes visible in the spectrum only in the strongly nonlinear regime.

4.1 Introduction

In this chapter we ask whether it is possible to detect the asteroseismic signal of a localized surface perturbation, such as an active region. We focused on stars with a level of activity higher than the Sun: those stars may have active regions with high surface coverage, and therefore better chances for detection.

Following the same approach of Goode and Thompson (1992) we used linear perturbation theory to calculate the changes induced in a $\ell = 2$ multiplet by a modeled active region (AR) and in presence of rotation. It is important to include the effect of rotation, to correctly reproduce the seismic signal resulting from the combined effect of rotation and the AR perturbation: in a spherically symmetric star multiplets are $(2\ell + 1)$ -fold degenerate in the azimuthal order m . Rotation completely removes the degeneracy by splitting the frequencies. However if a second unsteady perturbation is present, then each multiplet in the observed power spectrum would appear to have more than $(2\ell + 1)$ peaks.

Since the complex influence of an active region on acoustic oscillations is poorly understood, we considered a simple two parameters model, accounting for surface coverage and perturbation amplitude of the AR. We also discussed the changes that would be observed in the theoretical power spectra. As a complement to the linear analysis we also explored the nonlinear regime of the AR perturbation by means of 3D numerical simulations, using the GLASS code (see Papini et al. 2015, reproduced in this manuscript as Chapter 3).

4.2 Signature of an active region in the acoustic power: linear theory

4.2.1 Linear problem in the corotating frame

The normal modes of oscillation of a spherically symmetric nonrotating star are uniquely identified by three integer numbers: the radial order n , the angular degree ℓ , and the azimuthal order m , with $|m| \leq \ell$. Each eigenmode is described by a displacement vector $\xi_{n\ell m}^0(\mathbf{r}, t) = \xi_{n\ell m}^0(\mathbf{r})e^{-i\omega_{0,n\ell}t}$ that satisfies the linearized equation of motion

$$\mathcal{H}\xi_{n\ell m}^0(\mathbf{r}) = \omega_{0,n\ell}^2 \xi_{n\ell m}^0(\mathbf{r}), \quad (4.1)$$

where \mathcal{H}_0 is a linear spatial operator associated to the spherically symmetric star (see, *e.g.*, Unno et al. 1989). In spherical polar coordinates the eigenfunctions $\xi_{n\ell m}^0(\mathbf{r})$ are expressed in a separable form in term of the normalized spherical harmonics $Y_\ell^m(\theta, \phi)$, as

$$\xi_{n\ell m}^0(r, \theta, \phi) = \left[\xi_{r,n\ell}^0(r)\mathbf{e}_r + \xi_{h,n\ell}^0(r) \left(\mathbf{e}_\theta \partial_\theta + \frac{1}{\sin \theta} \mathbf{e}_\phi \partial_\phi \right) \right] Y_\ell^m(\theta, \phi) \quad (4.2)$$

where $\xi_{r,n\ell}^0(r)$ and $\xi_{h,n\ell}^0(r)$ contain the radial dependency of the eigenfunction, and can be numerically calculated for a given stellar model. The eigenfrequencies $\omega_{0,n\ell}$ are degenerate in the azimuthal order m , as a consequence of spherical symmetry.

We considered two perturbations, the first one due to rotation and the second one caused by the presence of an active region that is rotating with the star. The last perturbation is unsteady in an inertial frame of reference. The two perturbations completely

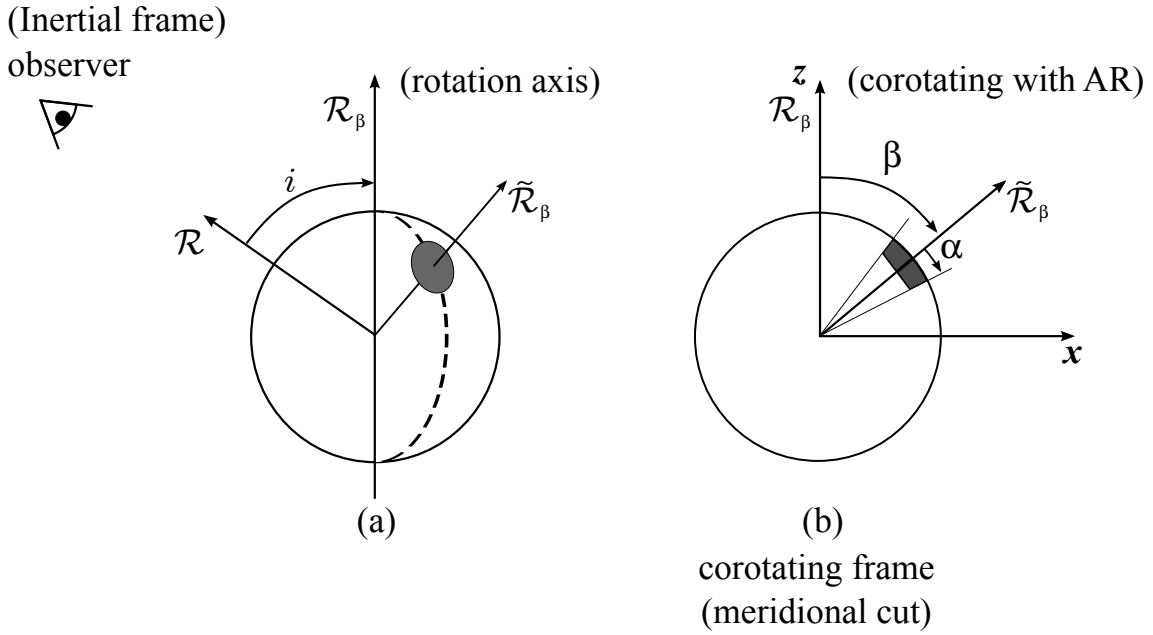


Figure 4.1: Reference frames and angles of the problem. Arrows denote the polar axes of the coordinate systems \mathcal{R} , \mathcal{R}_β , and $\tilde{\mathcal{R}}_\beta$. The frame \mathcal{R} is fixed with respect to the observer. The rotation axis of the star is inclined by an angle i with respect to the line of sight. The frames \mathcal{R}_β and $\tilde{\mathcal{R}}_\beta$ are corotating with the active region (shaded area) at a constant angular velocity Ω_β . The polar axis of \mathcal{R}_β is aligned with the stellar rotation axis. In \mathcal{R}_β the active region is placed at a colatitude β and in $\tilde{\mathcal{R}}_\beta$ is placed at the pole. In $\tilde{\mathcal{R}}_\beta$ the active region extends up to a colatitude α . The x and z axes in panel (b) are the Cartesian axes of the frame \mathcal{R}_β .

remove the $(2\ell + 1)$ -fold degeneracy in m . The effect of rotation of splitting the mode frequencies of a given $n\ell$ -multiplet is well known, however the combined effect of the two perturbations is not obvious a priori. Here we aim to investigate these effects on a single $n\ell$ -multiplet. In particular we are interested to seek the changes in the power spectrum of an observed light curve.

Provided that there is only one active region, one can choose a reference frame in which both perturbations are steady (assuming that rotation is independent of time). We defined three frames of reference, \mathcal{R} , \mathcal{R}_β , and $\tilde{\mathcal{R}}_\beta$, all three with the same origin at the center of the star. Figure 4.1 shows a sketch of the three frames. \mathcal{R} is an inertial frame whose polar axis points toward the observer and is inclined by an angle i with respect to the rotation axis of the star. The other two frames are both corotating with the active region at the angular velocity Ω_β with respect to \mathcal{R} . The polar axis of \mathcal{R}_β is parallel to the rotation axis of the star, while the polar axis of $\tilde{\mathcal{R}}_\beta$ is inclined by an angle β with respect to the rotation axis. In $\tilde{\mathcal{R}}_\beta$ the center of the active region is at the north pole.

The angular velocity Ω_β is equal to the surface rotational angular velocity of the star at the colatitude β . We call $\mathbf{r} = (r, \theta, \phi)$, $\mathbf{r}_\beta = (r, \theta_\beta, \phi_\beta)$, and $\tilde{\mathbf{r}}_\beta = (r, \tilde{\theta}, \tilde{\phi})$ the spherical-polar coordinates associated with \mathcal{R} , \mathcal{R}_β , and $\tilde{\mathcal{R}}_\beta$ respectively.

We first solved the problem in the reference frame \mathcal{R}_β : in this frame each eigenmode

of the multiplet solves the equation

$$\mathcal{H}\xi_M(\mathbf{r}_\beta) \equiv (\mathcal{H}_0 + O_\beta^{\text{ROT}} + O_\beta^{\text{AR}})\xi_M(\mathbf{r}_\beta) = \omega_M^2 \xi_M(\mathbf{r}_\beta) \quad (4.3)$$

where M identifies each one of the $2\ell + 1$ perturbed eigenmodes in the multiplet (with $-\ell \leq M \leq \ell$), with eigenfrequency ω_M and eigenfunction $\xi_M(\mathbf{r}_\beta)$. Here O_β^{ROT} and O_β^{AR} are the two operators describing the perturbations due to rotation and to the active region respectively. Both operators depend on the colatitude β of the active region.

If the two perturbations are small with respect to the spherically symmetric model, then to the lowest order of approximation the $2\ell + 1$ perturbed eigenfrequencies and eigenfunctions can be written in the corotating frame as

$$\omega_M(\beta) = \omega_0 + \delta\omega_M(\beta) \quad (4.4)$$

and

$$\xi_M(\mathbf{r}_\beta) = \sum_{m=-\ell}^{\ell} A_m^M(\beta) \xi_m^0(\mathbf{r}_\beta), \quad (4.5)$$

where ξ_m^0 are the unperturbed eigenfunctions of the same $n\ell$ -multiplet as given by Equations (4.1-4.2) ($n\ell$ subscripts are omitted to help reading), and where m is the azimuthal degree of the spherical harmonics $Y_\ell^m(\theta_\beta, \phi_\beta)$ in the frame \mathcal{R}_β . The M -degeneracy in \mathcal{R}_β is completely lifted because of the Coriolis force (Ledoux 1951). In writing the perturbed solutions we made the assumption that the perturbations do not mix states with different angular degrees or radial orders (*i.e.*, the sum in Equation (4.5) is only in m).

In order to find the perturbed solutions we first defined the inner product between two vectors $\xi(\mathbf{r}_\beta)$ and $\eta(\mathbf{r}_\beta)$ on the Hilbert space of vector displacements in the star as

$$\langle \xi, \eta \rangle = \int_V \xi^* \cdot \eta \rho dV \quad (4.6)$$

where $*$ denotes the complex conjugate. We normalize the mode eigenfunctions such that $\langle \xi_m^0, \xi_{m'}^0 \rangle = \delta_{mm'}$. By following the same procedure as Goode and Thompson (1992), we take the inner product of Equation (4.3) with $\xi_{m'}^0$

$$\langle \xi_{m'}^0, \mathcal{H}\xi_M \rangle = \omega_M^2 \langle \xi_{m'}^0, \xi_M \rangle,$$

to obtain

$$\sum_{m=-\ell}^{\ell} [O_{m'm}^{\text{ROT}}(\beta) + O_{m'm}^{\text{AR}}(\beta)] A_m^M(\beta) = \delta\omega_M(\beta) A_{m'}^M(\beta), \quad (4.7)$$

where the elements of the two perturbations matrices are

$$\begin{aligned} O_{m'm}^{\text{ROT}}(\beta) &= \frac{1}{2\omega_0} \langle \xi_{m'}^0, O_\beta^{\text{ROT}} \xi_m^0 \rangle, \\ O_{m'm}^{\text{AR}}(\beta) &= \frac{1}{2\omega_0} \langle \xi_{m'}^0, O_\beta^{\text{AR}} \xi_m^0 \rangle. \end{aligned} \quad (4.8)$$

By introducing the vector $\mathbf{A}^M = [A_{-\ell}^M, A_{-\ell+1}^M, \dots, A_{\ell}^M]^T$, Equation (4.7) can be rewritten in matrix form. Then $\delta\omega_M(\beta)$ and $\mathbf{A}^M(\beta)$ solve the eigenvalue problem

$$\mathbf{O}(\beta) \cdot \mathbf{A}^M(\beta) = \delta\omega_M(\beta)\mathbf{A}^M(\beta), \quad (4.9)$$

where the full perturbation matrix $\mathbf{O}(\beta)$ is

$$\mathbf{O}(\beta) = \mathbf{O}^{\text{ROT}}(\beta) + \mathbf{O}^{\text{AR}}(\beta). \quad (4.10)$$

While the rotation perturbation matrix $\mathbf{O}^{\text{ROT}}(\beta)$ in the frame \mathcal{R}_β is diagonal (since the angular velocity profile is axisymmetric in that frame), the matrix associated with the AR perturbation is not. However it can be obtained by first evaluating the diagonal perturbation matrix $\tilde{\mathbf{O}}^{\text{AR}}$ in the frame $\tilde{\mathcal{R}}_\beta$, and then rotating it to obtain the perturbation matrix

$$\mathbf{O}^{\text{AR}} = \mathbf{R}^{(\ell)}(0, -\beta, 0)\tilde{\mathbf{O}}^{\text{AR}}[\mathbf{R}^{(\ell)}(0, -\beta, 0)]^{-1} \quad (4.11)$$

in the frame \mathcal{R}_β , by means of the matrix operator $\mathbf{R}^{(\ell)}$ with elements $R_{Mm}^{(\ell)}(0, -\beta, 0) = r_{Mm}^{(\ell)}(-\beta) = r_{mM}^{(\ell)}(\beta)$, which performs the rotation $(\tilde{\theta}, \tilde{\phi}) \rightarrow (\theta_\beta, \phi_\beta)$ of the spherical harmonics

$$Y_\ell^m(\theta_\beta, \phi_\beta) = \sum_{M=-\ell}^{\ell} Y_\ell^M(\tilde{\theta}, \tilde{\phi})R_{Mm}^{(\ell)}(0, -\beta, 0) \quad (4.12)$$

via the Euler angles $(0, -\beta, 0)$, as defined by Messiah (1959). We note that in the case $\mathbf{O}^{\text{ROT}}(\beta) = 0$ (*i.e.*, in presence of solid body rotation and neglecting the effects of coriolis force and centrifugal distortion), the eigenvectors $\mathbf{A}^M(\beta)$ are the column vectors of the rotation matrix $\mathbf{R}^{(\ell)}(0, -\beta, 0)$, and we may identify $\xi_M(\mathbf{r}_\beta)$ with the pure spherical harmonic solutions $\xi_M^0(\tilde{\mathbf{r}}_\beta)$ with azimuthal degree M for the magnetic perturbation in the frame $\tilde{\mathcal{R}}_\beta$ of the active region.

4.2.1.1 Frequency splitting due to rotation

In the corotating frame \mathcal{R}_β , the rotation perturbation matrix takes the form

$$\begin{aligned} O_{mm'}^{\text{ROT}}(\beta) \simeq & \delta_{mm'} \left\{ m \int_V K_{n\ell m}(r, \theta_\beta) [\Omega(r, \theta_\beta) - \Omega_\beta] dV \right. \\ & \left. + m\Omega_\beta C_{n\ell} + \frac{\Omega_{eq}^2 R^3}{GM} Q_{2\ell m} \omega_{0,n\ell} \right\}, \end{aligned} \quad (4.13)$$

where $\Omega(r, \theta_\beta)$ is the internal angular velocity of the star and integration is performed over the entire volume V of the star. It follows that $\Omega_\beta = \Omega(R, \beta)$, R being the radius of the star. The functions $K_{n\ell m}(r, \theta_\beta)$ are the rotational kernels (Hansen et al. 1977), and $C_{n\ell}$ are the Ledoux constants (Ledoux 1951) that account for the effect of the Coriolis force. The last term describes the quadrupole distortion of the stellar surface due to the centrifugal forces (Kjeldsen et al. 1998), with

$$Q_{2\ell m} \simeq \frac{2/3 \int_{-1}^1 P_2(x) |P_\ell^{m|}(x)|^2 dx}{\int_{-1}^1 |P_\ell^{m|}(x)|^2 dx} = \frac{2}{3} \frac{\ell(\ell+1) - 3m^2}{(2\ell+3)(2\ell-1)} \quad (4.14)$$

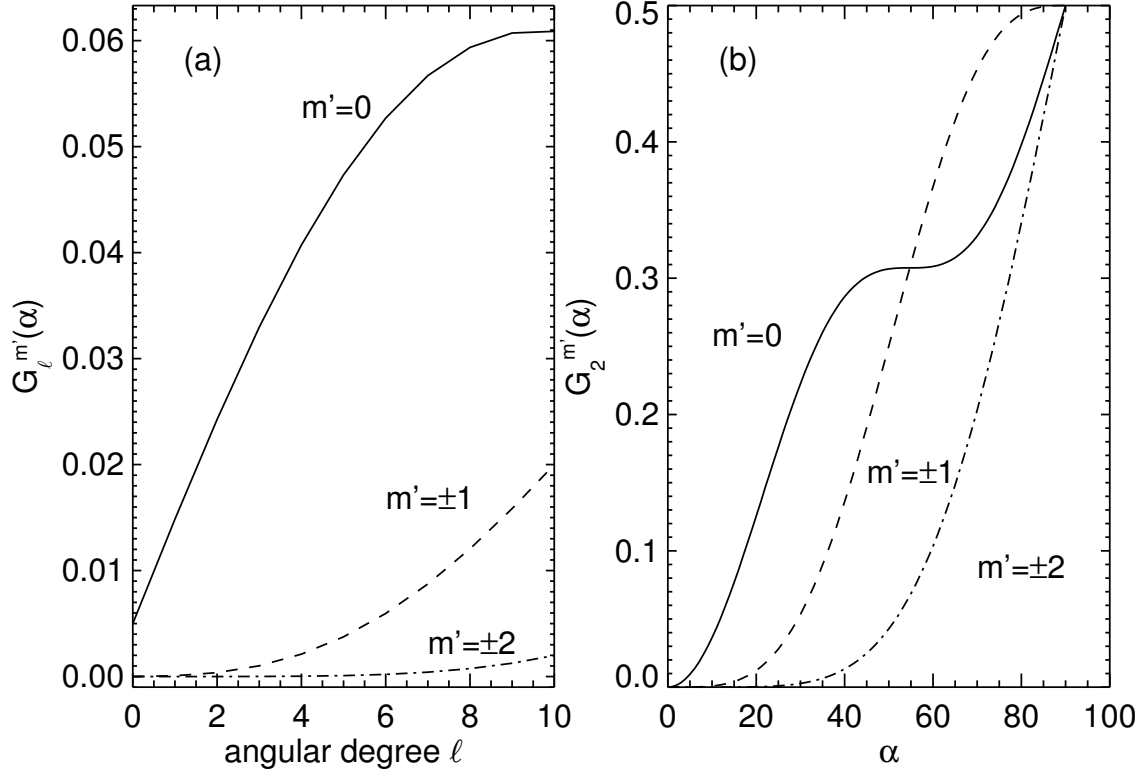


Figure 4.2: **(a):** Geometrical weight factor $G_\ell^{m'}(\alpha)$ vs. angular degree ℓ for $m = 0, \pm 1, \pm 2$ and $\alpha = 8^\circ$. **(b):** $G_\ell^{m'}(\alpha)$ vs. α for $\ell = 2$.

where $P_\ell^m(x)$ are the associated Legendre functions and P_2 is the Legendre polynomial of second order. This term is proportional to the ratio of the centrifugal to the gravitational forces at the surface $\Omega_{eq}^2 R^3 / (GM)$, where Ω_{eq} is the surface angular velocity at the equator, R is the radius of the star, M its mass, and G is the universal constant of gravity. The centrifugal term is very small in the case of slow rotators (Dziembowski and Goode 1992): for the Sun its relative contribution to the frequency shifts is $\sim 4 \cdot 10^{-6}$, *i.e.*, around 10 nHz at 3 mHz. However it increases rapidly with rotation, and already for stars rotating few times faster than the Sun is not negligible (Gizon and Solanki 2004). We note that, since the value of $Q_{2\ell m}$ is the same for azimuthal components with same $|m|$, the centrifugal term causes an asymmetric shift in the eigenfrequencies of the $n\ell$ -multiplet.

4.2.1.2 Frequency splitting due to the active region

Modeling the influence of surface magnetic fields on acoustic oscillations is a challenging problem (Gizon et al. 2010; Schunker et al. 2013). Here we choose to drastically simplify the physics and to focus on the geometrical aspects of the problem. Let us consider that the area of the active region extends up to a colatitude $\tilde{\theta} = \alpha$ (see Figure 4.1), and parametrize the perturbation matrix $\tilde{\mathbf{O}}^{\text{AR}}$ in the frame $\tilde{\mathcal{R}}_\beta$ in the form

$$\tilde{O}_{m'm''}^{\text{AR}} = \delta_{m'm''} \omega_{0,n\ell} \varepsilon_{n\ell} G_\ell^{m'}(\alpha), \quad (4.15)$$

with

$$G_\ell^{m'}(\alpha) = \frac{(2\ell + 1)(\ell - |m'|)!}{2(\ell + |m'|)!} \int_{\cos\alpha}^1 [P_\ell^{|m'|}(\mu)]^2 d\mu, \quad (4.16)$$

where $G_\ell^{m'}(\alpha)$ is a geometrical weight factor accounting for the surface coverage of the active region. For small values of α , this term sharply decreases as $|m'|$ increases, as shown in Figure 4.2a.

The parameter $\varepsilon_{n\ell}$ measures the relative magnitude of the effect of the AR perturbation and contains all the physics. If the perturbation is strongly localized near the surface then the value of $\varepsilon_{n\ell}$ increases with the radial order n , since the position of the upper turning point of a mode is frequency dependent. Calculating the actual value of $\varepsilon_{n\ell}$ goes beyond the scope of this work, and we will leave it as a parameter. We note that, while the value of $\varepsilon_{n\ell}$ is the same for the whole $n\ell$ -multiplet, $G_\ell^{m'}(\alpha)$ changes with m' and hence it will shape the multiplet in the observed power spectrum. The elements of the matrix \mathbf{O}^{AR} in \mathcal{R}_β finally read (see Equation 4.11)

$$O_{mm'}^{\text{AR}} = \omega_{0,n\ell} \varepsilon_{n\ell} \sum_{\mu=-\ell}^{\ell} G_\ell^\mu(\alpha) r_{m\mu}^{(\ell)}(-\beta) r_{m'\mu}^{(\ell)}(-\beta).$$

4.2.1.3 Power spectrum in the observer's frame: $(2\ell + 1)^2$ peaks

Given particular values for α , β , and $\varepsilon_{n\ell}$ the eigenvalue problem (4.9) can be solved. The last operation consists in transforming the solutions (4.4) and (4.5) to the observer's frame \mathcal{R} and to build a synthetic power spectrum, so to relate the results to observations.

As a first step we need to find an expression that relates (ω_M, ξ_M) to the observed intensity. For the sake of simplicity we assume that the variation $I(\theta_\beta, \phi_\beta, t)$ induced by the acoustic oscillations in the emergent photospheric intensity is proportional to the Eulerian pressure perturbation of the acoustic wavefield (Toutain and Gouttebroze 1993), measured at $r = R$ at the stellar surface. The pressure perturbation p of the acoustic wavefield is related to the displacement ξ through the linearized adiabatic equation

$$p = -\rho c_s^2 \nabla \cdot \xi - \xi \cdot \nabla P_0, \quad (4.17)$$

where P_0 and c_s^2 are the pressure and the squared adiabatic sound speed of the star. Through Equation (4.5), one can show that the pressure perturbation $p_M(r, \theta_\beta, \phi_\beta)$ of an eigenmode M takes the form

$$p_M(R, \theta_\beta, \phi_\beta) = \sum_{m=-\ell}^{\ell} A_m^M p_m^0(R, \theta_\beta, \phi_\beta) \propto \sum_{m=-\ell}^{\ell} A_m^M Y_\ell^m(\theta_\beta, \phi_\beta), \quad (4.18)$$

where $p_m^0(R, \theta_\beta, \phi_\beta)$ are the pressure eigenfunctions of the unperturbed stellar model.

Acoustic oscillations in Sun-like stars are stochastically excited and damped by turbulent convection, therefore the intensity variation is a random sample from a probability distribution. Since in the corotating frame \mathcal{R}_β the perturbation is steady, $I(\theta_\beta, \phi_\beta, t)$ is a

stationary process in that frame. An expression for the intensity variations $I(\theta_\beta, \phi_\beta, \omega)$ in the Fourier space that has the above statistical properties is

$$\begin{aligned} I(\theta_\beta, \phi_\beta, \omega) &\propto \sum_{M=-\ell}^{\ell} p_M(R, \theta_\beta, \phi_\beta) L_M^{1/2}(\omega) \mathcal{N}_M(\omega) \\ &\propto \sum_{M=-\ell}^{\ell} \sum_{m=-\ell}^{\ell} A_m^M Y_\ell^m(\theta_\beta, \phi_\beta) L_M^{1/2}(\omega) \mathcal{N}_M(\omega) \end{aligned} \quad (4.19)$$

where $L(\omega)$ is a Lorentzian line profile

$$L(\omega) = \left[1 + \left(\frac{\omega - \omega_M}{\Gamma/2} \right)^2 \right]^{-1}, \quad (4.20)$$

appropriate for exponentially damped oscillators (Anderson et al. 1990) with full width at half maximum (FWHM) Γ . In Equation (4.19) the $\mathcal{N}_M(\omega)$ are independent complex Gaussian random variables, with zero mean $E[\mathcal{N}_M(\omega)] = 0$ and unit variance

$$E[\mathcal{N}_{M'}^*(\omega') \mathcal{N}_M(\omega)] = \delta_{M'M} \delta_{\omega'\omega}. \quad (4.21)$$

Since $I(\theta_\beta, \phi_\beta, t)$ is real, in Equation (4.19) we only model the positive-frequency part of the spectrum. The negative-frequency part is related to the positive part by $I(\theta_\beta, \phi_\beta, -\omega) = I^*(\theta_\beta, \phi_\beta, \omega)$.

In the time domain, the intensity $I(\theta, \phi, t)$ as seen by the observer in the inertial frame \mathcal{R} is obtained through a passive rotation by the euler angles $(0, -i, \Omega_\beta t)$, that transforms $(\theta_\beta, \phi_\beta)$ to (θ, ϕ) , where $\theta = 0$ is the direction of the observer. To perform the rotation we take advantage of the spherical harmonic formulation. In the frequency domain, the rotation by the angle $\Omega_\beta t$ has the effect of shifting each m -component of $I(\theta_\beta, \phi_\beta, \omega)$ in frequency $\omega \rightarrow \omega - m\Omega_\beta$. The other rotation introduces the rotation matrix $r_{m'm}^{(\ell)}(-i)$, as defined by Messiah (1959). The intensity in the frame \mathcal{R} then reads

$$I(\theta, \phi, \omega) = \sum_{M=-\ell}^{\ell} \sum_{m=-\ell}^{\ell} \sum_{m'=-\ell}^{\ell} A_m^M Y_\ell^{m'}(\theta, \phi) r_{m'm}^{(\ell)}(-i) L_M^{1/2}(\omega - m\Omega_\beta) \mathcal{N}_M(\omega - m\Omega_\beta). \quad (4.22)$$

The observed disk-integrated intensity in the frequency domain is obtained by integrating the above equation over the visible disk

$$I_{\text{obs}}(\omega) = \int_0^{2\pi} d\phi \int_0^{\pi/2} d\theta I(\theta, \phi, \omega) W(\theta) \cos \theta \sin \theta, \quad (4.23)$$

where $W(\theta)$ is the limb-darkening function. The components with $m' \neq 0$ in Equation (4.22) vanish upon integration over ϕ , thus Equation (4.23) reduces to

$$I_{\text{obs}}(\omega) = V_\ell \sum_{M=-\ell}^{\ell} \sum_{m=-\ell}^{\ell} A_m^M r_{0m}^{(\ell)}(-i) L_M^{1/2}(\omega - m\Omega_\beta) \mathcal{N}_M(\omega - m\Omega_\beta), \quad (4.24)$$

where

$$V_\ell = \int_0^{2\pi} d\phi \int_0^{\pi/2} d\theta Y_\ell^0(\theta, \phi) W(\theta) \cos \theta \sin \theta \quad (4.25)$$

accounts for limb-darkening and projection effects. The matrix elements $r_{0m}^{(\ell)}(-i)$ may be written explicitly in terms of the associated Legendre polynomials (Messiah 1959):

$$r_{0m}^{(\ell)}(-i) = (-1)^m \sqrt{\frac{(\ell - m)!}{(\ell + m)!}} P_\ell^m(\cos i).$$

Let us call $P(\omega) = |I_{\text{obs}}(\omega)|^2$ the observed power spectrum of the oscillations. $P(\omega)$ is a realization of the expected power spectrum $\mathcal{P}(\omega)$. The expectation value of the power spectrum is a sum over terms of the form $E[\mathcal{N}_M^*(\omega - m\Omega_\beta)\mathcal{N}_{M'}(\omega - m'\Omega_\beta)]$, where indices M, m, M', m' are integers between $-\ell$ and $+\ell$. These terms are zero for $M \neq M'$ or $m \neq m'$, therefore the formula

$$\mathcal{P}(\omega) \equiv E[P(\omega)] = \sum_{M=-\ell}^{\ell} \sum_{m=-\ell}^{\ell} P_m^M(i, \beta) L_M(\omega - m\Omega_\beta) \quad (4.26)$$

describes the observed limit power spectrum. For positive frequencies, $\mathcal{P}(\omega)$ for a $n\ell$ -multiplet is then the sum of $(2\ell + 1)^2$ Lorentzian profiles, centered at frequencies

$$\omega_m^M(\beta) = \omega_M(\beta) + m\Omega_\beta = \omega_0 + \delta\omega_M(\beta) + m\Omega_\beta \quad (4.27)$$

with peak amplitudes

$$P_m^M(i, \beta) = \frac{(\ell - |m|)!}{(\ell + |m|)!} \left[V_\ell A_m^M(\beta) P_\ell^{|m|}(\cos i) \right]^2. \quad (4.28)$$

4.2.2 Power spectrum: asymmetric profiles and blended peaks in $n\ell$ -multiplets

In this section we evaluated the signal imprinted in a $\ell = 2, n = 18$ multiplet by a large active region, in a star rotating with a period of 8 days, *i.e.*, ~ 3.5 times faster than the Sun. For the calculation of the unperturbed eigenmodes $(\omega_{n\ell}, \xi_{n\ell})$ we employed the ADIPLS software package (Christensen-Dalsgaard 2008a), using the solar Model S (Christensen-Dalsgaard et al. 1996) as background model. The unperturbed frequency of the multiplet is $\omega_{n\ell}/2\pi \simeq 2756.95 \mu\text{Hz}$.

4.2.2.1 Rotation model

To calculate the rotational splitting we used the rotation profile of Gizon and Solanki (2004), rescaled to the desired rotation period. Figure 4.3 shows the rotational splittings of the $\ell = 2, n = 18$ multiplet as a function of β and in the frame \mathcal{R}_β , as given by Equation (4.13). The shifts are negative for negative azimuthal orders (the opposite applies to positive m values) if the active region is at the pole, but they increase as the AR colatitude increases. Gray lines show the splittings for $m = 0, -1, -2$ resulting from the neglect of the centrifugal distortion (splittings for $m > 0$ have opposite sign with respect to those with negative m s). The centrifugal term considerably affects the rotational splittings, for it shifts the $m = 0$ mode and introduces an asymmetry in the shifts between positive and negative azimuthal orders m , with a maximum frequency shift of more than 100 nHz. Therefore this term must be included when performing the analysis.

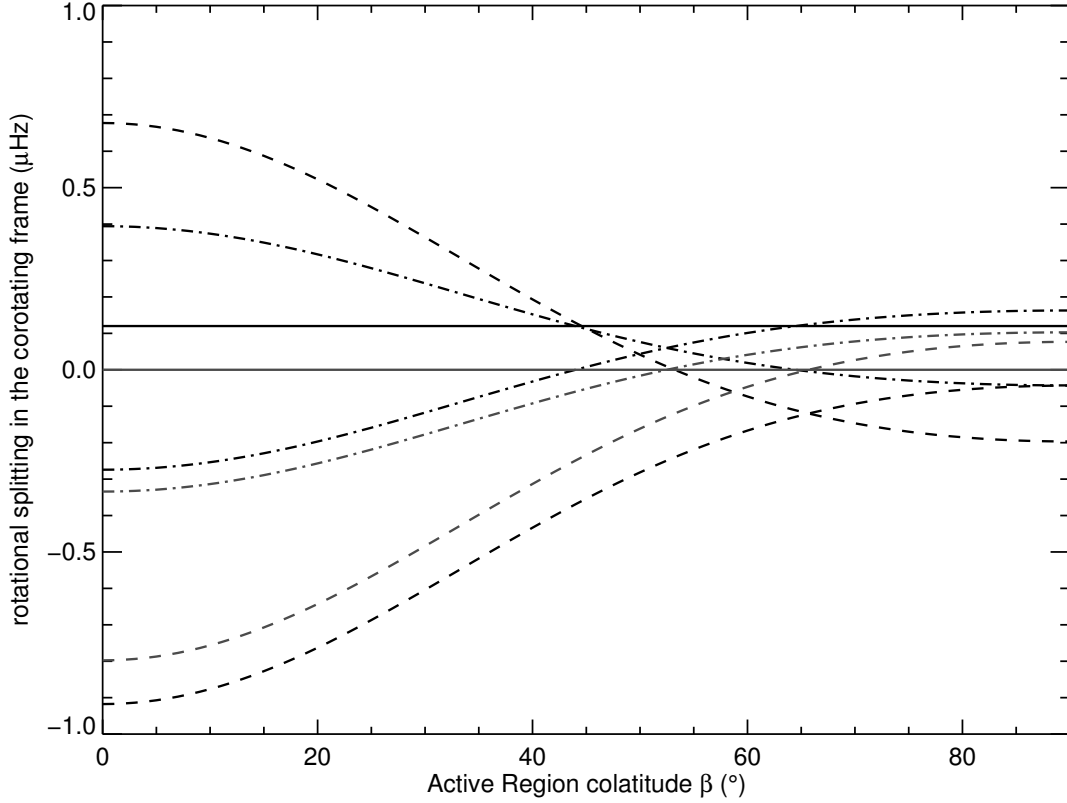


Figure 4.3: Rotational splittings $O_{mm}^{\text{ROT}}(\beta)$ of the $\ell = 2, n = 18$ multiplet vs. active region colatitude β , as given by Equation (4.13) (black lines) for a star with a rotation period of 8 days, for $m = 0$ (solid line), $|m| = 1$ (dash-dotted line) and $|m| = 2$ (dashed line). The gray lines are the resulting splittings if one neglects the centrifugal term. In this case only zero and negative m s are shown, and positive m values satisfy $O_{-m-m}^{\text{ROT}}(\beta) = -O_{mm}^{\text{ROT}}(\beta)$.

4.2.2.2 Model parameters for a large active region

Modeling the effects of surface magnetic activity on acoustic oscillations is challenging: there are indeed direct effects associated with the magnetic fields (see, *e.g.*, Gough and Thompson 1990), but also indirect effects due to changes in the stellar stratification caused by activity. To give an estimate of $\varepsilon_{n\ell}$ we considered only the indirect effects and we assumed that the active region changes only the internal sound speed stratification. By labeling with Δc^2 the signed square of this change, we can write an expression for $\varepsilon_{n\ell}$ in the form (see Papini et al. 2015, and Equation (3.12))

$$\varepsilon_{n\ell} = \int_{\text{AR}} \Delta c^2(r) \left[\frac{1}{r} \partial_r (r^2 \xi_{r,n\ell}(r)) - \ell(\ell+1) \xi_{h,n\ell}(r) \right]^2 \rho(r) dr \times \left(2\omega_{n\ell}^2 \int_V \|\xi\|^2 \rho dV \right)^{-1} \quad (4.29)$$

where $\rho(r)$ is the density of the stellar background. Here the integral concerning the perturbation is performed over the active region and the boundary conditions are kept unchanged.

From observations of p -mode frequency changes during the solar cycle, Libbrecht and Woodard (1990) have shown that the (positive) frequency shifts are almost independent on ℓ and increase with frequency, thus indicating that the effects of magnetic activity on acoustic oscillations are confined near the surface. Assuming that the perturbation extends a few pressure scale heights deep just below the photosphere, and setting $\Delta c^2/c^2 \simeq 10\%$ in that region, we obtained $\varepsilon_{n\ell} = 0.003$ for $\ell = 2, n = 18$. This estimate is far from being realistic, but it provides a basis to work with.

The surface coverage of active regions in stars, as inferred by Doppler imaging of dark spots, spans from less than percent up to 11% (Strassmeier 2009). Here we focused on two different surface coverages of 4% and 8% respectively, and set $\cos \alpha = 0.92$ and 0.84 accordingly (*i.e.*, $\alpha \simeq 23^\circ$ and 32°) in Equation (4.16). We considered three AR colatitudes $\beta = 20^\circ, 50^\circ, \text{ and } 80^\circ$, *i.e.* one near the pole of the star, one at mid latitudes, and the last near the equator.

4.2.2.3 Example power spectrum for the $\ell = 2, n = 18$ multiplet

We solved the eigenvalue problem (4.9) for the selected set of values of α, β , and $\varepsilon_{n\ell}$, by employing Jacobi's method (Press et al. 1992). The explicit expression for the rotation matrices was found by using the Wigner formula (Messiah 1959).

Figure 4.4 displays the different contributions to the frequency changes induced by rotation and the AR perturbation, together with the theoretical peaks in the observed acoustic power, for one of the selected cases. The peak amplitudes were calculated by using Equation (4.28) and by employing the formulation of Pierce (2000) for the limb-darkening function.

Figure 4.5 to 4.10 show the resulting observed power spectra in the different configurations for three different angles of observation, $i = 30^\circ, 50^\circ, \text{ and } 80^\circ$ respectively. The corresponding theoretical Lorentzian envelope (solid line) was calculated by means of Equation (4.26). In the spectrum we set a value for the FWHM of $\Gamma/2\pi = 1 \mu\text{Hz}$, typical for this multiplet in the Sun (Chaplin et al. 2005).

As a common feature in all spectra only the $M = 0$ component in each m -quintuplet displays a significant shift. All the other peaks are clustered near the frequencies of pure rotational splitting (see also Figure 4.4). This is due to the fact that the axisymmetric modes in the reference frame $\tilde{\mathcal{R}}_\beta$ of the active region are more affected by the AR perturbation (as found in Papini et al. 2015). As result the term with $m' = m'' = 0$ in $\tilde{\mathbf{O}}^{\text{AR}}$ is dominant, and so is the corresponding eigenvalue $\delta\omega_{M=0}$. However with increasing surface coverage also the frequency shifts of the non-axisymmetric modes increase and the peaks get less clustered. This behavior arises only from geometry considerations.

The peaks within the same m -quintuplet reveal a fine structure, and all the peaks have different amplitudes, thus resulting in an asymmetric profile for the Lorentzian envelope. It is evident that is not possible to resolve all the $(2\ell + 1)^2$ peaks of the spectrum, and an observer would identify only some more than $2\ell + 1$ peaks. In particular in the cases shown here it is possible to identify from 5 to 6 peaks for $i = 80^\circ$, up to 7 for 55° , and from 3 to 5 for $i = 30^\circ$, the additional peaks coming from the most shifted $M = 0$ mode. Because of the big shift in frequency the $M = 0$ peaks are blended with peaks of different m -quintuplets. This blending increases with activity (Figures 4.8 -4.10). As a consequence is not possible to identify a Lorentzian profile for each single m -quintuplet.

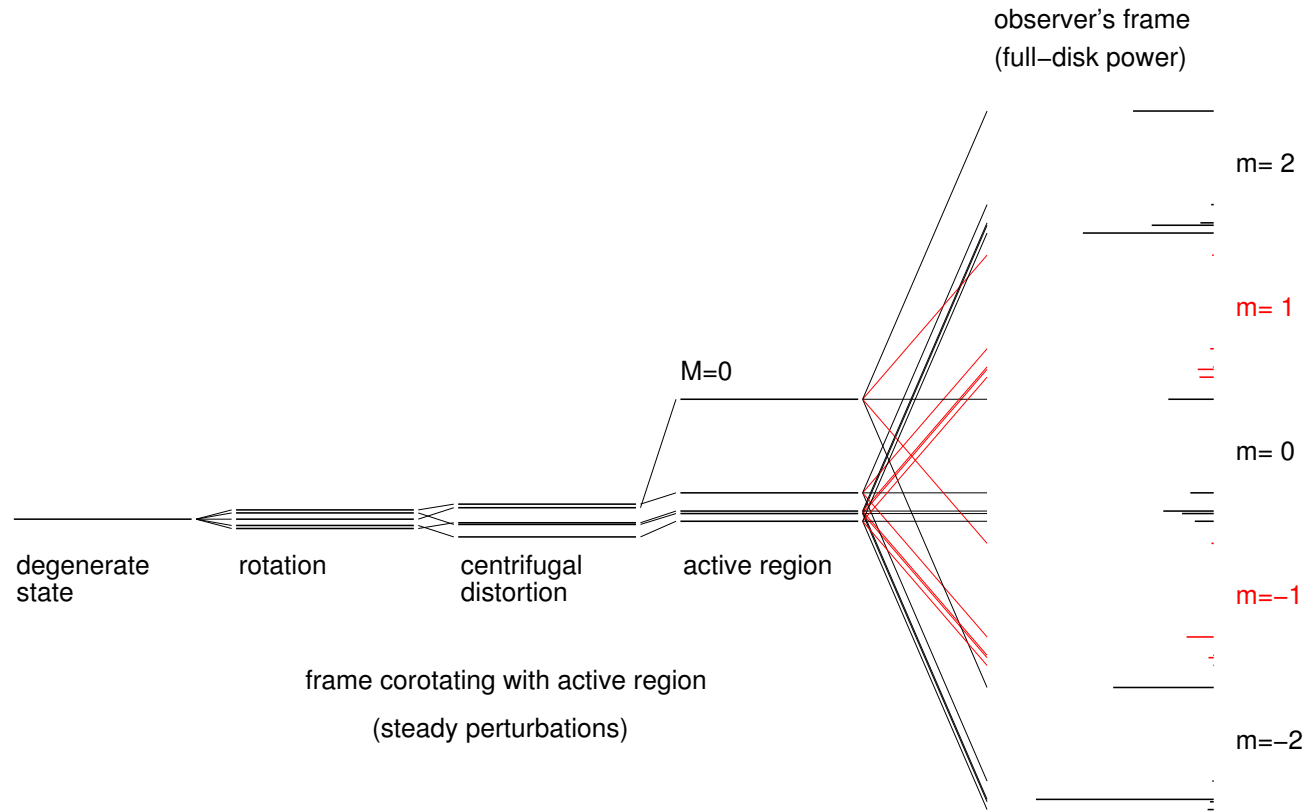


Figure 4.4: Schematic diagram for the $\ell = 2, n = 18$ mode, showing how the different contributions remove the degeneracy of the nonrotating nonmagnetic star and produce $2\ell + 1$ different eigenfrequencies in the frame corotating with the active region, for a star with a rotation period of 8 days and in the case of $\varepsilon_{nl} = 0.003, \beta = 80^\circ$ and $\alpha = 23^\circ$, that correspond to $\Omega_\beta/2\pi = 1.504 \mu\text{Hz}$. The $M = 0$ eigenmode is the most shifted. Also shown the resulting $(2\ell + 1)^2$ peaks of the acoustic power as seen in the observer's frame, with an inclination angle $i = 80^\circ$, for $m = 0, \pm 2$ (black) and for $m = \pm 1$ (red).

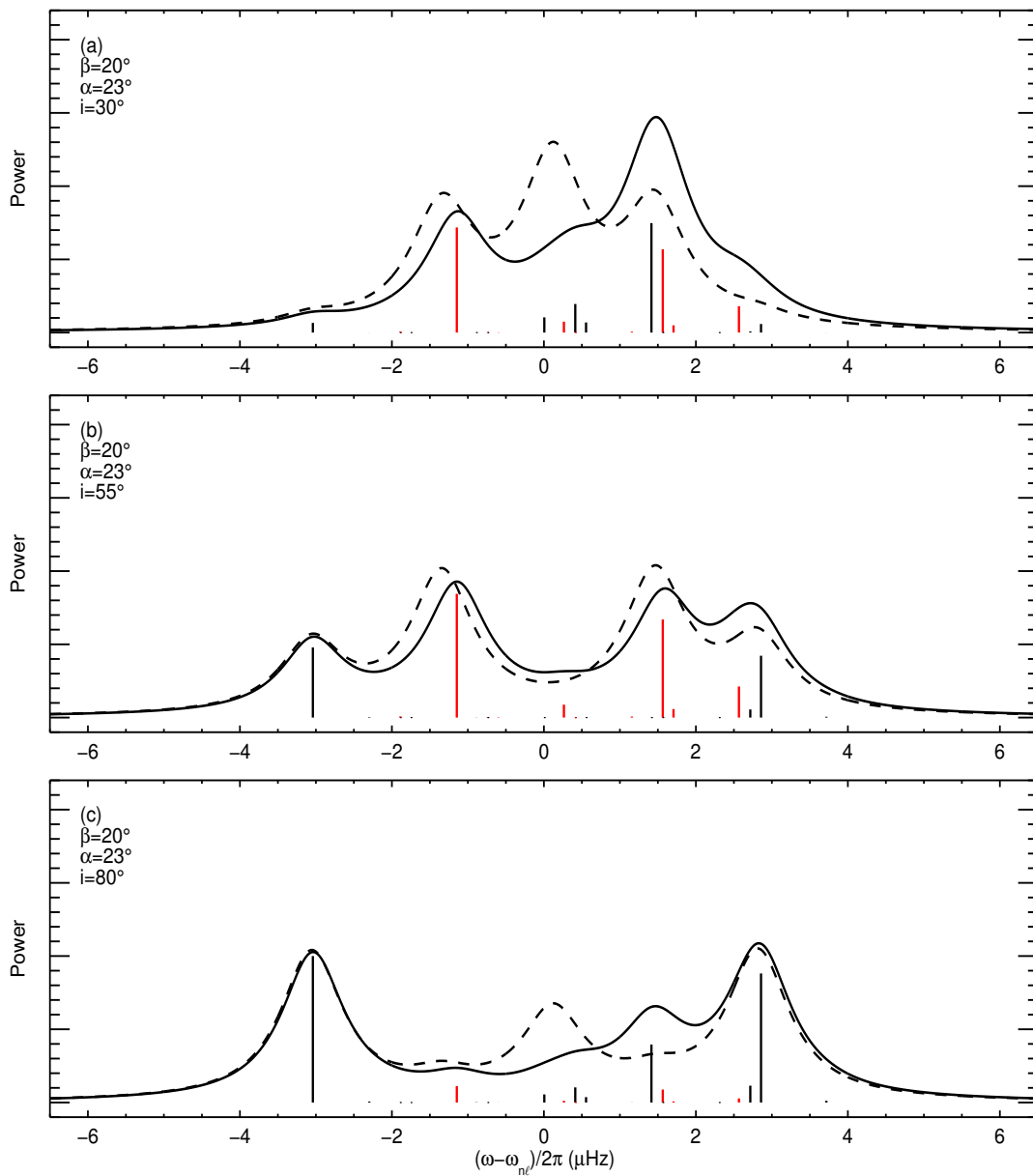


Figure 4.5: Acoustic power vs. $(\omega - \omega_{nl})/2\pi$ for the $\ell = 2$, $n = 18$ multiplet observed at three inclination angles $i = 30^\circ$, $i = 55^\circ$, and 80° , for a star with a rotation period of 8 days and in the case of an active region with $\varepsilon_{nl} = 0.003$, $\beta = 20^\circ$, and for a surface coverage with $\alpha = 23^\circ$. Vertical lines show the theoretical peaks for $m = 0, \pm 2$ modes (black) and $m = \pm 1$ modes (red). The resulting Lorentzian envelope (solid line) was obtained by using the solar value of $1 \mu\text{Hz}$ for the FWHM. The dashed line plots the observed pure rotational spectrum, which is asymmetric because of centrifugal distortion (Equation (4.13)).

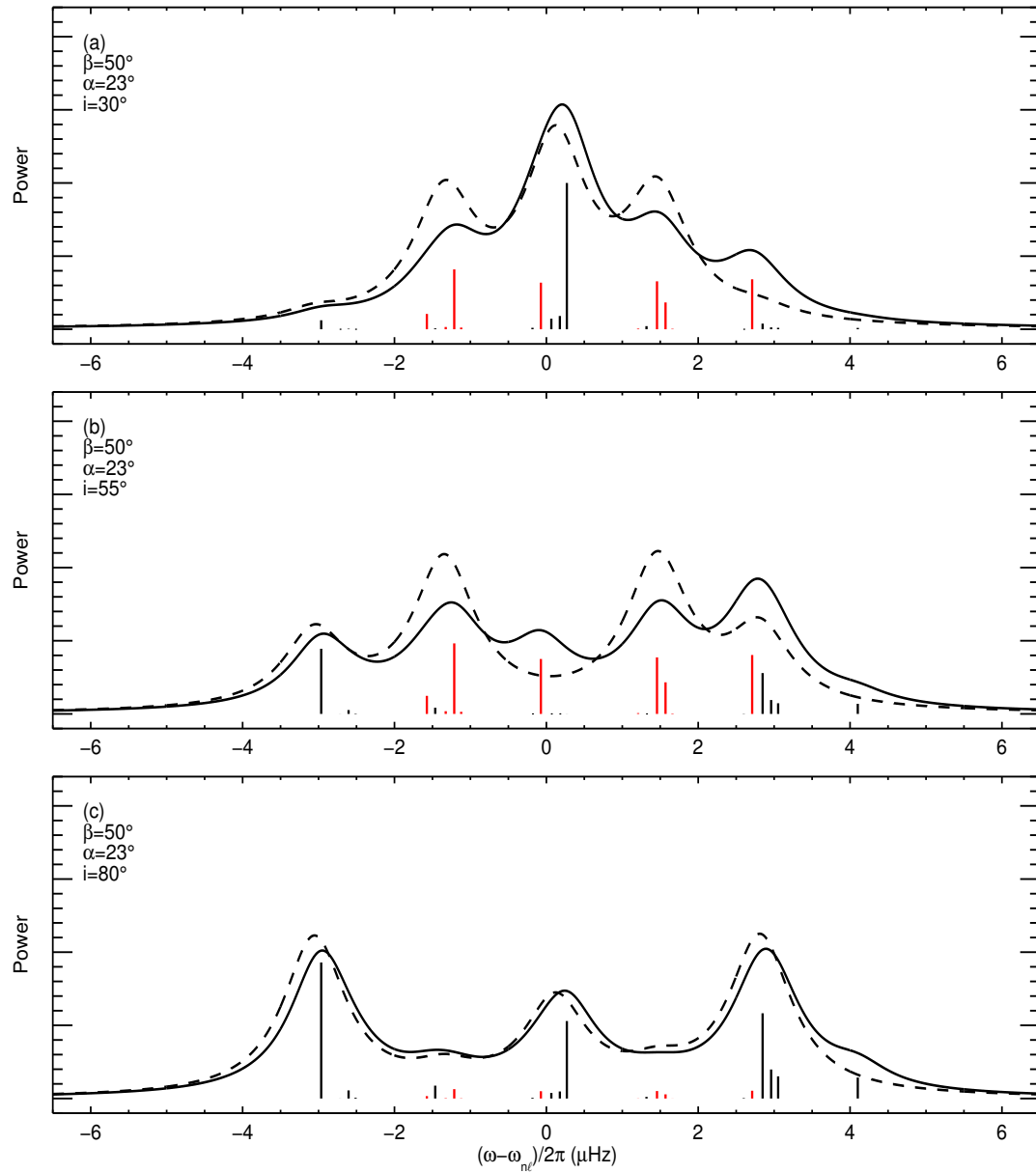


Figure 4.6: Same as in Figure 4.5, but for an AR colatitude $\beta = 50^\circ$.

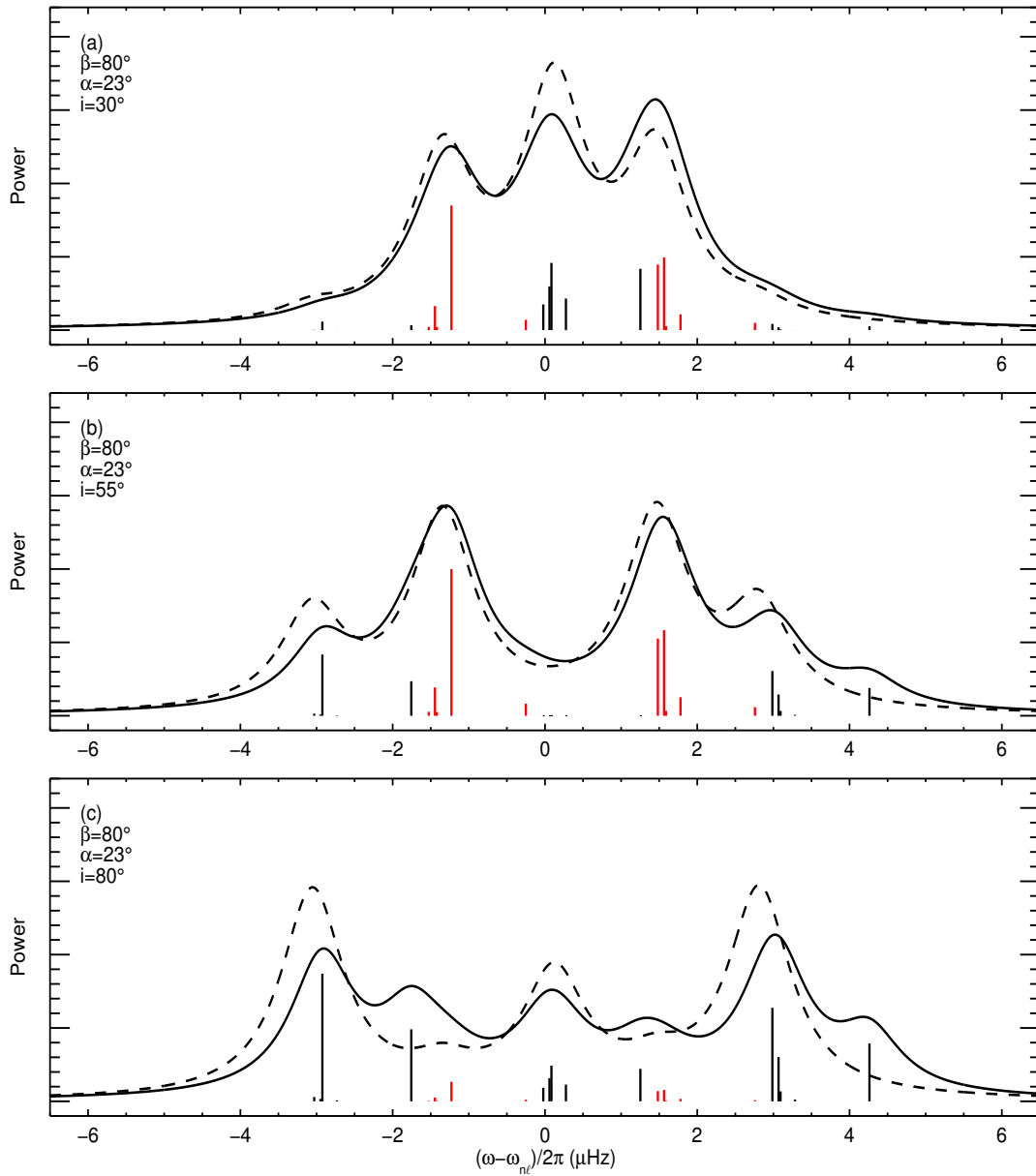


Figure 4.7: Same as in Figure 4.5, but for an AR colatitude $\beta = 80^\circ$.

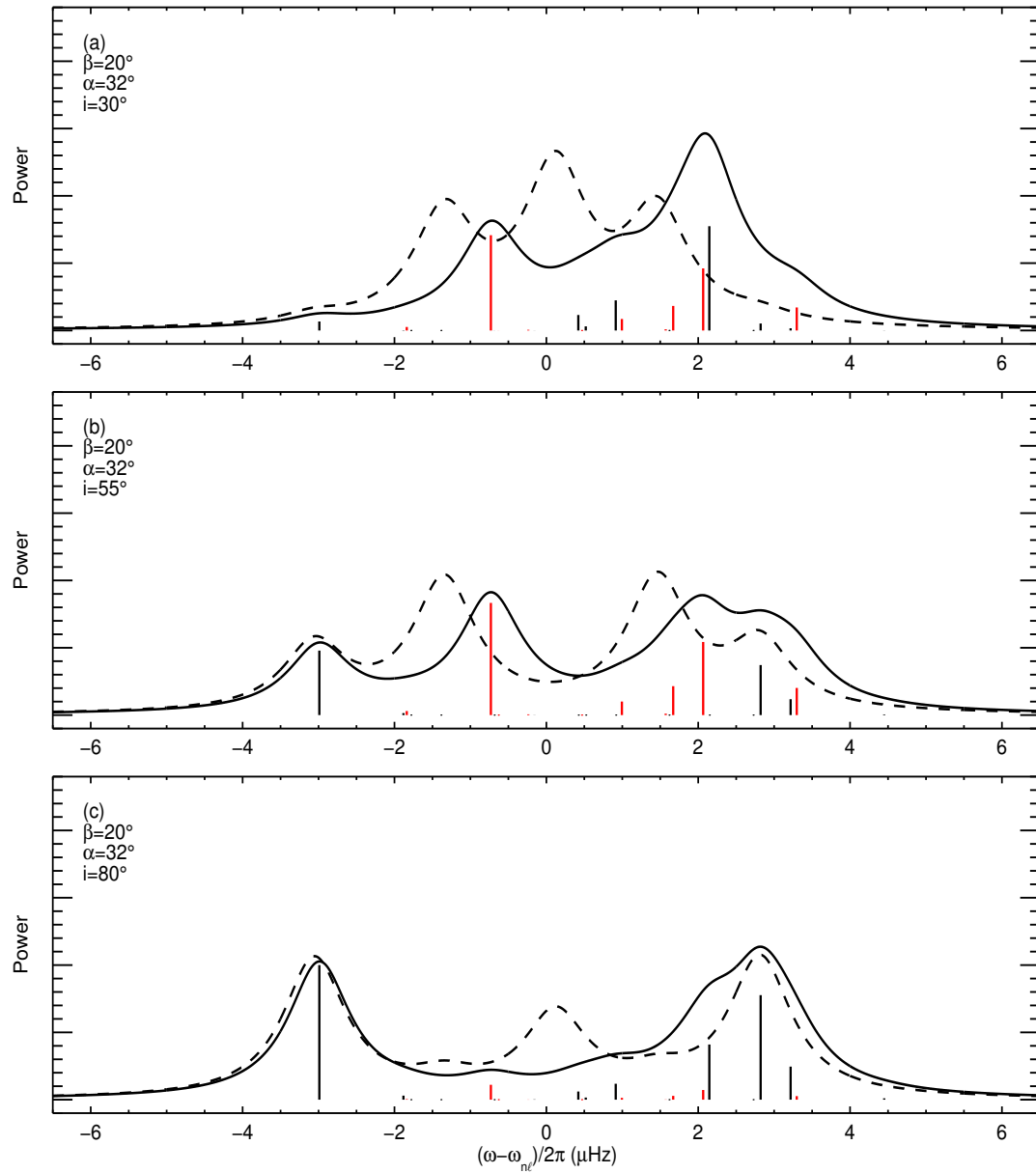


Figure 4.8: Same as in Figure 4.5, but for a surface coverage with $\alpha = 32^\circ$.

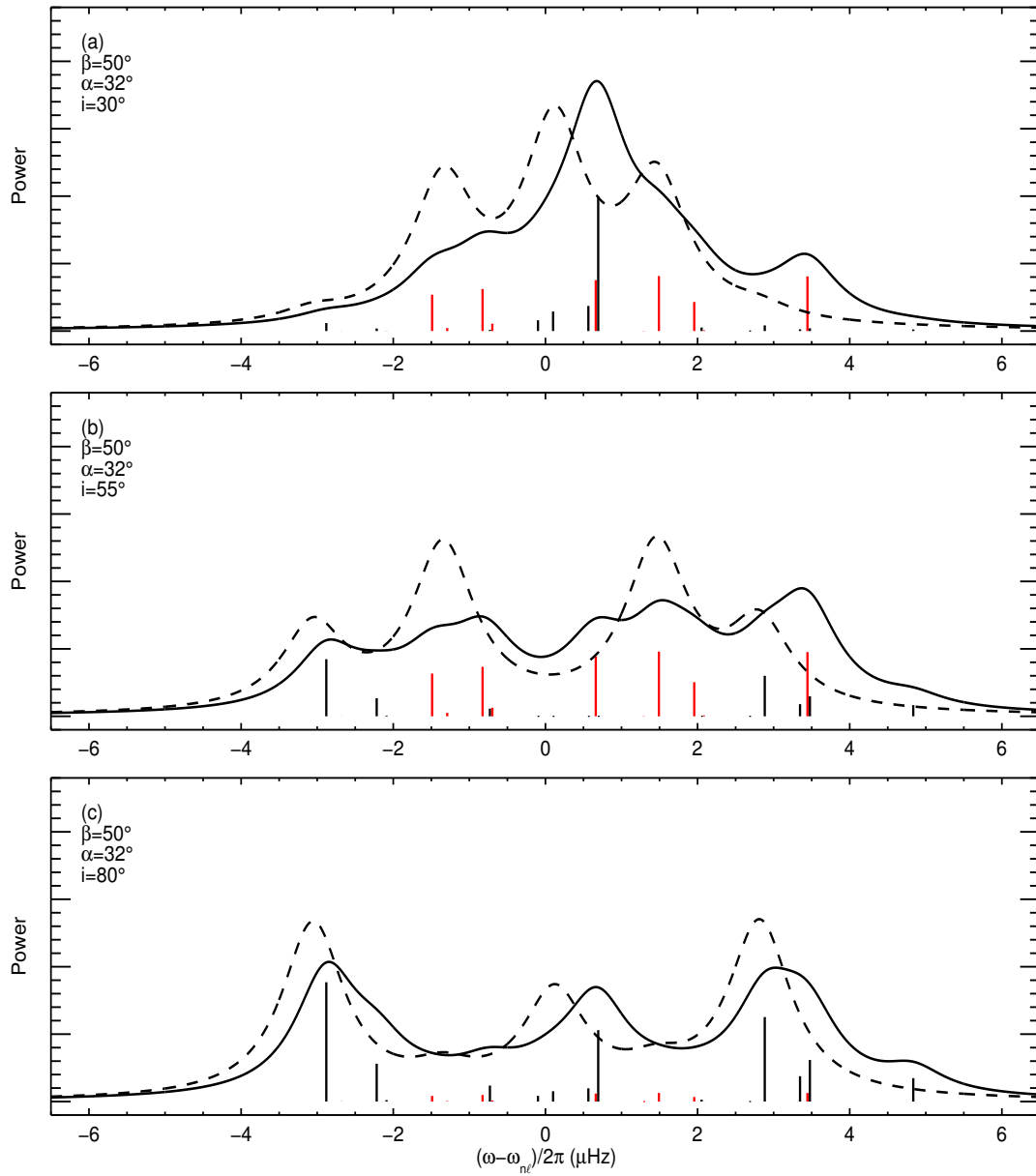


Figure 4.9: Same as in Figure 4.5, but for an AR colatitude $\beta = 50^\circ$ and a surface coverage with $\alpha = 32^\circ$.

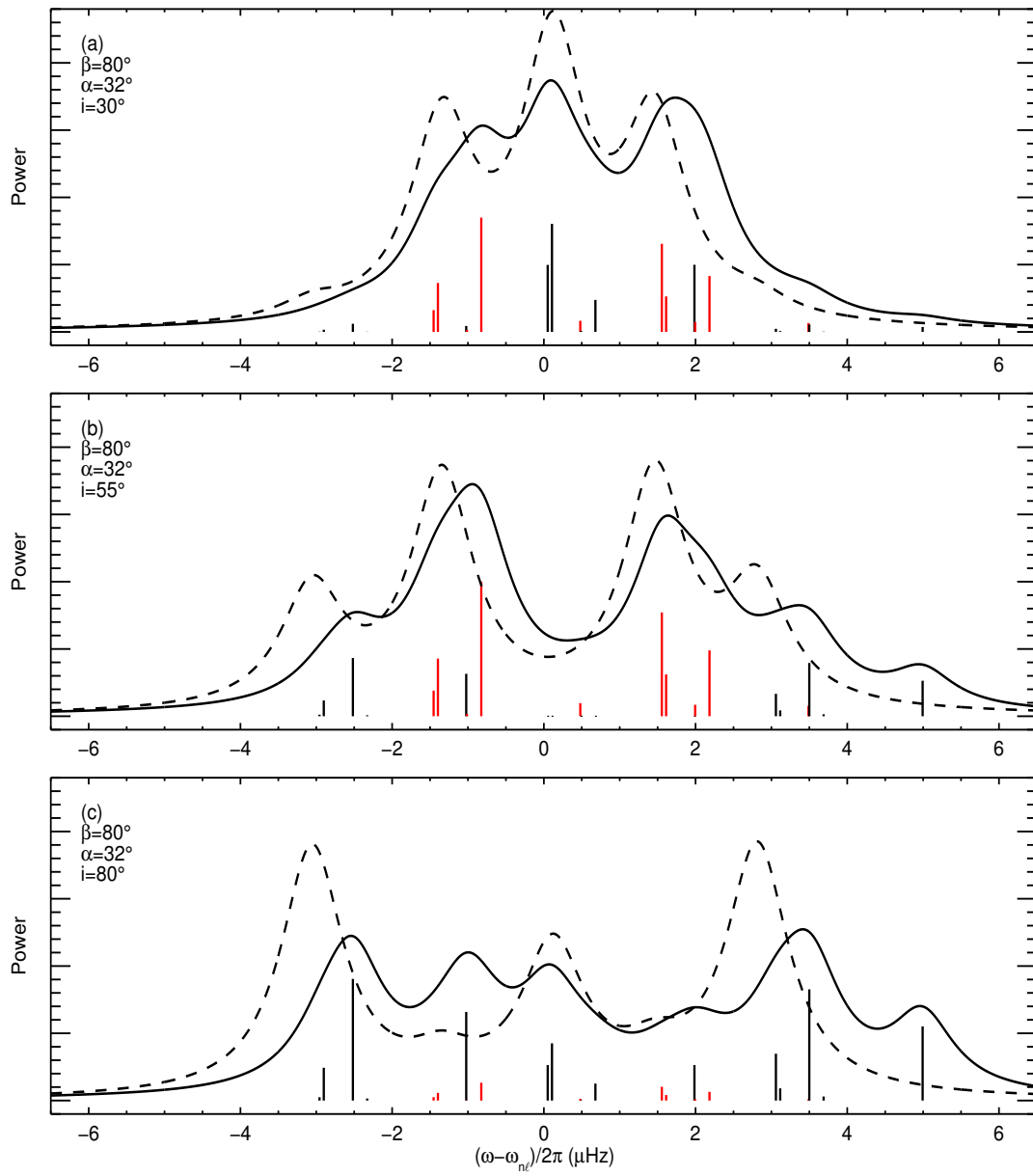


Figure 4.10: Same as in Figure 4.5, but for an AR colatitude $\beta = 80^\circ$ and a surface coverage with $\alpha = 32^\circ$.

This would happen also with decreasing rotation period. Figure 4.8a shows an extreme case in which both the $M = 0, m = 0$ and the $M = 1, m = 1$ peaks equally contribute to form one Lorentzian peak.

The resulting observed Lorentzian envelope is very sensitive to the latitudinal position of the AR and to the inclination angle: the observed spectrum in Figure 4.7a is near the pure rotational spectrum, while the same configuration observed from a different inclination angle (Figure 4.7c) shows a more asymmetric profile with additional peaks. The sensitivity of the spectrum to the colatitude of the AR is evident by looking at the differences between the figures, and is due both to the variation with β of the rotational splittings (Figure 4.3) and to the increasing amplitude with β of the nondiagonal elements in the rotation matrix $\mathbf{R}^{(\ell)}$ in Equation (4.10). Spectra with same colatitude β and inclination angle i , but different surface coverage α , are similar, this however do not indicates that the shape of the Lorentzian profiles has a weak dependence on the surface coverage of the AR, but rather that the effect of $G_\ell^m(\alpha)$ in these two cases is similar, as can be deduced from Figure 4.2b.

In a real observation the power spectrum is not as clean as in the previous figures, due to the stochastic excitation of the acoustic modes induced by the near-surface turbulent convection and to noise, whose origin is both stellar and instrumental. To illustrate this effect, in Figures 4.11-4.13 the power spectra in the cases of higher activity (Figures 4.8-4.10) have been replotted together with a realization of the power spectrum, created by taking the modulus squared of Equation (4.24). An additional Gaussian random noise with a signal-to-noise ratio of 100 was prescribed (see, *e.g.*, Gizon and Solanki 2003). Indeed the realization noise considerably degrades the spectrum, however in some cases is still possible to distinguish between the pure rotational spectrum and the spectrum resulting from the presence of the AR.

Figures 4.11-4.13 suggest that the asymmetry in the Lorentzian envelope is the observable imprint of the active region in the power spectrum. In a simple attempt to characterize it we calculated the mean frequency shifts of each m -quintuplet in the $\ell = 2, n = 18$ multiplet, by taking a power-weighted average of the clustered $M \neq 0$ frequency shifts for each m . Remarkably, the resulting averaged shifts are independent on the inclination angle, since all the peaks within the same m -quintuplet have the same visibility. Therefore for an AR with a given strength and surface coverage they only depend on the colatitude β . Figure 4.14 shows a contour of the observed power spectrum with $i = 80^\circ$ and $\alpha = 23^\circ$ as a function of β , with superimposed the power-weighted averaged frequency shifts of the $M \neq 0$ peaks (red-dashed lines) and the shifts of the $M = 0$ peaks (red-dotted lines). The averaged shifts nicely follow the Lorentzian peaks. We also see that except for the uppermost $M = 2, m = 2$ peak, all the other $M = 0$ peaks overlap with the averaged $M \neq 0$ peaks, making difficult to separate the contributions to the power spectrum of the single m -quintuplets.

In Figure 4.15 we further averaged the frequency shifts over the same $|m|$. Therefore the final averages are independent on both the inclination angle and rotation, with the exception of centrifugal distortion, and only depend on the AR perturbation. This is the imprint in the observed frequencies of the active region. Here we clearly see the dependence of the frequency shifts on the AR colatitude: the shifts are maximum with the AR at the pole, and then generally decrease (in absolute value) as the AR latitude decreases. The solid thick line indicates the shifts of the $M = 0$ peaks averaged over $|m|$,

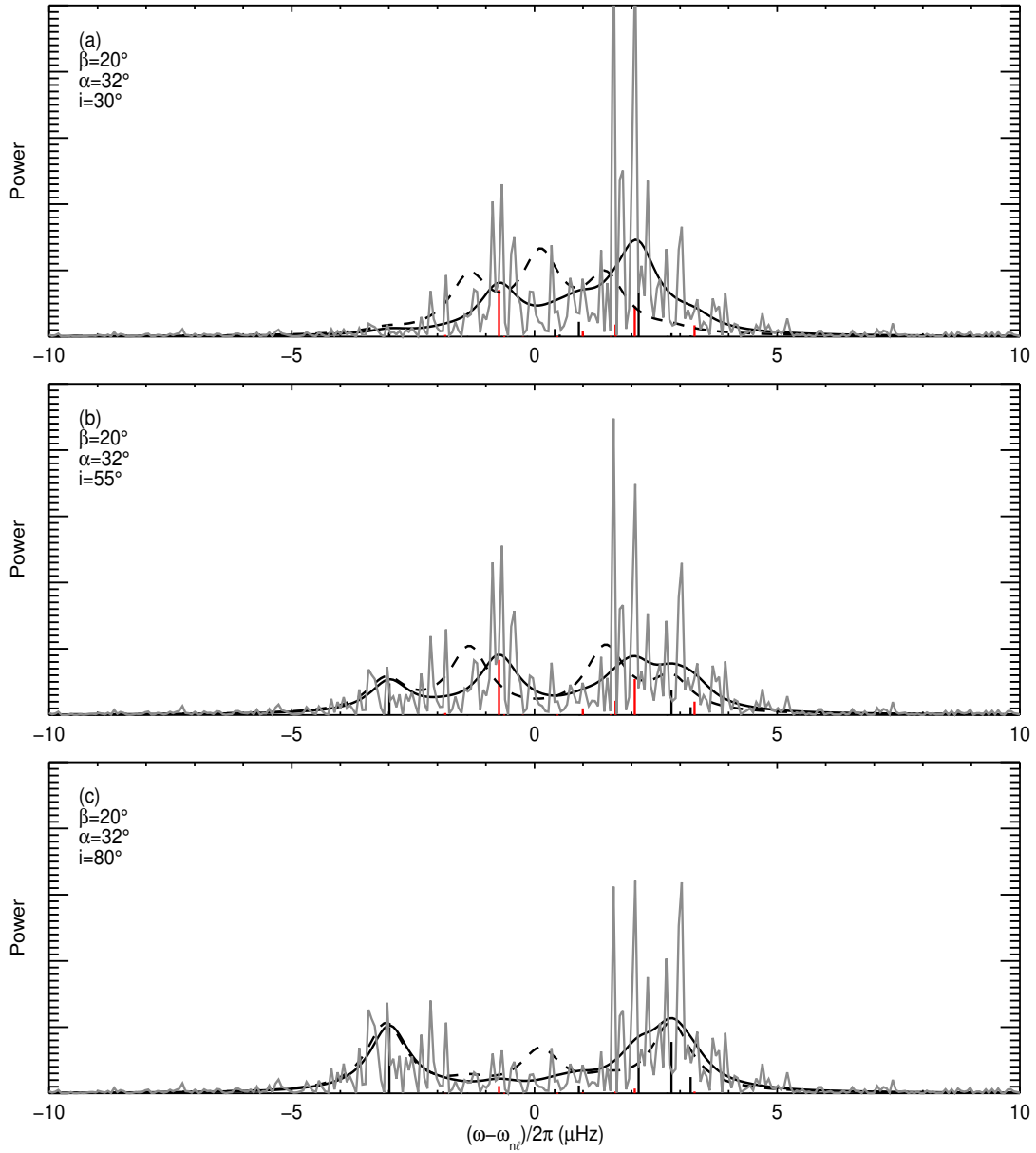


Figure 4.11: Three realizations of the power spectrum (gray lines) of the theoretical spectra in Figure 4.8. The Lorentzian envelope (solid line) was used as expectation value for the power spectrum. The dashed line plots the observed pure rotational spectrum corresponding to 6 months of continuous observations. A signal-to-noise ratio of 100 has been used.

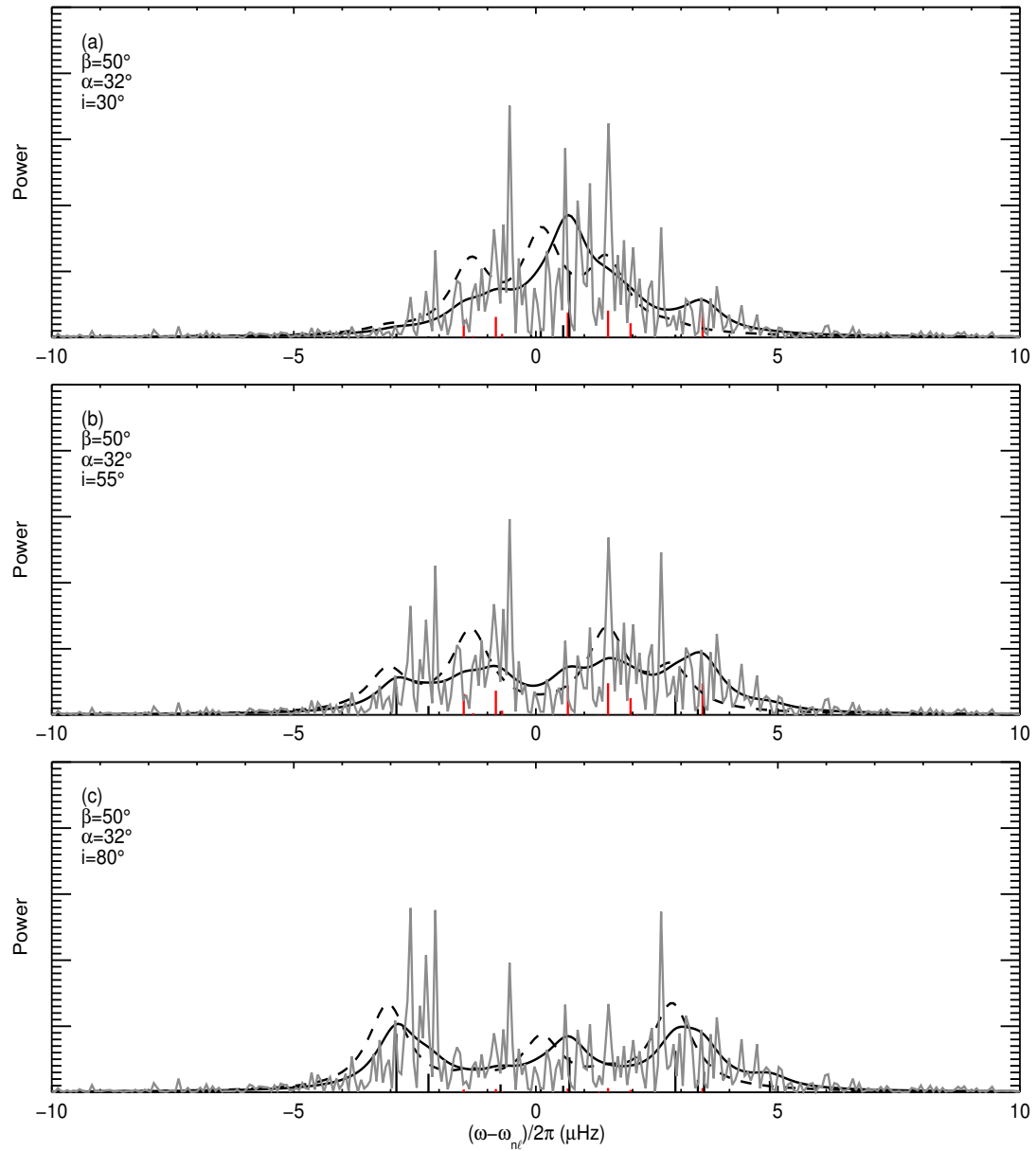


Figure 4.12: Same as in Figure 4.11, but for an AR colatitude $\beta = 50^\circ$.

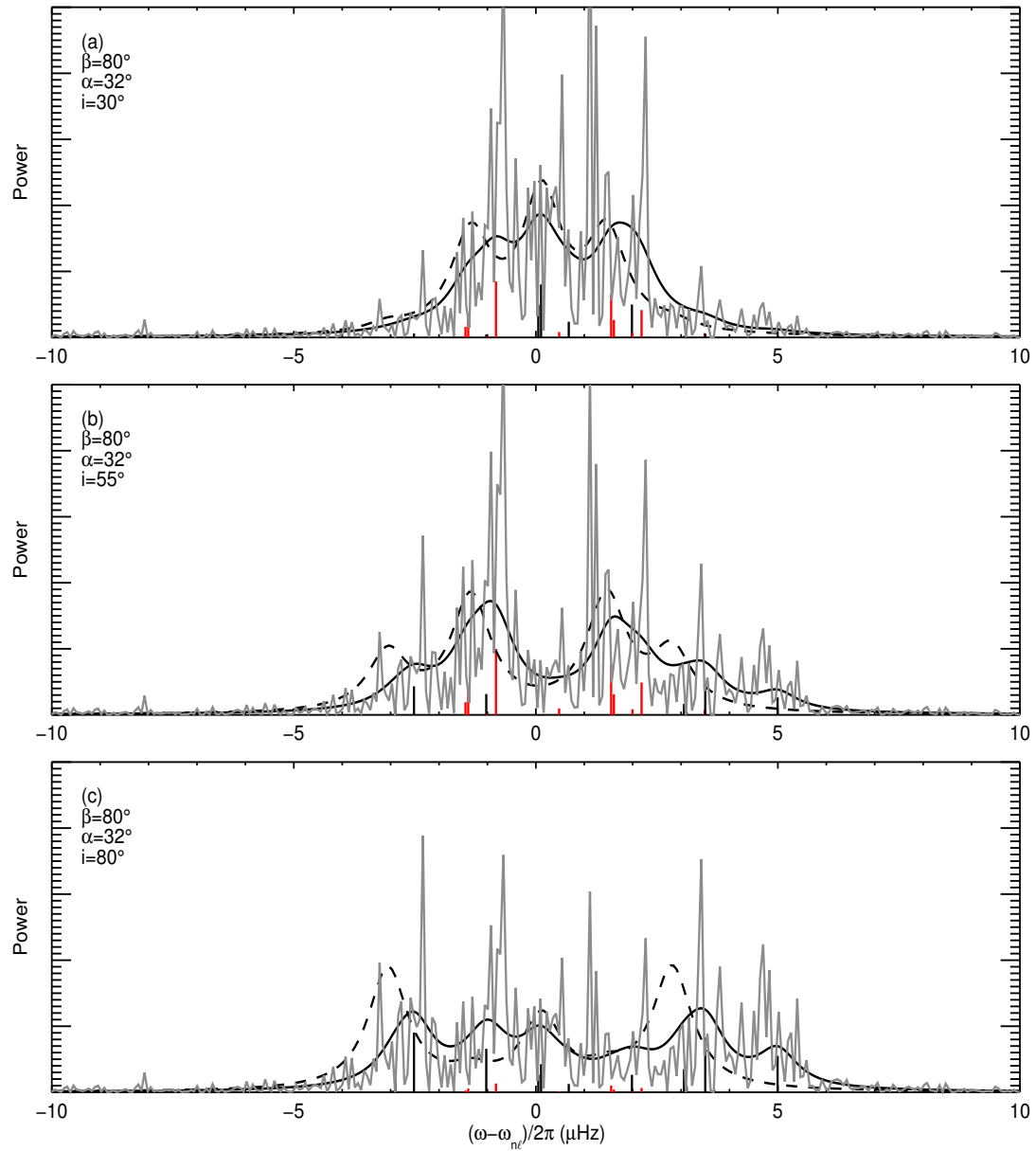


Figure 4.13: Same as in Figure 4.11, but for an AR colatitude $\beta = 80^\circ$.

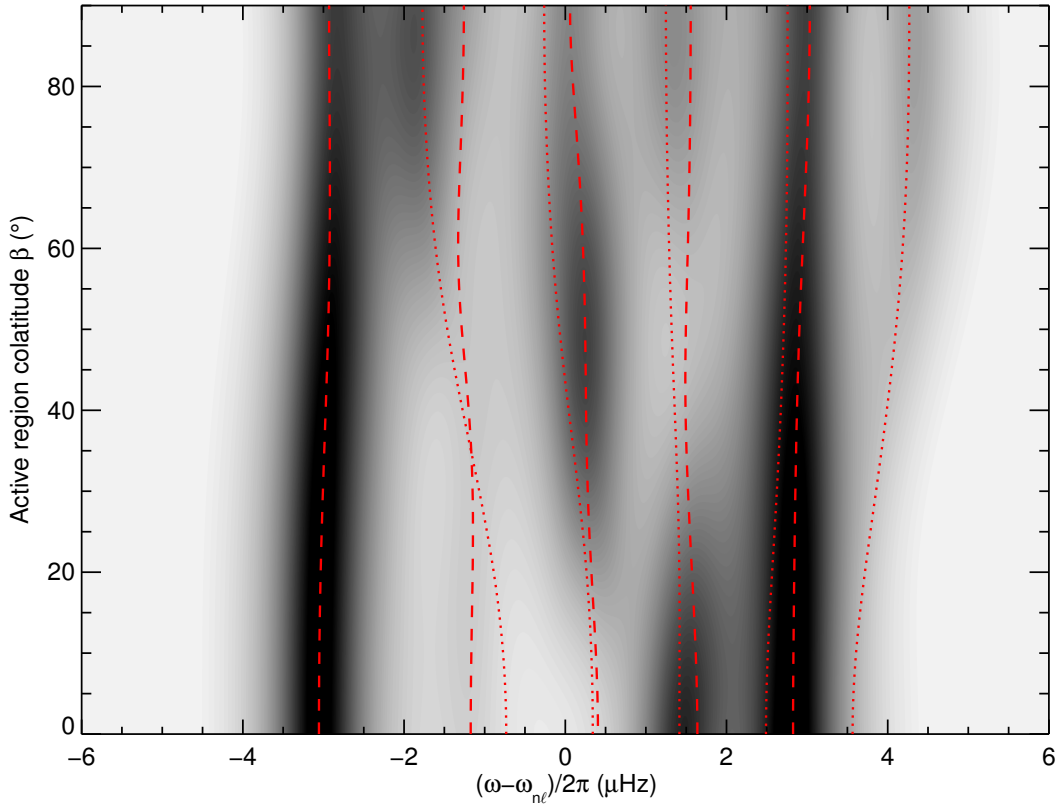


Figure 4.14: Contour of the acoustic power as a function of the active region colatitude β , for the $\ell = 2$, $n = 18$ multiplet and for $\varepsilon_{n\ell} = 0.003$, $\alpha = 23^\circ$, and $i = 80^\circ$. The red lines show the power-weighted averages of the frequency shifts for $M \neq 0$ in each m -quintuplet (dashed lines) and the shift of the $M = 0$ peaks (dotted lines).

which completely overlap. Gray lines show the same averaging but for a pure rotational multiplet, which results in a constant offset due to centrifugal distortion.

4.3 Nonlinear frequency shifts and amplitudes in synthetic power spectra from numerical simulations

We now explore the nonlinear regime of the AR perturbation by means of numerical simulations in the time domain. For the study we used the GLASS code with the same numerical setup employed in Papini et al. (2015).

Running numerical simulations for different values of β and different perturbation amplitudes is computationally expensive. Instead we performed simulations for a 3D polar perturbation to the sound speed in the case of a star with no rotation (this is equivalent to solve the numerical problem in the reference frame $\tilde{\mathcal{R}}_\beta$), and we introduced the effect of rotation later in processing the output. The approach has the advantage that, for a given amplitude of the AR perturbation, we only need to run one simulation in order to calculate the power spectrum for any given value of β and rotation period. However

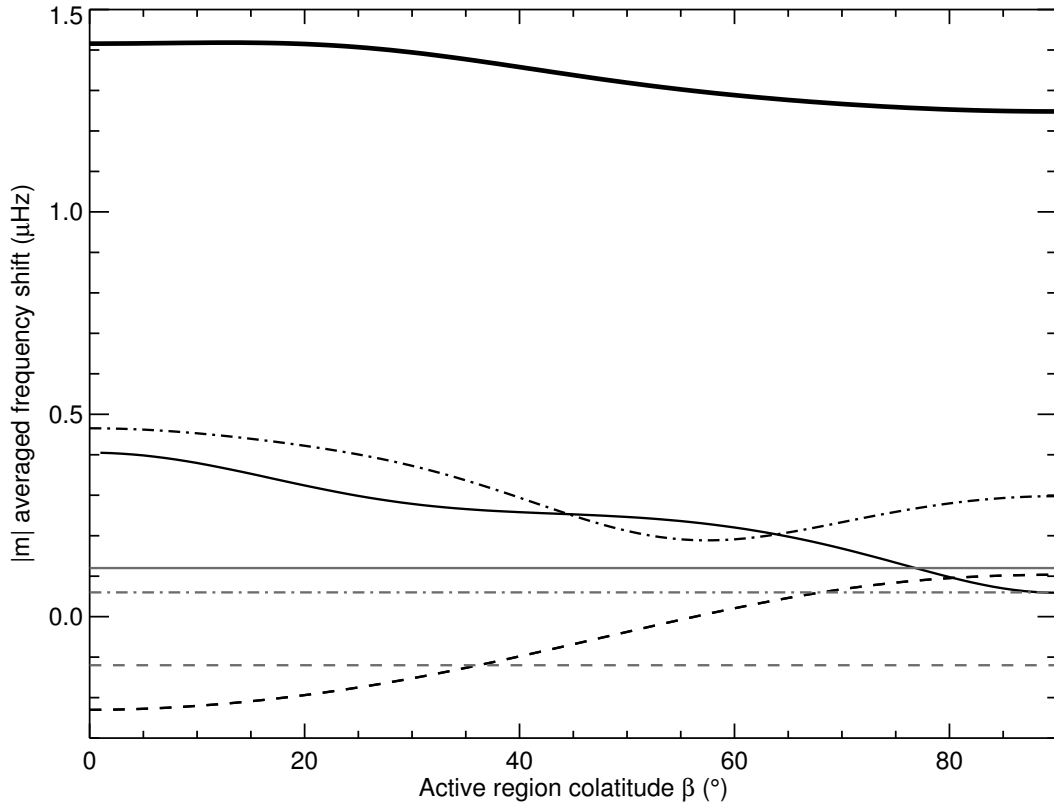


Figure 4.15: Averaged frequency shifts induced by the active region vs. active region colatitude β , for the $\ell = 2$, $n = 18$ multiplet and for $\varepsilon_{n\ell} = 0.003$ and $\alpha = 23^\circ$. The shifts are averaged for each m over the 2ℓ peaks with $M \neq 0$, and then averaged over the same $|m|$ to remove the effect of rotation, except the centrifugal distortion. The black solid line is for $m = 0$, the dash-dotted line is for $|m| = 1$, and the dashed line is for $|m| = 2$. Gray lines result from the effect of the centrifugal distortion only. The black solid thick line at the top indicate the shift of the $M = 0, m = 0$ peak.

we can only reproduce solid body rotation, and it is not possible to include the effects of centrifugal distortion and of the Coriolis force, therefore in each $n\ell$ -multiplet we expect to find $(2\ell + 1)(\ell + 1)$ peaks instead of $(2\ell + 1)^2$. Nonetheless the results are useful for exploring the nonlinear regime of the AR perturbation. We note that, as a consequence of neglecting these rotational effects, M identifies the azimuthal degree of the spherical harmonics $Y_\ell^M(\tilde{\theta}, \tilde{\phi})$ in the frame $\tilde{\mathcal{R}}_\beta$ (see Section 4.2.1).

We considered a 3D perturbation to the square sound speed of the form (see Equation 3.7)

$$\Delta c^2(r, \tilde{\theta}) = \varepsilon c_0^2(r) f(r; r_c) g(\tilde{\theta}), \quad (4.30)$$

that in $\tilde{\mathcal{R}}_\beta$ describes a perturbation of amplitude ε^1 placed at a depth $R - r_c$, with a Gaussian profile in radius multiplied by a raised cosine $f(r; r_c)$ and with a raised cosine profile $g(\tilde{\theta})$ in colatitude. For the explicit form of $f(r; r_c)$ and $g(\tilde{\theta})$, and for other details concerning the simulation setup we refer to Papini et al. (2015). As $g(\tilde{\theta})$ is defined, the perturbation

¹N.B.: the ε defined here is not the $\varepsilon_{n\ell}$ introduced in Equation (4.15).

is placed at the pole.

4.3.1 Synthetic power spectrum with rotation

Building a synthetic power spectrum in principle requires calculating all the contributions to the intensity at the photosphere in the visible part of the electromagnetic spectrum. Here we are only concerned with the contributions of the acoustic wavefield. As in Section 4.2.1.3 we assume that the intensity fluctuations are proportional to the Eulerian pressure perturbation measured at $r_0 = R + 200$ km above the surface (see Papini et al. 2015).

In the simulations all the modes were excited at the beginning with the same phase, therefore in order to recover the limit power spectrum in the case of stochastic excitation we employed the following procedure. The contribution to the intensity $I_M(\tilde{\theta}, \tilde{\phi}, t)$ of all the different $n\ell$ modes with the same M takes the form

$$I_M(\tilde{\theta}, \tilde{\phi}, t) \propto \sum_{\ell=|M|}^{\ell_{\max}} \Re \left\{ p_{\ell M}(r_0, t) Y_{\ell}^M(\tilde{\theta}, \tilde{\phi}) \right\}, \quad (4.31)$$

where $p_{\ell M}(r_0, t)$ are the coefficients of the spherical harmonic decomposition of the wavefield pressure $p(r_0, \tilde{\theta}, \tilde{\phi}, t)$ at the time t in the frame $\tilde{\mathcal{R}}_{\beta}$, given in output by GLASS, and ℓ_{\max} gives the spectral resolution of the spherical harmonic decomposition. By using Equation (4.12) we expressed each $Y_{\ell}^M(\tilde{\theta}, \tilde{\phi})$ in terms of the spherical harmonics $Y_{\ell}^m(\theta, \phi)$ in the frame \mathcal{R} , by means of two consecutive rotations of the Euler angles $(0, -i, \Omega_{\beta}t)$ and $(0, \beta, 0)$. This was followed by an integration over the visible disk, to obtain the disk-integrated intensity of each mM component

$$I_{mM}(t) = \sum_{\ell=\max\{|m|, |M|\}}^{\ell_{\max}} V_{\ell} r_{0m}^{(\ell)} (-i) r_{mM}^{(\ell)}(\beta) \Re \left\{ p_{\ell M}(r_0, t) e^{-im\Omega_{\beta}t} \right\}. \quad (4.32)$$

Then a Fourier transform in time was performed, in order to obtain the observed intensity $I_{mM}(\omega)$ in the frequency domain. Finally we derived the expression for the limit power spectrum in the case of random excitations

$$\mathcal{P}(\omega) = \sum_{m=-\ell_{\max}}^{\ell_{\max}} \sum_{M=-\ell_{\max}}^{\ell_{\max}} |I_{mM}(\omega)|^2, \quad (4.33)$$

that is analogous to Equation (4.26), but for the entire wavefield.

For the nonlinear study we chosen a perturbation with $r_c = 0.98$ and $\epsilon = 0.1$, which for $\ell = 2, n = 18$ results in a value $\epsilon_{n\ell} \simeq 0.005$, that is, roughly twice the value used in the linear analysis. The simulation run for 108 days (stellar time), in order to reach an accuracy of $\sim 0.11 \mu\text{Hz}$ in the frequency domain. In the simulations the wavefield is affected by a numerical damping, that grows with frequency with an exponential dependence. This caused the peaks in the simulated spectra to have a Lorentzian shape. We took advantage of numerical damping and for the analysis we selected two $\ell = 2$ multiplets: one with $n = 18$ and a FWHM comparable to that observed in the Sun, the other with $n = 12$ and a FWHM small enough to resolve all the mM peaks in the multiplet and thus better characterize the nonlinear effects.

Figures 4.16 and 4.17 show the observed power spectra of the two selected multiplets, in the case of $\beta = 80^\circ$ and two inclination angles, $i = 30^\circ$ and 80° . The peaks of the $n = 12$ multiplet have a FWHM of $\Gamma/2\pi \simeq 0.2 \mu\text{Hz}$, small enough to separate almost all the 15 peaks, while the peaks of the $n = 18$ multiplet have $\Gamma/2\pi \simeq 1 \mu\text{Hz}$, and only few peaks are well resolved. Each spectrum is normalized with respect to the uppermost $M \neq 0$ peak. The simulated power spectrum (black line) of the $\ell = 2, n = 12$ multiplet is well reproduced by the spectrum predicted by the linear theory (red dot-dashed lines), except for the peaks corresponding to the $M = 0$ mode (vertical red lines show the $M = 0$ peaks from linear theory), which are less shifted in frequency and have smaller amplitudes. In the case of the $\ell = 2, n = 18$ multiplet the nonlinear effects are less visible, due to the overlapping of the Lorentzian profiles. To help the discussion a blue line displays the contribution to the power spectrum of the $M = 0$ peaks, and shows that also for this multiplet the $M = 0$ component of the spectrum deviates from the linear behavior, both in frequency and amplitude (the Lorentzian envelopes drawn by the blue line are incompatible with amplitudes and frequencies defined by the vertical red lines). With increasing ϵ the wavefield-AR interaction enters in the strongly nonlinear regime, and for a perturbation with $\epsilon = 0.4$ results in a massive distortion of the multiplet's power spectrum, with respect to the spectrum predicted by linear theory (see Figure 4.18 and 4.19). The distortion is mainly caused by the increasing mixing of the modes (see Section 3.5.1).

Here two different behaviors are evident. In the $\ell = 2, n = 12$ multiplet the $M = 0$ peaks are almost suppressed, while the same peaks for the $\ell = 2, n = 18$ are strongly enhanced. Also the peaks with $M = 1$ start to deviate from the linear prediction. This is in agreement with what found in Papini et al. (2015) for the nonrotating case.

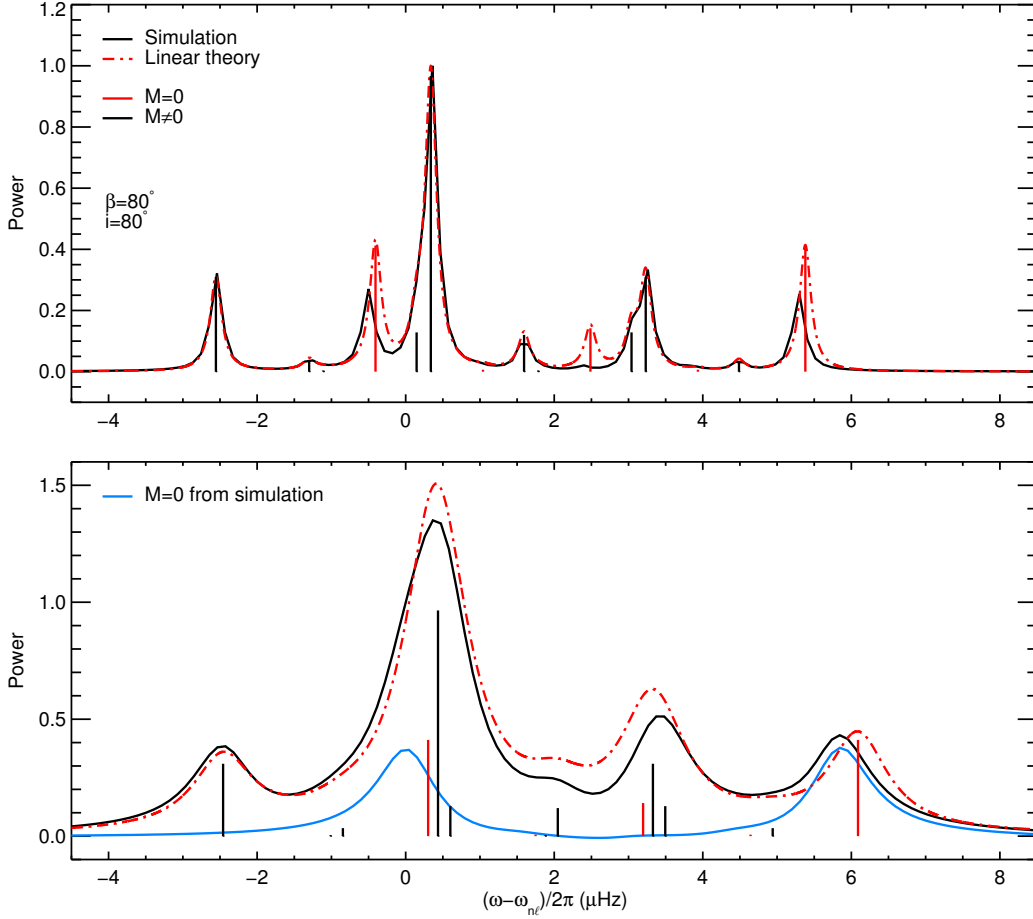


Figure 4.16: Acoustic power vs. frequency $(\omega - \omega_{nl})/2\pi$ for the $\ell = 2$, $n = 12$ (top panel) and $n = 18$ (bottom panel) multiplets, as observed at an inclination angle $i = 80^\circ$ for a star with a rotation period of 8 days (solid body rotation) and $\beta = 80^\circ$, and for a perturbation with $\epsilon = 0.1$ and $r_c = 0.98$ (Equation (4.30)). The black line shows the power spectrum extracted from a simulation performed with GLASS, the red dot-dashed line indicates the theoretical spectrum as resulting from linear theory. Vertical lines show the theoretical peaks from linear theory, in red for $M = 0$ and in black for $M \neq 0$. The blue line displays the contribution of the $M = 0$ peaks to the simulated power spectrum. The $n = 12$ multiplet has a FWHM of $\Gamma/2\pi \approx 0.2 \mu\text{Hz}$, while the $n = 18$ multiplet has $\Gamma/2\pi \approx 1 \mu\text{Hz}$.

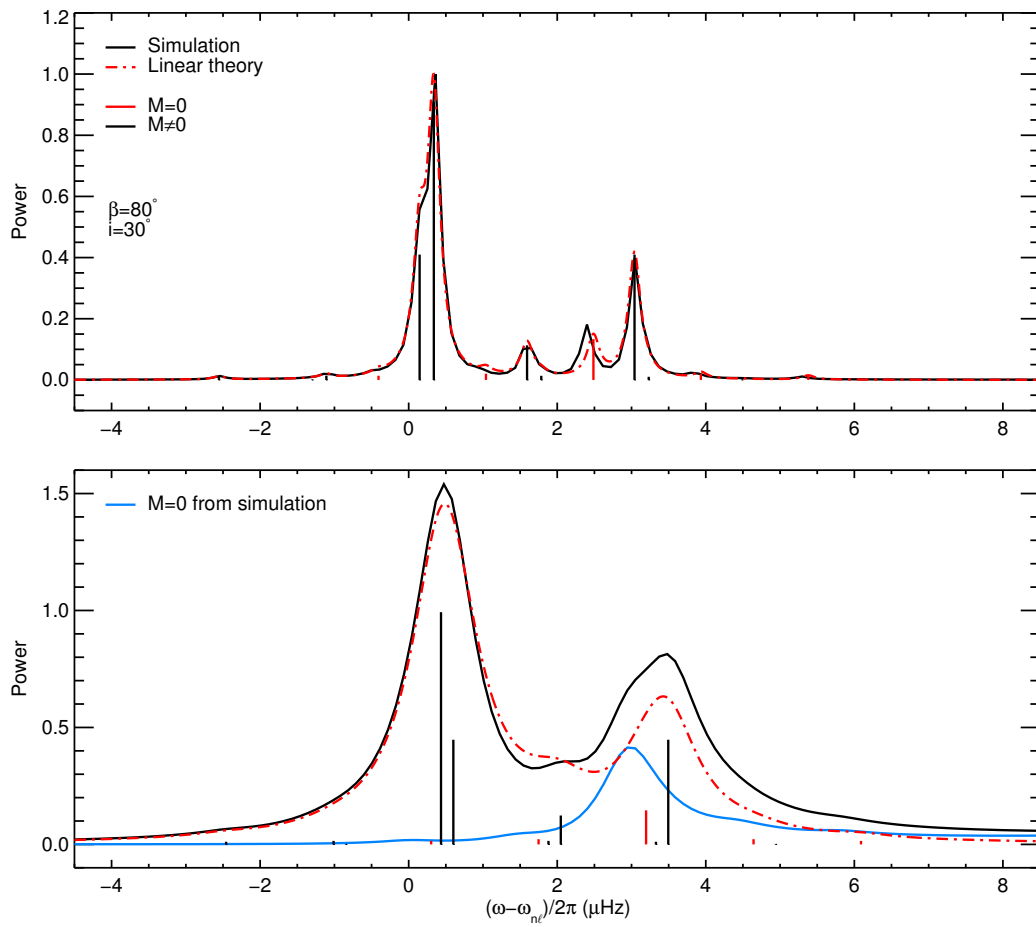


Figure 4.17: Same as in Figure 4.16, but for $i = 30^\circ$.

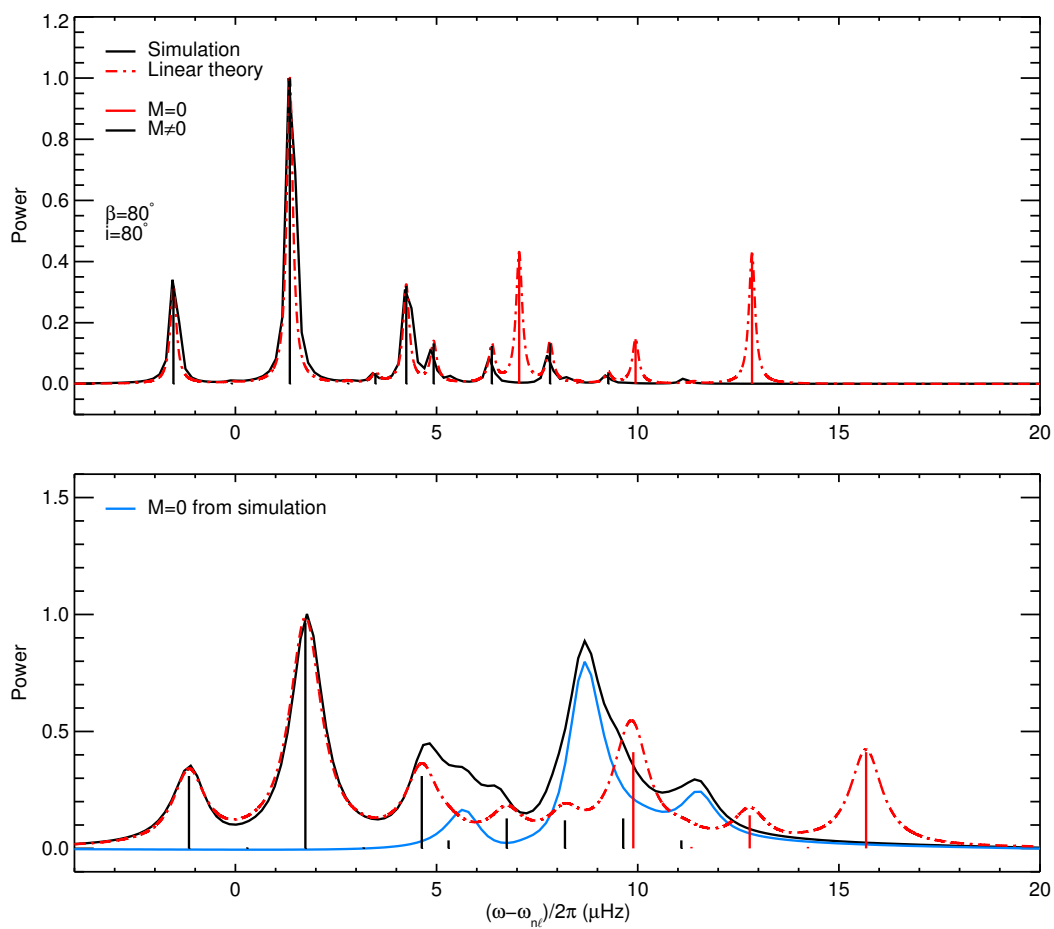


Figure 4.18: Same as in Figure 4.16, but for $\epsilon = 0.4$.

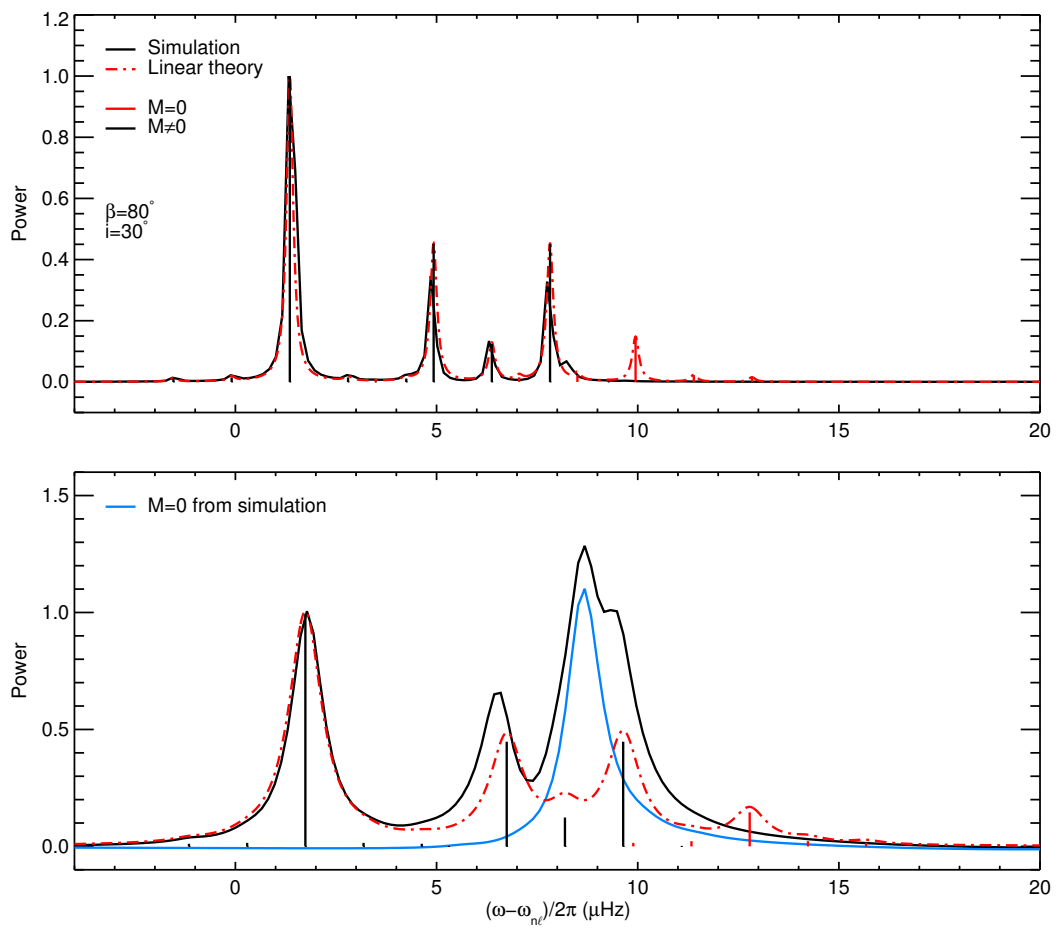


Figure 4.19: Same as in Figure 4.16, but for $\epsilon = 0.4$ and $i = 30^\circ$.

5 Conclusions

In this thesis I used forward modeling to investigate the interaction of global acoustic modes of oscillation with localized structures. This study should help identify the signature of starspots and active regions in asteroseismic observations.

5.1 Conclusions of chapter 2

The use of a numerical code to perform linear time domain simulations required the construction of a stellar background model which is convectively stable. The stabilization method devised offers several advantages, as it completely removes the convective instability and it is not tuned to a particular model, but can be applied to any stellar model. Moreover, important properties of the original model (such as hydrostatic equilibrium and seismic reciprocity, if present) are preserved.

Connected to the problem of stabilization, a perturbative approach was proposed to approximately recover the wavefield of the original unstable model, by using linear time-domain numerical simulations.

The method requires the relative change ΔN in the buoyancy frequency between the stable and the unstable model to be $\Delta N^2/2\omega^2 \lesssim 1$, where ω is the wave angular frequency. Whether this condition is fulfilled depends on the model of convection used. In this work we used the standard solar Model S, which is based on a mixing-length theory (MLT) of convection (by setting $\alpha_P = 1.990$, see Christensen-Dalsgaard 2008b, Appendix 2 and references therein), such that $\Delta N^2/2\omega^2 < 1.1$ at $\omega/2\pi = 3$ mHz in the highly superadiabatic layer. Model S does not include the treatment for turbulent pressure.

Other models of convection (including turbulent pressure, MLT with different mixing-length parameters, nonlocal MLT, models from 3D simulations) may result in different superadiabatic gradients (as shown by, *e.g.* Trampedach 2010, Figure 4), leading to either higher or lower values of $\Delta N^2/2\omega^2$. In addition, the peak in the superadiabatic gradient strongly depends on the Sun-like star under consideration which, for increasing values of $\log g$, shows a decreasing amplitude and an increasing width of the superadiabatic peak (see Trampedach 2010, Figure 2).

Because we are ultimately interested in running 3D simulations of wave propagation in the presence of magnetic activity, it is important to ask about the influence of magnetic fields on superadiabatic gradients in the near surface layers. For that purpose, we measured N^2 in the realistic 3D sunspot simulation of Braun et al. (2012). It follows, using the condition for convective instability in the presence of vertical magnetic fields (Gough

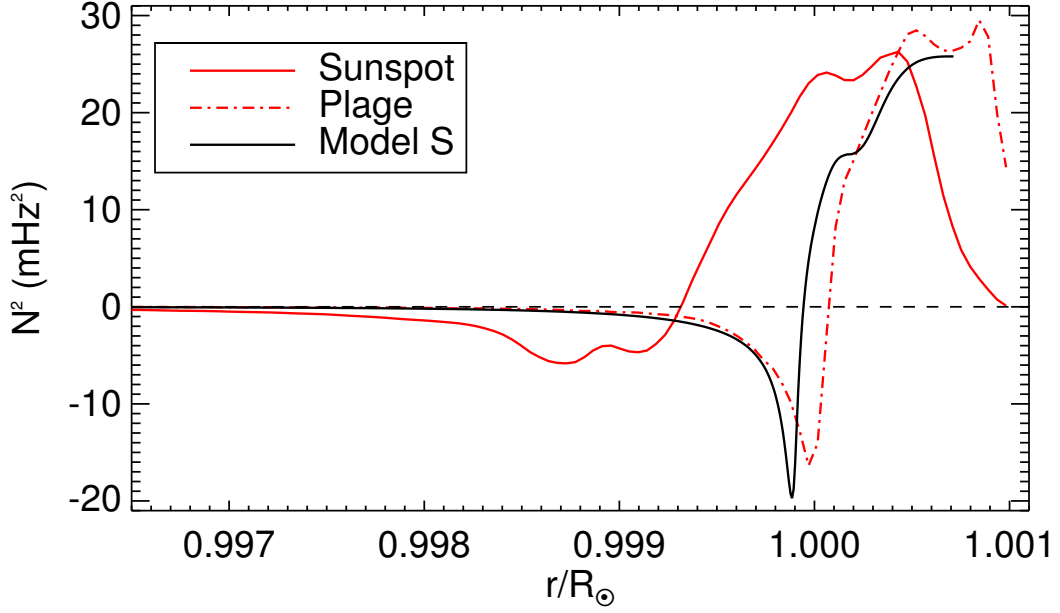


Figure 5.1: Square of the buoyancy frequency in presence of a sunspot, from the simulations of Braun et al. (2012): in the umbra (red line) (circular average on the first 2 Mm from the center of the spot), in the plage (red dot dashed line) and from Model S (black line).

and Tayler 1966)

$$\frac{1}{\Gamma} - \frac{d \ln \rho}{d \ln P} < \left(1 + \frac{4\pi\Gamma P}{B^2} \right)^{-1},$$

that the magnetic field B has a stabilizing effect. Therefore it is likely that enforcing $N^2 > 0$ in the quiet Sun is a sufficient condition for stability in the presence of magnetic activity.

Figure 5.1 shows that the value of ΔN^2 in the sunspot (where the magnetic-field amplitude exceeds 3000 G) is reduced by a factor of about four. In plage regions (with a magnetic-field amplitude $B \approx 100$ G, at a distance of 20 Mm from the center of the sunspot), ΔN^2 is only slightly reduced (Figure 5.1).

While more tests are needed, we expect that the proposed approach for performing time-domain simulations of wave propagation will find applications both in local and global helioseismology.

5.2 Conclusions of chapter 3

Using 3D linear numerical simulations, I investigated the changes in global acoustic modes with $\ell \leq 2$ induced by a localized sound speed perturbation at a depth $R - r_c$ and with relative amplitude ϵ , mimicking the changes caused by a starspot with a polar cap configuration. The effect of rotation was not included. A parametric study considering different values for r_c and ϵ was performed.

Results have shown that the interaction of the wavefield with a polar spot strongly affects the axisymmetric modes, which show a nonlinear behavior increasing with ϵ , for $\epsilon \gtrsim 0.2$. The frequency shifts for radial modes exceed the shifts predicted by linear theory, while the shifts for the $\ell = 2, m = 0$ modes are smaller than predicted by linear theory and cross the $|m| = 1$ modes at a frequency that decreases with increasing ϵ or decreasing depth. For modes with $m \neq 0$ linear theory successfully predicts the correct frequencies, however, the $m = 1$ modes start to deviate from the linear regime at $\epsilon \simeq 0.8$.

The nonlinear changes, with ϵ , in the mode frequencies and mode mixing (resulting from the distortion of eigenfunctions) will play a role in the correct identification of the modes. Strong mode mixing may also cause $\ell > 2$ modes to become visible in the observed spectrum (see, *e.g.*, Dziembowski and Goode 1996).

In this context, a global comparison of the frequency shifts in all $n\ell$ -components (as done, *e.g.* in Figure 3.4) would help in the correct identification of the modes and in exploiting the nonlinear behavior of the axisymmetric modes, thus characterizing the perturbation.

5.3 Conclusions of chapter 4

In this chapter stellar rotation was introduced and a localized perturbation describing a corotating active region was placed at different latitudes. In such a system, the perturbation is unsteady in any inertial frame of reference. The active region is characterized by its surface coverage and a perturbation amplitude $\epsilon_{n\ell}$. We considered surface coverages of 4% and 8% of the stellar surface, in the range of observed values (Strassmeier 2009).

In the linear regime of the perturbation, the power spectrum of the low-degree modes revealed a complex structure: the combined effects of rotation and the active-region perturbation cause each $n\ell$ -multiplet to appear as $(2\ell + 1)^2$ peaks, each of them with a different amplitude (Goode and Thompson 1992; Gizon 1998). Among these, $2\ell(2\ell + 1)$ peaks are clustered near the frequencies of pure rotational splitting, while the other $2\ell + 1$ peaks are shifted to higher frequencies. As a consequence, the power spectrum develops a complex and asymmetric profile and shows more than the standard $2\ell + 1$ peaks in a multiplet.

The number of resolved peaks in the observed spectrum is sensitive to the latitudinal position of the active region and to the inclination angle i . The inclination angle plays a major role in shaping the multiplet, as it determines the visibility of the modes. We find that the complexity of the power spectrum increases with the colatitude β of the active region, due to the increasing amplitude of the nondiagonal elements in the perturbation matrix. For fast rotating stars, the effect of centrifugal distortion is significant and must be accounted for, since it also introduces a m -symmetric component to the frequency splittings.

Numerical simulations, performed to explore the nonlinear regime of the perturbation, have shown that the $M = 0$ peaks deviate from the linear behavior for $\varepsilon_{n\ell} \gtrsim 0.005$. Depending on the $n\ell$ -multiplet in the power spectrum, the amplitude of these peaks is either reduced or enhanced, due to mode mixing (Section 3.5.1). These results suggest that for active regions of sizes comparable to the largest ones observed with Doppler imaging (Marsden et al. 2005), the calculations should be carried out in the nonlinear regime.

5.4 Outlook

In this thesis we have studied the observational signatures of a large starspot or an active region in the power spectrum of low-degree acoustic oscillations. We discussed the complex appearance of mode power in azimuthal mode multiplets due to the unsteady nature of the perturbation. Numerical simulations with GLASS could be used to identify modes in strongly magnetized stars. Future work may include more realistic models of starspots and active regions, which account for the direct magnetohydrodynamic (MHD) effect of magnetic fields on the acoustic wavefield (*e.g.*, Cameron et al. 2011).

Guided by the simulations presented in this thesis, future work should include the search for the seismic signature of starspots in oscillation power spectra from the *Kepler* mission. The search for asymmetric line profiles requires power spectra with high signal-to-noise ratios from stars with large starspots. It may be possible to detect the asteroseismic signature of starspots in Sun-like pulsators from the *Kepler* catalog that are more active than the Sun. The PLATO mission (Rauer et al. 2014), to be launched in 2024, will provide a very large database of pulsating stars and a great opportunity to study stellar activity through asteroseismology.

Bibliography

- Aerts, C., Christensen-Dalsgaard, J., Kurtz, D. W., 2010, *Asteroseismology*, Springer
- Anderson, E. R., Duvall, Jr., T. L., Jefferies, S. M., 1990, *Modeling of solar oscillation power spectra*, *ApJ*, **364**, 699–705
- Auvergne, M., Bodin, P., Boisdard, L., Buey, J.-T., Chaintreuil, S., Epstein, G., Joutet, M., Lam-Trong, T., Levacher, P., Magnan, A., Perez, R., Plasson, P., Plesseria, J., Peter, G., Steller, M., Tiphène, D., Baglin, A., Agogué, P., Appourchaux, T., Barbet, D., Beaufort, T., Bellenger, R., Berlin, R., Bernardi, P., Blouin, D., Boumier, P., Bonneau, F., Briet, R., Butler, B., Cautain, R., Chiavassa, F., Costes, V., Cuvilho, J., Cunha-Parro, V., de Oliveira Fialho, F., Decaudin, M., Defise, J.-M., Djalal, S., Docclo, A., Drummond, R., Dupuis, O., Exil, G., Fauré, C., Gaboriaud, A., Gamet, P., Gavalda, P., Grolleau, E., Gueguen, L., Guivarc’h, V., Guterman, P., Hasiba, J., Huntzinger, G., Hustaix, H., Imbert, C., Jeanville, G., Johlander, B., Jorda, L., Journoud, P., Karioty, F., Kerjean, L., Lafond, L., Lapeyrere, V., Landiech, P., Larqué, T., Laudet, P., Le Merrer, J., Leporati, L., Leruyet, B., Levieuge, B., Llebaria, A., Martin, L., Mazy, E., Mesnager, J.-M., Michel, J.-P., Moalic, J.-P., Monjoin, W., Naudet, D., Neukirchner, S., Nguyen-Kim, K., Ollivier, M., Orcesi, J.-L., Ottacher, H., Oulali, A., Parisot, J., Perruchot, S., Piacentino, A., Pinheiro da Silva, L., Platzer, J., Pontet, B., Pradines, A., Quentin, C., Rohbeck, U., Rolland, G., Rollenhagen, F., Romagnan, R., Russ, N., Samadi, R., Schmidt, R., Schwartz, N., Sebbag, I., Smit, H., Sunter, W., Tello, M., Toulouse, P., Ulmer, B., Vandermarcq, O., Vergnault, E., Wallner, R., Waultier, G., Zanatta, P., 2009, *The CoRoT satellite in flight: description and performance*, *A&A*, **506**, 411–424
- Baliunas, S. L., Donahue, R. A., Soon, W. H., Horne, J. H., Frazer, J., Woodard-Eklund, L., Bradford, M., Rao, L. M., Wilson, O. C., Zhang, Q., Bennett, W., Briggs, J., Carroll, S. M., Duncan, D. K., Figueroa, D., Lanning, H. H., Misch, T., Mueller, J., Noyes, R. W., Poppe, D., Porter, A. C., Robinson, C. R., Russell, J., Shelton, J. C., Soyumer, T., Vaughan, A. H., Whitney, J. H., 1995, *Chromospheric variations in main-sequence stars*, *ApJ*, **438**, 269–287
- Bedding, T. R., 2014, *Solar-like oscillations: An observational perspective*, 22nd Canary Islands Winter School of Astrophysics, (eds.) P. L. Pallé and C. Esteban, Cambridge University Press
- Böhm-Vitense, E., 2007, *Chromospheric Activity in G and K Main-Sequence Stars, and What It Tells Us about Stellar Dynamos*, *ApJ*, **657**, 486–493

- Borucki, W. J., Koch, D., Basri, G., Batalha, N., Brown, T., Caldwell, D., Caldwell, J., Christensen-Dalsgaard, J., Cochran, W. D., DeVore, E., Dunham, E. W., Dupree, A. K., Gautier, T. N., Geary, J. C., Gilliland, R., Gould, A., Howell, S. B., Jenkins, J. M., Kondo, Y., Latham, D. W., Marcy, G. W., Meibom, S., Kjeldsen, H., Lissauer, J. J., Monet, D. G., Morrison, D., Sasselov, D., Tarter, J., Boss, A., Brownlee, D., Owen, T., Buzasi, D., Charbonneau, D., Doyle, L., Fortney, J., Ford, E. B., Holman, M. J., Seager, S., Steffen, J. H., Welsh, W. F., Rowe, J., Anderson, H., Buchhave, L., Ciardi, D., Walkowicz, L., Sherry, W., Horch, E., Isaacson, H., Everett, M. E., Fischer, D., Torres, G., Johnson, J. A., Endl, M., MacQueen, P., Bryson, S. T., Dotson, J., Haas, M., Kolodziejczak, J., Van Cleve, J., Chandrasekaran, H., Twicken, J. D., Quintana, E. V., Clarke, B. D., Allen, C., Li, J., Wu, H., Tenenbaum, P., Verner, E., Bruhweiler, F., Barnes, J., Prsa, A., 2010, *Kepler Planet-Detection Mission: Introduction and First Results*, *Science*, **327**, 977–980
- Braun, D. C., Birch, A. C., Rempel, M., Duvall, T. L., 2012, *Helioseismology of a Realistic Magnetoconvective Sunspot Simulation*, *ApJ*, **744**, 77
- Broomhall, A.-M., Chatterjee, P., Howe, R., Norton, A. A., Thompson, M. J., 2014, *The Sun's Interior Structure and Dynamics, and the Solar Cycle*, *Space Sci. Rev.*, **186**, 191–225
- Cameron, R., Gizon, L., Daifallah, K., 2007, *SLiM: a code for the simulation of wave propagation through an inhomogeneous, magnetised solar atmosphere*, *Astronom. Nach.*, **328**, 313–318
- Cameron, R., Gizon, L., Duvall, Jr., T. L., 2008, *Helioseismology of Sunspots: Confronting Observations with Three-Dimensional MHD Simulations of Wave Propagation*, *Sol. Phys.*, **251**, 291–308
- Cameron, R. H., Gizon, L., Schunker, H., Pietarila, A., 2011, *Constructing Semi-Empirical Sunspot Models for Helioseismology*, *Sol. Phys.*, **268**, 293–308
- Chaplin, W. J., Elsworth, Y., Isaak, G. R., Marchenkov, K. I., Miller, B. A., New, R., Pinter, B., Appourchaux, T., 2002, *Peak finding at low signal-to-noise ratio: low- l solar acoustic eigenmodes at $n \leq 9$ from the analysis of BiSON data*, *MNRAS*, **336**, 979–991
- Chaplin, W. J., Houdek, G., Elsworth, Y., Gough, D. O., Isaak, G. R., New, R., 2005, *On model predictions of the power spectral density of radial solar p modes*, *MNRAS*, **360**, 859–868
- Chaplin, W. J., Elsworth, Y., Houdek, G., New, R., 2007a, *On prospects for sounding activity cycles of Sun-like stars with acoustic modes*, *MNRAS*, **377**, 17–29
- Chaplin, W. J., Elsworth, Y., Miller, B. A., Verner, G. A., New, R., 2007b, *Solar p -Mode Frequencies over Three Solar Cycles*, *ApJ*, **659**, 1749–1760
- Chaplin, W. J., Houdek, G., Appourchaux, T., Elsworth, Y., New, R., Toutain, T., 2008, *Challenges for asteroseismic analysis of Sun-like stars*, *A&A*, **485**, 813–822

- Christensen-Dalsgaard, J., 2002, *Helioseismology*, *Reviews of Modern Physics*, **74**, 1073–1129
- Christensen-Dalsgaard, J., 2004, *An Overview of Helio- and Asteroseismology*, in SOHO 14 Helio- and Asteroseismology: Towards a Golden Future, (Ed.) D. Danesy, vol. **559** of ESA Special Publication, pp. 1–33
- Christensen-Dalsgaard, J., 2008a, *ADIPLS – the Aarhus adiabatic oscillation package*, *Ap&SS*, **316**, 113–120
- Christensen-Dalsgaard, J., 2008b, *ASTEC– the Aarhus STellar Evolution Code*, *Ap&SS*, **316**, 13–24
- Christensen-Dalsgaard, J., Dappen, W., Ajukov, S. V., Anderson, E. R., Antia, H. M., Basu, S., Baturin, V. A., Berthomieu, G., Chaboyer, B., Chitre, S. M., Cox, A. N., Demarque, P., Donatowicz, J., Dziembowski, W. A., Gabriel, M., Gough, D. O., Guenther, D. B., Guzik, J. A., Harvey, J. W., Hill, F., Houdek, G., Iglesias, C. A., Kosovichev, A. G., Leibacher, J. W., Morel, P., Proffitt, C. R., Provost, J., Reiter, J., Rhodes, Jr., E. J., Rogers, F. J., Roxburgh, I. W., Thompson, M. J., Ulrich, R. K., 1996, *The Current State of Solar Modeling*, *Science*, **272**, 1286–1292
- Cowling, T. G., 1941, *The non-radial oscillations of polytropic stars*, *MNRAS*, **101**, 367–375
- Cunha, M. S., Gough, D., 2000, *Magnetic perturbations to the acoustic modes of roAp stars*, *MNRAS*, **319**, 1020–1038
- Dahlen, F. A., Tromp, J., 1998, *Theoretical global seismology*, Princeton University Press, Princeton
- Dziembowski, W. A., Goode, P. R., 1992, *Effects of differential rotation on stellar oscillations - A second-order theory*, *ApJ*, **394**, 670–687
- Dziembowski, W. A., Goode, P. R., 1996, *Magnetic Effects on Oscillations in roAp Stars*, *ApJ*, **458**, 338–346
- García, R. A., Mathur, S., Salabert, D., Ballot, J., Régulo, C., Metcalfe, T. S., Baglin, A., 2010, *CoRoT Reveals a Magnetic Activity Cycle in a Sun-Like Star*, *Science*, **329**, 1032
- Gizon, L., 1995, *Can we see the back of the Sun?*, in Vincent R.A. et al. (eds.), *Proc. Conf. STEP 1995* (University of Adelaide), pp. 173–176
- Gizon, L., 1998, *Comments on the influence of solar activity on p-mode oscillation spectra*, in *New Eyes to See Inside the Sun and Stars*, (Eds.) F.-L. Deubner, J. Christensen-Dalsgaard, D. Kurtz, vol. **185** of IAU Symposium, pp. 173–174
- Gizon, L., 2002, *Prospects for detecting stellar activity through asteroseismology*, *Astronomische Nachrichten*, **323**, 251–253
- Gizon, L., 2013, *Seismology of the Sun*, in *Proc. 11th Internat. Conf. on Mathematical and Numerical Aspects of Waves*, (Eds.) N. Gmati, H. Haddar, pp. 23–26

- Gizon, L., Solanki, S. K., 2003, *Determining the Inclination of the Rotation Axis of a Sun-like Star*, ApJ, **589**, 1009–1019
- Gizon, L., Solanki, S. K., 2004, *Measuring Stellar Differential rotation with asteroseismology*, Sol. Phys., **220**, 169–184
- Gizon, L., Birch, A. C., Spruit, H. C., 2010, *Local Helioseismology: Three-Dimensional Imaging of the Solar Interior*, Ann. Rev. Astron. Astrophys., **48**, 289–338
- Goode, P. R., Thompson, M. J., 1992, *The effect of an inclined magnetic field on solar oscillation frequencies*, ApJ, **395**, 307–315
- Gough, D. O., Tayler, R. J., 1966, *The influence of a magnetic field on Schwarzschild's criterion for convective instability in an ideally conducting fluid*, MNRAS, **133**, 85–98
- Gough, D. O., Thompson, M. J., 1990, *The effect of rotation and a buried magnetic field on stellar oscillations*, MNRAS, **242**, 25–55
- Gough, D. O., Kosovichev, A. G., Toomre, J., Anderson, E., Antia, H. M., Basu, S., Chaboyer, B., Chitre, S. M., Christensen-Dalsgaard, J., Dziembowski, W. A., Eff-Darwich, A., Elliott, J. R., Giles, P. M., Goode, P. R., Guzik, J. A., Harvey, J. W., Hill, F., Leibacher, J. W., Monteiro, M. J. P. F. G., Richard, O., Sekii, T., Shibahashi, H., Takata, M., Thompson, M. J., Vauclair, S., Vorontsov, S. V., 1996, *The Seismic Structure of the Sun*, Science, **272**, 1296–1300
- Hanasoge, S. M., 2008, *Seismic Halos around Active Regions: A Magnetohydrodynamic Theory*, ApJ, **680**, 1457–1466
- Hanasoge, S. M., Duvall, Jr., T. L., 2007, *The solar acoustic simulator: applications and results*, Astronom. Nach., **328**, 319–322
- Hanasoge, S. M., Larsen, R. M., Duvall, Jr., T. L., De Rosa, M. L., Hurlburt, N. E., Schou, J., Roth, M., Christensen-Dalsgaard, J., Lele, S. K., 2006, *Computational Acoustics in Spherical Geometry: Steps toward Validating Helioseismology*, ApJ, **648**, 1268–1275
- Hanasoge, S. M., Birch, A., Gizon, L., Tromp, J., 2011, *The Adjoint Method Applied to Time-distance Helioseismology*, ApJ, **738**, 100
- Hansen, C. J., Cox, J. P., van Horn, H. M., 1977, *The effects of differential rotation on the splitting of nonradial modes of stellar oscillation*, ApJ, **217**, 151–159
- Hartlep, T., Zhao, J., Mansour, N. N., Kosovichev, A. G., 2008, *Validating Time-Distance Far-Side Imaging of Solar Active Regions through Numerical Simulations*, ApJ, **689**, 1373–1378
- Hu, F. Q., Hussaini, M. Y., Manthey, J. L., 1996, *Low-Dissipation and Low-Dispersion Runge Kutta Schemes for Computational Acoustics*, Journal of Computational Physics, **124**, 177–191
- Khomenko, E., Collados, M., 2006, *Numerical Modeling of Magnetohydrodynamic Wave Propagation and Refraction in Sunspots*, ApJ, **653**, 739–755

- Kjeldsen, H., Arentoft, T., Bedding, T., Christensen-Dalsgaard, J., Frandsen, S., Thompson, M. J., 1998, *Asteroseismology and Stellar Rotation*, in Structure and Dynamics of the Interior of the Sun and Sun-like Stars, (Ed.) S. Korzennik, vol. **418** of ESA Special Publication, pp. 385–390
- Ledoux, P., 1951, *The Nonradial Oscillations of Gaseous Stars and the Problem of Beta Canis Majoris.*, ApJ, **114**, 373–384
- Leighton, R. B., Noyes, R. W., Simon, G. W., 1962, *Velocity Fields in the Solar Atmosphere. I. Preliminary Report.*, ApJ, **135**, 474–499
- Lele, S. K., 1992, *Compact Finite Difference Schemes with Spectral-like Resolution*, Journal of Computational Physics, **103**, 16–42
- Libbrecht, K. G., 1988, *Solar p-mode phenomenology*, ApJ, **334**, 510–516
- Libbrecht, K. G., Woodard, M. F., 1990, *Solar-cycle effects on solar oscillation frequencies*, Nature, **345**, 779–782
- Lynden-Bell, D., Ostriker, J. P., 1967, *On the stability of differentially rotating bodies*, MNRAS, **136**, 293–310
- Marsden, S. C., Waite, I. A., Carter, B. D., Donati, J.-F., 2005, *Doppler imaging and surface differential rotation of young open cluster stars - I. HD 307938 (R58) in IC 2602*, MNRAS, **359**, 711–724
- Messiah, A., 1959, *Mécanique Quantique*, Volume II, Appendix C.IV, Dunod, Paris
- Metcalf, T. S., Chaplin, W. J., Appourchaux, T., García, R. A., Basu, S., Brandão, I., Creevey, O. L., Deheuvels, S., Doğan, G., Eggenberger, P., Karoff, C., Miglio, A., Stello, D., Yıldız, M., Çelik, Z., Antia, H. M., Benomar, O., Howe, R., Régulo, C., Salabert, D., Stahn, T., Bedding, T. R., Davies, G. R., Elsworth, Y., Gizon, L., Hekker, S., Mathur, S., Mosser, B., Bryson, S. T., Still, M. D., Christensen-Dalsgaard, J., Gilliland, R. L., Kawaler, S. D., Kjeldsen, H., Ibrahim, K. A., Klaus, T. C., Li, J., 2012, *Asteroseismology of the Solar Analogs 16 Cyg A and B from Kepler Observations*, ApJ, **748**, L10
- Monteiro, M. J. P. F. G., 2009, *Evolution and Seismic Tools for Stellar Astrophysics*, Springer, Dordrecht
- Moradi, H., Baldner, C., Birch, A. C., Braun, D. C., Cameron, R. H., Duvall, T. L., Gizon, L., Haber, D., Hanasoge, S. M., Hindman, B. W., Jackiewicz, J., Khomenko, E., Komm, R., Rajaguru, P., Rempel, M., Roth, M., Schlichenmaier, R., Schunker, H., Spruit, H. C., Strassmeier, K. G., Thompson, M. J., Zharkov, S., 2010, *Modeling the Subsurface Structure of Sunspots*, Sol. Phys., **267**, 1–62
- Moreno-Insertis, F., Spruit, H. C., 1989, *Stability of sunspots to convective motions. I - Adiabatic instability*, ApJ, **342**, 1158–1171
- Mosser, B., Appourchaux, T., 2009, *On detecting the large separation in the autocorrelation of stellar oscillation times series*, A&A, **508**, 877–887

- Papini, E., Gizon, L., Birch, A. C., 2014, *Propagating Linear Waves in Convectively Unstable Stellar Models: A Perturbative Approach*, Sol. Phys., **289**, 1919–1929
- Papini, E., Birch, A. C., Gizon, L., Hanasoge, S. M., 2015, *Simulating acoustic waves in spotted stars*, A&A, **577**, A145
- Parchevsky, K. V., Kosovichev, A. G., 2007, *Three-dimensional Numerical Simulations of the Acoustic Wave Field in the Upper Convection Zone of the Sun*, ApJ, **666**, 547–558
- Pierce, K., 2000, in *Allen's Astrophysical Quantities*, 4th ed., New York: Springer
- Press, W. H., Teukolsky, S. A., Vetterling, W. T., Flannery, B. P., 1992, *Numerical recipes in FORTRAN. The art of scientific computing*, 1992, 2nd ed., Cambridge University Press
- Rauer, H., Catala, C., Aerts, C., Appourchaux, T., Benz, W., Brandeker, A., Christensen-Dalsgaard, J., Deleuil, M., Gizon, L., Goupil, M.-J., Güdel, M., Janot-Pacheco, E., Mas-Hesse, M., Pagano, I., Piotto, G., Pollacco, D., Santos, C., Smith, A., Suárez, J.-C., Szabó, R., Udry, S., Adibekyan, V., Alibert, Y., Almenara, J.-M., Amaro-Seoane, P., Eiff, M. A.-v., Asplund, M., Antonello, E., Barnes, S., Baudin, F., Belkacem, K., Bergemann, M., Bihain, G., Birch, A. C., Bonfils, X., Boisse, I., Bonomo, A. S., Borsa, F., Brandão, I. M., Brocato, E., Brun, S., Burleigh, M., Burston, R., Cabrera, J., Cassisi, S., Chaplin, W., Charpinet, S., Chiappini, C., Church, R. P., Csizmadia, S., Cunha, M., Damasso, M., Davies, M. B., Deeg, H. J., Díaz, R. F., Dreizler, S., Dreyer, C., Eggenberger, P., Ehrenreich, D., Eig Müller, P., Erikson, A., Farmer, R., Feltzing, S., de Oliveira Fialho, F., Figueira, P., Forveille, T., Fridlund, M., García, R. A., Giommi, P., Giuffrida, G., Godolt, M., Gomes da Silva, J., Granzer, T., Grenfell, J. L., Grotzsch-Noels, A., Günther, E., Haswell, C. A., Hatzes, A. P., Hébrard, G., Hekker, S., Helled, R., Heng, K., Jenkins, J. M., Johansen, A., Khodachenko, M. L., Kislyakova, K. G., Kley, W., Kolb, U., Krivova, N., Kupka, F., Lammer, H., Lanza, A. F., Lebreton, Y., Magrin, D., Marcos-Arenal, P., Marrese, P. M., Marques, J. P., Martins, J., Mathis, S., Mathur, S., Messina, S., Miglio, A., Montalbán, J., Montalto, M., Monteiro, M. J. P. F. G., Moradi, H., Moravveji, E., Mordasini, C., Morel, T., Mortier, A., Nascimbeni, V., Nelson, R. P., Nielsen, M. B., Noack, L., Norton, A. J., Ofir, A., Oshagh, M., Ouazzani, R.-M., Pápics, P., Parro, V. C., Petit, P., Plez, B., Poretti, E., Quirrenbach, A., Ragazzoni, R., Raimondo, G., Rainer, M., Reese, D. R., Redmer, R., Reffert, S., Rojas-Ayala, B., Roxburgh, I. W., Salmon, S., Santerne, A., Schneider, J., Schou, J., Schuh, S., Schunker, H., Silva-Valio, A., Silvotti, R., Skillen, I., Snellen, I., Sohl, F., Sousa, S. G., Sozzetti, A., Stello, D., Strassmeier, K. G., Švanda, M., Szabó, G. M., Tkachenko, A., Valencia, D., Van Grootel, V., Vauclair, S. D., Ventura, P., Wagner, F. W., Walton, N. A., Weingrill, J., Werner, S. C., Wheatley, P. J., Zwintz, K., 2014, *The PLATO 2.0 mission*, Experimental Astronomy, **38**, 249–330
- Ricker, G. R., Winn, J. N., Vanderspek, R., Latham, D. W., Bakos, G. Á., Bean, J. L., Berta-Thompson, Z. K., Brown, T. M., Buchhave, L., Butler, N. R., Butler, R. P., Chaplin, W. J., Charbonneau, D., Christensen-Dalsgaard, J., Clampin, M., Deming, D., Doty, J., De Lee, N., Dressing, C., Dunham, E. W., Endl, M., Fressin, F., Ge, J., Henning, T., Holman, M. J., Howard, A. W., Ida, S., Jenkins, J., Jernigan, G., Johnson,

- J. A., Kaltenecker, L., Kawai, N., Kjeldsen, H., Laughlin, G., Levine, A. M., Lin, D., Lissauer, J. J., MacQueen, P., Marcy, G., McCullough, P. R., Morton, T. D., Narita, N., Paegert, M., Palle, E., Pepe, F., Pepper, J., Quirrenbach, A., Rinehart, S. A., Sasselov, D., Sato, B., Seager, S., Sozzetti, A., Stassun, K. G., Sullivan, P., Szentgyorgyi, A., Torres, G., Udry, S., Villaseñor, J., 2014, *Transiting Exoplanet Survey Satellite (TESS)*, in Society of Photo-Optical Instrumentation Engineers (SPIE) Conference Series, vol. **9143** of Society of Photo-Optical Instrumentation Engineers (SPIE) Conference Series, pp. 20–34
- Santos, A. R. G., Cunha, M. S., Lima, J. J. G., 2012, *Asteroseismology and magnetic cycles*, *Astronomische Nachrichten*, **333**, 1032–1035
- Scherrer, P. H., Schou, J., Bush, R. I., Kosovichev, A. G., Bogart, R. S., Hoeksema, J. T., Liu, Y., Duvall, T. L., Zhao, J., Title, A. M., Schrijver, C. J., Tarbell, T. D., Tomczyk, S., 2012, *The Helioseismic and Magnetic Imager (HMI) Investigation for the Solar Dynamics Observatory (SDO)*, *Sol. Phys.*, **275**, 207–227
- Schou, J., Antia, H. M., Basu, S., Bogart, R. S., Bush, R. I., Chitre, S. M., Christensen-Dalsgaard, J., Di Mauro, M. P., Dziembowski, W. A., Eff-Darwich, A., Gough, D. O., Haber, D. A., Hoeksema, J. T., Howe, R., Korzennik, S. G., Kosovichev, A. G., Larsen, R. M., Pijpers, F. P., Scherrer, P. H., Sekii, T., Tarbell, T. D., Title, A. M., Thompson, M. J., Toomre, J., 1998, *Helioseismic Studies of Differential Rotation in the Solar Envelope by the Solar Oscillations Investigation Using the Michelson Doppler Imager*, *ApJ*, **505**, 390–417
- Schunker, H., Cameron, R. H., Gizon, L., Moradi, H., 2011, *Constructing and Characterising Solar Structure Models for Computational Helioseismology*, *Sol. Phys.*, **271**, 1–26
- Schunker, H., Gizon, L., Cameron, R. H., Birch, A. C., 2013, *Helioseismology of sunspots: how sensitive are travel times to the Wilson depression and to the subsurface magnetic field?*, *A&A*, **558**, A130
- Schwarzschild, K., 1906, *On the equilibrium of the Sun's atmosphere*, *Göttinger Nach.*, **195**, 41–53
- Shelyag, S., Erdélyi, R., Thompson, M. J., 2006, *Forward Modeling of Acoustic Wave Propagation in the Quiet Solar Subphotosphere*, *ApJ*, **651**, 576–583
- Strassmeier, K. G., 2009, *Starspots*, *A&A Rev.*, **17**, 251–308
- Tayler, R. J., 1973, *The adiabatic stability of stars containing magnetic fields-I. Toroidal fields*, *MNRAS*, **161**, 365
- Thompson, M. J., Toomre, J., Anderson, E. R., Antia, H. M., Berthomieu, G., Burtonclay, D., Chitre, S. M., Christensen-Dalsgaard, J., Corbard, T., De Rosa, M., Genovese, C. R., Gough, D. O., Haber, D. A., Harvey, J. W., Hill, F., Howe, R., Korzennik, S. G., Kosovichev, A. G., Leibacher, J. W., Pijpers, F. P., Provost, J., Rhodes, Jr., E. J., Schou, J., Sekii, T., Stark, P. B., Wilson, P. R., 1996, *Differential Rotation and Dynamics of the Solar Interior*, *Science*, **272**, 1300–1305

Bibliography

- Toutain, T., Gouttebroze, P., 1993, *Visibility of solar p-modes*, A&A, **268**, 309–318
- Trampedach, R., 2010, *Convection in stellar models*, Ap&SS, **328**, 213–219
- Tromp, J., Tape, C., Liu, Q., 2005, *Seismic tomography, adjoint methods, time reversal and banana-doughnut kernels*, Geophysical Journal International, **160**, 195–216
- Unno, W., Osaki, Y., Ando, H., Saio, H., Shibahashi, H., 1989, *Nonradial oscillations of stars*, University of Tokyo Press
- Wilson, O. C., 1968, *Flux Measurements at the Centers of Stellar h- and K-Lines*, ApJ, **153**, 221–234

Publications

Refereed publications

- E. Papini, L. Gizon, and A. C. Birch, “*Propagating Linear Waves in Convectively Unstable Stellar Models: A Perturbative Approach*”, *Sol. Phys.*, **289**, 1919-1929, 2014.
- E. Papini, A. C. Birch, L. Gizon, and S. K. Hanasoge, “*Simulating acoustic waves in spotted stars*”, *A&A*, **577**, A145, 2015.

Conference Contributions

- Stellar and Planetary Dynamos Conference, Göttingen, Germany, May 26-29, 2015
Poster: “*Simulating acoustic waves in spotted stars.*”
- HELAS VI/ SOHO-28/ SPACEINN Conference "Helioseismology and Applications", Göttingen, Germany, September 1-5, 2014
Poster: “*Simulating acoustic waves in spotted stars.*”
- École de physique des Houches Workshop “The future of plasma astrophysics: combining experiments, observations, simulations and theory”, Les Houches, France, February 25- March 8, 2013
Poster: “*Convectively-stable stellar models for computational seismology*”
- Rocks’n’Stars Conference, Göttingen, Germany, October 8-11, 2012
Talk: “*Propagating linear waves in a convectively unstable solar model: a perturbative approach.*”

Acknowledgements

First of all, I would like to thank my supervisors, Laurent Gizon and Aaron Birch, who guided me through my entire PhD. My research, my work and my scientific education largely benefited from their deep knowledge and experience in this field of research. I am very thankful to Shravan Hanasoge, now at TIFR Mumbai, who gave me full access to the GLASS code.

I thank Ansgar Reiners for accepting to be part of my TAC committee, and to be one of the referees of my thesis. I am thankful to Prof. Jörg Büchner, Prof. Thorsten Hohage, Dr. Olga Shishkina, and Prof. Andreas Tilgner for agreeing to be in the examination committee.

I acknowledge research funding by the *Deutsche Forschungsgemeinschaft* (DFG) under the grant SFB 963 “Astrophysical Turbulence and Flow Instabilities” (Project A18). I performed the numerical simulations using the cluster at the German Data Center for SDO.

As part of The *International Max Planck Research School for Solar System Science at the University of Göttingen*, I owe many many thanks to the coordinator, Sonja Schuh, who helped me with all the bureaucratic procedures and typos and showed a considerable amount of patience with any issue I had.

I am particularly grateful to Robert Cameron for all the useful discussions and the help in fixing GLASS. I thank Raymond Burston for his help in using the cluster. Hannah Schunker and Jesper Schou were always available to help with any scientific issue or just to have a good chat. I am thankful to them for their encouragement. I thank my friends and colleagues from IMPRS and MPS: Jan, Björn, Martin, Atefeh, Francisco, (spanish) David, Rakesh, Ankit, Fabien, Vali, Wieland, Don, Nafiseh, Ricardo and many others. With some of them I also enjoyed playing volleyball and basketball. I thank Björn who spent half of his morning to translate my summary to German, and did a really good job. With the MPS choir I spent only wonderful times: with Klaus, David, Maria, Jacob, Marc, Kaori, Tanja, Irene, and Anusha, and other “recurring characters”. We shared the joy of singing together and discovering new songs.

Very special thanks go to my little Italian community inside MPS. Luca and Domenico filled almost every morning and after-lunch with good jokes and chats in our exclusive coffee club. Luca and Regina, with their little kids, made many weekends enjoyable. With Domenico, Marco, and Giulia we had great times trying to survive in Lindau, Marco in particular for the continuous new breaking ideas on inventing new hobbies. Domenico was always there for help and support, and to share a whisky together. In the last year few people added to the list, my Italian friends Piero, Annalisa, Matteo, Mattia, and many others.

I am grateful to my family, my parents for their love and encouragement, my twin

Acknowledgements

Davide, and all my brothers and sister Francesco, Giacomo and Ester; my grand parents, whom I miss every day.

Last but not least I want to thank Nathalie, for her love, support, and a lot of patience in the last months.

Curriculum vitae

Personal

Name: Emanuele Papini
Date of birth: December 20, 1984
Place of birth: Firenze, Italy
Nationality: Italian

Education

- 01/2012 – 07/2015: Ph. D. studies
University: Georg-August-Universität Göttingen, Germany
Institute: Max-Planck-Institut für Sonnensystemforschung, Göttingen, Germany
Title of the dissertation:
“Simulating the signature of starspots in stellar oscillations.”
- 01/2008 – 09/2011: M. Sc. in Physics and Astrophysics
Università degli studi di Firenze, Firenze, Italy
Title of the master thesis:
“Fast Magnetic Reconnection in the resistive MHD regime: Numerical Simulations.”
Thesis Supervisor: Dr. Simone Landi
- 09/2003 – 01/2008: B. Sc. in Physics and Astrophysics
Università degli studi di Firenze, Firenze, Italy
Title of the bachelor thesis:
“Non-Maxwellian Distribution Functions in the Solar Corona.”
Thesis Supervisor: Prof. Dr. Claudio Chiuderi

Publications

- E. Papini, L. Gizon, and A. C. Birch, “*Propagating Linear Waves in Convectively Unstable Stellar Models: A Perturbative Approach*”, *Sol. Phys.*, **289**, 1919-1929, 2014.
- E. Papini, A. C. Birch, L. Gizon, and S. K. Hanasoge, “*Simulating acoustic waves in spotted stars*”, *A&A*, **577**, A145, 2015.
- S. Landi, L. Del Zanna, E. Papini, F. Pucci, and M. Velli, *Resistive Magnetohydrodynamics Simulations of the Ideal Tearing Mode* *ApJ*, **806**, 131–138, 2015.

Conference Contributions

- Stellar and Planetary Dynamos Conference, Göttingen, Germany, May 26-29, 2015
Poster: “*Simulating acoustic waves in spotted stars.*”
- HELAS VI/ SOHO-28/ SPACEINN Conference "Helioseismology and Applications", Göttingen, Germany, September 1-5, 2014
Poster: “*Simulating acoustic waves in spotted stars.*”
- École de physique des Houches Workshop “The future of plasma astrophysics: combining experiments, observations, simulations and theory”, Les Houches, France, February 25- March 8, 2013
Poster: “*Convectively-stable stellar models for computational seismology*”
- Rocks’n’Stars Conference, Göttingen, Germany, October 8-11, 2012
Talk: “*Propagating linear waves in a convectively unstable solar model: a perturbative approach.*”